Analytical Representation and Finite Element Analysis of Magnetically-Geared Permanent Magnet Machines

by

Sajjad Mohammadi Yangijeh

B.Sc., Kermanshah University of Technology (2011)
M.Sc., Amirkabir University of Technology (2014)

Submitted to the Department of Electrical Engineering and Computer Science
in partial fulfillment of the requirements for the degree of

Master of Science in Electrical Engineering and Computer Science

at the

MASSACHUSETTS INSTITUTE OF TECHNOLOGY

June 2019

Author .....
Department of Electrical Engineering and Computer Science
May 23, 2019

Certified by .....
James L. Kirtley Jr.
Professor of Electrical Engineering and Computer Science
Thesis Supervisor

Accepted by .....
Leslie A. Kolodziejski
Professor of Electrical Engineering and Computer Science
Chair, Department Committee on Graduate Students

Analytical Representation and Finite Element Analysis of Magnetically-Geared Permanent Magnet Machines

by

Sajjad Mohammadi Yangijeh

Submitted to the Department of Electrical Engineering and Computer Science
on May 23, 2019, in partial fulfillment of the
requirements for the degree of
Master of Science in Electrical Engineering and Computer Science

Abstract

Recently, magnetic gears have drawn significant interest as a promising alternative to their mechanical counterparts by introducing features such as generating high torque at low speed, reduced acoustic noise and vibrations, low maintenance, inherent overload protection, improved reliability, physical isolation between shafts, and contactless power transfer. Conventional electrical machines can be combined with magnetic gears to form a compact device called a magnetically-geared machine. They have found their way into mechatronics, wind turbines, wave energy generation and electric vehicles. Such devices can be studied by numerical techniques or analytical frameworks. The former such as finite element methods (FEM), although powerful, is expensive and time-consuming, while the latter approach like flux-tube based models provide a flexible yet reasonable solution for preliminary designs and optimizations. In this thesis, there has been a comprehensive study on flux-tube based modeling and finite element analysis of the machine. The stator is represented using flux-tube based carterâĂŹs coefficient and a surface current density. The permanent magnets are modeled by different approaches including magnetization density, Coulombian fictitious charges and Amperian currents. The air-gap permeances are also modeled by flux-tubes. Closed-form expressions for the magnetic fields has been extracted. The developed torques has been calculated by different techniques including Maxwell stress tensor, Lorentz force and Kelvin force density. These options provide designers with a universal and flexible framework, enabling them to pick the best technique according to the configuration and application. The field modulation concepts and the gearing effects have been investigated using the developed analytical framework as well as 2D and 3D FEM, whose results agree. Both radial-flux and axial-flux configurations, the two main structures of rotating electrical machines, have been studied as well.

Thesis Supervisor: James L. Kirtley Jr.
Title: Professor of Electrical Engineering and Computer Science

بسم الله الرحمن الرحيم

And say, "My Lord, increase me in knowledge."

Quran [20:114]

Acknowledgment

I am delighted to acknowledge everyone who contributed to my thesis or provided me with any kind of support and motivation. First, I would like to express my sincere appreciation to professor James Kirtley for his encouragement, guidance and support throughout this thesis. His knowledge and experience in the field of electric machines and electromagnetic devices provided me an opportunity to gain expertise.

I also would like to express my gratitude to the people at Kermanshah University of Technology, Amirkabir University of Technology and University of Tehran, from which I developed a strong foundation scientifically and learned a lot ethically.

Also, I would like to thank all my colleagues at the Grainger Energy Machines Facility (GEM) at MIT, formerly known as the laboratory of electromagnetic and electronic systems (LEES), and the Iranian community at MIT and Boston area, who provided me a positive and supportive environment.

I also want to express my appreciation for the masterpiece of the great Persian poet Mowlana Balkhi Rumi whose poetry, especially his renowned book *Masnavi*, has inspired my soul to seek eternal values beyond day-to-day life.

Words can never do justice to express my gratitude to my family, especially my father and my mother for the sacrifice they have always made, just like a candle which burns itself to light the way of others. After the favor of God, the Compassionate, my family have always been the unconditional source of love, endless care and continuous support.

Contents

List of Figures

List of Tables

Chapter 1

Introduction

1.1 Magnetically-geared machines

Electrical machines and electromagnetic devices have the important role of energy conversion between electrical and mechanical forms. Recently, magnetic gears have drawn significant attention as a promising dual to mechanical gears by featuring advantages such as generating high torque at low speed, reduced acoustic noise and vibrations, low maintenance, inherent overload protection, improved reliability, physical isolation between shafts, and contactless power transfer [1]-[4]. Conventional electrical machines are usually integrated with mechanical gears to match the torque-speed characteristics required by the application, in which magnetic gears are a promising substitution that can simply be attached to any mechanical or electrical machine [2]-[3], or can be combined with electric machines into compact device [4]. They have found their way into robotics and mechatronics, wind turbines [5], wave energy generation [6]-[8] and electric vehicles [9].

Magnetic gears can be connected to conventional electric machines with isolated magnetic circuits [2]. Also, they can be combined into a single compact machine called magnetically-geared machines [4]. Recently, valuable studies has been done on both radial-flux [10]-[12] and axial-flux [13]-[15] magnetic gears using finite element analysis.

Almost more works has been done in the study of magnetic gears and magnetically-geared machines by finite element analysis than using analytical methods, so there is still a big demand for the modeling of magnetic gears and specially magnetically-geared machines which can be used in the investigation of the nature of the machine as well as preliminary design stages and optimizations. A magnetic equivalent circuit is presented for magnetic gears very recently [16]-[17]. Another valuable contribution to the field is [18], in which a magnetic gear has been modeled by solving Laplace's and Poison's equation; although, the accuracy of the framework is not that good and such models do not have a

flexibility in complex structures, it opens a new door to the analytical study of magnetic gears. Investigation of the magnetic fields within the machine in order to understand the field modulation and gearing effect has been done in [19] and [20] as well.

1.2 Thesis contributions

Contributions of this thesis to the field of electrical machines and specifically magnetic gears can be summarized in the following points:

- Utilization of two-dimensional and three-dimensional finite element method as a power numerical tool in the design and analysis of electrical machines, especially magnetically geared permanent magnet machines.

- Investigation and implementations of the flux-tube method, also called magnetic equivalent circuit (MEC), as a flexible yet accurate analytical framework for the study of the physics, analysis, design and optimization of electromagnetic devices, especially magnetically-geared machines.

- Development of a novel analytical model for magnetically-geared machines for the two cases of rotating modulator ring and rotating PM ring. The accuracy of the model has been varied by FEM, showing a very close agreement between the analytical and numerical results.

- Modeling the stator and the PMs by employing different techniques such as magnetization density, Amperian currents and coulombian fictitious charges, providing a general framework so that a suitable technique can be used based on the geometry of the machine for further study of such devices.

- Extracting closed-form expressions for the magnetic fields and the developed torque using different approaches including Maxwell stress tensor, Lorentz force and Kelvin force. These options give the designers a flexibility to choose the best technique according to the configuration and application of the device.

- Study the nature and behavior of magnetically geared machines and extracting its main characteristics such as torque, field and back-EMF with different

scenarios and conditions. This study is done both analytically using the model and numerically using 2D and 3D FEM.

- Study the behavior of both radial-flux and axial-flux configurations of magnetically-geared synchronous machines as the two main structures of electrical machines using 2D and 3D FEM.

1.3 Thesis structure

Chapter 2 is devoted to finite-element method (FEM) as a powerful numerical technique that provides an accurate analysis, although it might be expensive and time-consuming. A detailed study and development of a novel structure for switched reluctance machines (SRMs) using 2D FEM has been studied. Analytical approaches provide fast and relatively accurate solutions that could be utilized in the design optimizations, as well as providing physical concepts for the designers. Both numerical or analytical techniques may be used in the analysis of electrical machines. Numerical approaches like finite element method (FEM), although accurate, are usually expensive and too time-consuming to be used in the design optimizations, while analytical models by providing fast, yet accurate solutions are a very good trade-off between accuracy and simplicity—useful in preliminary design stages. Chapter 3 is on the flux-tube based modeling of electromagnetic devices. Also, modeling of a switched reluctance motor as a very good example has been studied. It is shown that the developed model has superiorities in terms of accuracy and flexibility over the existing ones. All taken together, it is tried to show that analytical models are appropriate for preliminary stages of the design optimization, and numerical techniques are suitable for final verification of the results.

In chapter 4, a comprehensive analytical model for magnetically-geared permanent magnet machines has been developed using different approaches. An attempt has been made to employ different techniques to provide a universal framework so that a set of options will be provided for the designers and engineers, enabling them to pick the suitable method based on the configuration and geometry of the device. A flux-tube based model for the Carter's coefficient has been obtained to account for the slot effect. Detailed study of the air-gap field has been done, based on which analytical expressions of the air-gap

permeances has been extracted; a simplified model and an accurate one has been proposed. The stator is modeled by magnetomotive force and a surface current density. The permanent magnets are modeled with three techniques: magnetization density, Coulombian model and Amperian current representation. The air-gap flux has been obtained and finally a closed-form expression for the developed torque has been extracted by employing different techniques: Maxwell stress tensor, Lorentz force and Kelvin force density. The modulation concept and the gearing effect has been studied as well. All the aforementioned procedures have been performed for two cases: modulator ring as the rotor or the PM ring as the rotor.

In chapter 5, a radial-flux magnetically-geared machine has been studied using 2D FEM. It has been shown that the results obtained from the developed analytical model correlate well with those obtained from FEM, and there is a match between the discussed concepts. Main characteristics of the machine including torque-angle curve, torque profile, back-EMF, magnetic flux density distribution are also extracted. Harmonics analysis is also performed to investigate the modulation effect. Chapter 6 is devoted to the study of an axial-flux magnetically-geared machine as one of the two main structures of electrical machines. It is analyzed using 3D FEM. Finally, we will be talking about the conclusions and the future works in chapter 7.

Chapter 2

Finite Element Analysis

2.1 Introduction

Finite-element method (FEM) is a powerful numerical technique that provides an accurate analysis, although it might be expensive and time-consuming [21]. Analytical approaches provide fast and relatively accurate solutions that could be utilized in the design optimizations, as well as providing physical concepts for the designers. All taken together, analytical models are appropriate for preliminary stages of the design procedure, and numerical techniques for final verification of the results. It is also worth noting that there has been a remarkable interest in FEM-based study of variety of electric machines, from eddy-current couplers [22]-[25] to induction motors [26].

2.2 FEM-based analysis and design of a novel switched reluctance motor

In this section, two-dimensional finite element method (2D FEM) is employed in design and analysis of a novel topology for 8/10 two-phase switched reluctance motors (TPSRM). The related paper has been recently presented in 2018 IEEE Industry Applications Society Annual Meeting (IAS) by the author of this master thesis [27]. It has also been published in [28]. In the proposed TPSRMs, a wound stator pole of the same phase as the flux return path is embedded. Thanks to FEM, the motor is studied and fully analyzed. Through a comprehensive comparison, superiorities of the proposed 8/10 TPSRM over two analogous 6/10 [29] and 9/12 [30] TPSRMs. FEM has been employed to study, analyze and design of the proposed switched reluctance machine in this chapter.

2.2.1 Topology of the TPSRM

Fig. 2.1 shows the geometry of the 8/10 TPSRM, in which the two adjacent stator poles and the diametrically opposite poles have the same phase. The topology and specifications of the proposed, 6/10, and 9/12 TPSRMs to be compared, are presented in Fig. 2.2 and

Table 2.1. The stator outer radius and stack length of the three motors are equal. The common feature of them is that they provide a return path for the flux so that the back iron flux path is shortened compared to conventional SRMs in which the flux flows through the whole stator/rotor back iron.

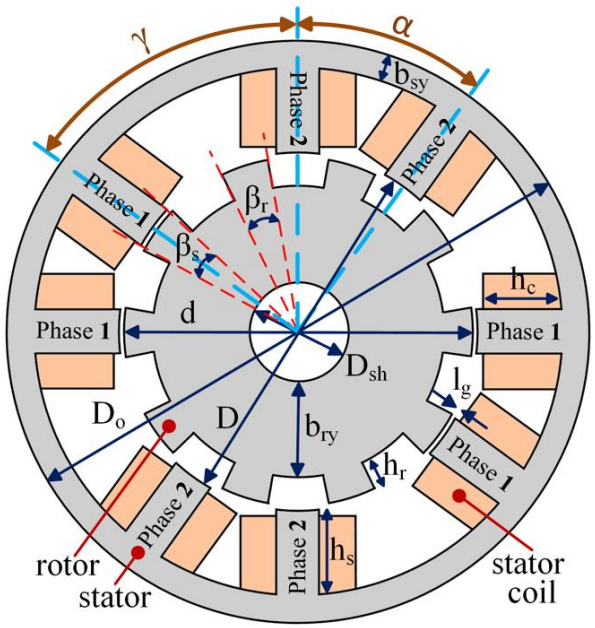

Figure 2.1: Geometry of the proposed switched reluctance motor

Table 2.1: Machine specifications

parameter	8/10 SRM	9/12 SRM	6/10 SRM
stator outer diameter, D_o (mm)	82	82	82
stator back iron thickness, b_{sy} (mm)	3.85	6	6
stator pole height, h_s (mm)	12	12.6	10.29
stator inner diameter, D (mm)	50.3	44.8	49.42
air-gap length, l_g (mm)	0.17	0.17	0.17
rotor outer diameter, d (mm)	49.96	44.46	49.08
rotor pole height, h_r (mm)	4	8.54	9.09
rotor back iron thickness, b_{ry} (mm)	13.98	7.09	8.85
rotor shaft diameter, D_{sh} (mm)	14	13.2	13.2
stator pole arc, β_s (deg)	14	13.8	16
rotor pole arc, β_r (deg)	16	13.2	18.9
stack length, L (mm)	25.4	25.4	25.4
available winding space, A_w (mm^2)	64	64	67
number of windings, N_w	8	6	4

number of turns per pole, T_{ph}	110	110	110

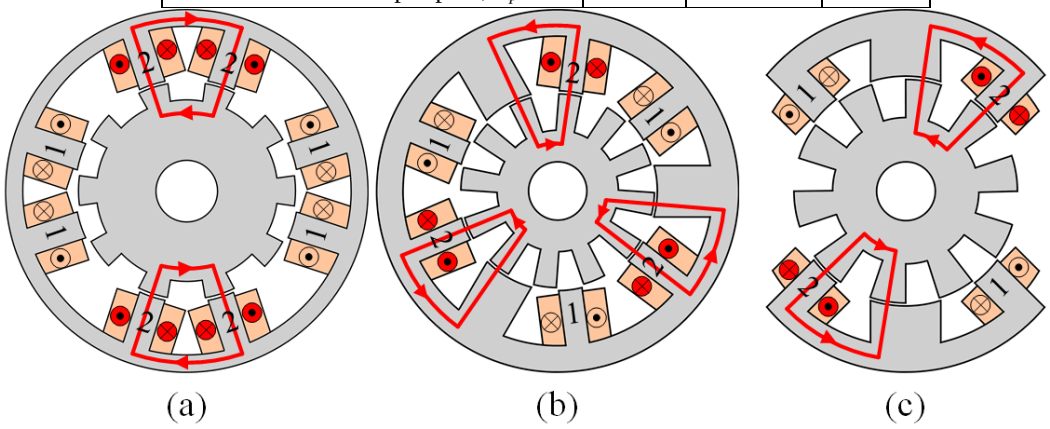

Figure 2.2: Topology and main flux paths of (a) the proposed 8/10 TPSRM, (b) the 9/12 TPSRM, and (c) the 6/10 TPSRM

2.2.2 Topology

In the proposed 8/10 TPSRM, the return flux path is designed such that another wound stator pole is embedded in the motor, resulting in a significant flux increase and subsequently a higher torque density. Also, both the core volume in which the flux reverses is reduced. Moreover, the traverse flux paths in the rotor/stator back irons are shortened (lower MMF required). Fig. 2.3 illustrate the flux paths within the motor for the aligned condition under the excitation of phase 1. The bold line indicates the main flux path, while the thin line denotes the path having a very small amount of flux flows.

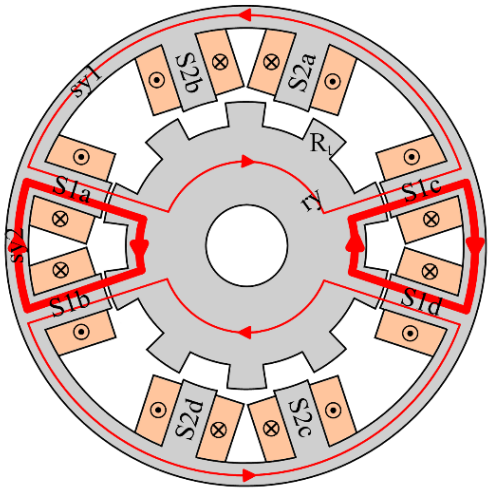

Figure 2.3: Flux paths within the proposed 8/10 TPSRM when phase 1 is excited under the aligned condition.

The pole combinations (S/R) for TPSRMs with four stator poles are 4/2, 4/6, 4/10, 4/14, 4/18; that is, R=S*{0.5, 1.5, 2.5, 3.5, …}. As shown in Fig. 2.4, the return path is obtained by merging the stator with its duplicate that is rotated by a multiple of rotor pole pitch θ_{rp}. The main flux path is also shown. In Fig. 2.4(a), a 4/6 TPSRM stator is merged with a duplicate rotated by θ_{rp} to achieve an 8/6 TPSRM. However, the problem is that the two adjacent stator poles of different phase are too close to each other to provide enough winding space.

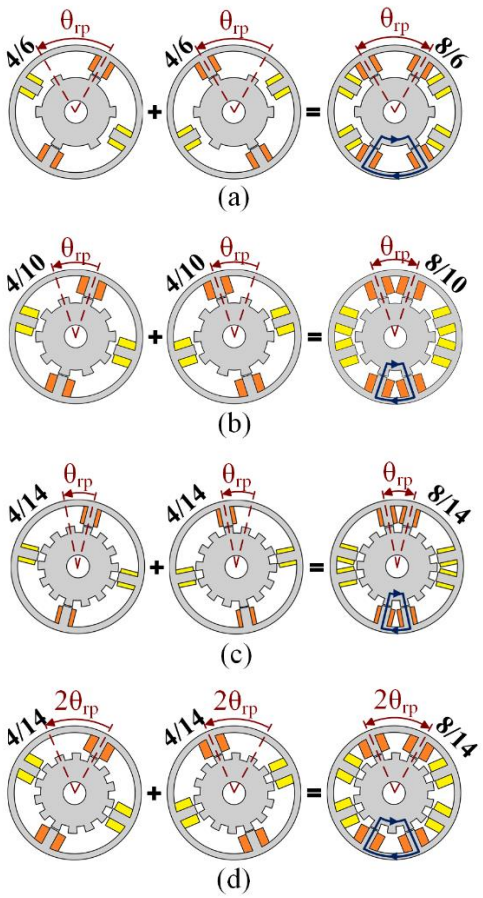

Figure 2.4: (a) Merging a 4/6 SRM stator with a duplicate after θr rotation to achieve 8/6 SRM, (b) merging a 4/10 SRM stator with a duplicate after θr rotation to achieve 8/10 SRM, (c) merging a 4/14 SRM stator with a duplicate after θr rotation to achieve 8/14 SRM

In Fig. 2.4(b), a 4/10 TPSRM stator is merged by a duplicate rotated by θ_{rp} to achieve a novel 8/10 TPSRM, where we have a satisfactory space for stator windings (design candidate).

In Figs. 2.4(c) and (d), a 4/14 TPSRM stator is merged by a duplicate, while the stator is rotated by $2_{\theta rp}$. The main drawback of the former is the same as that of the first topology, i.e., very small winding areas. Generally, the closer the value of α to the value of γ, the larger the winding space. Although this problem is somewhat solved in the latter, the larger number of rotor poles needs an increased switching, increased flux path lengths, and increased number of flux reversals (increased hysteresis loss) in the rotor poles.

2.2.3 Design formulas

The angle between two nearby stator poles, which is equal to rotor pole pitch angle, is as follows:

$$\alpha = 360^{\circ} / N_r \tag{2.1}$$

The angle between two faraway stator poles γ can be obtained by solving the following proportion:

$$\frac{2}{N_s} = \frac{\alpha + \gamma}{360^{\circ}} \Rightarrow \gamma = \frac{720^{\circ}}{N_s} - \alpha \tag{2.2}$$

Rotor poles pitch angle is as follows:

$$\theta_{rp} = 360^{\circ} / N_r \tag{2.3}$$

The following criterion should be satisfied to efficiently design the stator yoke length:

$$0.5\omega_{sp} < b_{sy} < \omega_{sp} \tag{2.4}$$

The stator pole width can simply be obtained as in below:

$$\frac{\omega_{sp}}{2} = \frac{D}{2}\sin\left(\frac{\beta_s}{2}\right) \Rightarrow \omega_{sp} = D\sin\left(\frac{\beta_s}{2}\right) \tag{2.5}$$

In order to effectively utilize the inter-pole area for stator windings, the following criterion should be satisfied [30]:

$$h_c < h_s < 1.4h_c \tag{2.6}$$

where, h_c is winding height. The stator outer diameter is:

$$D_o = D + 2b_{sy} + 2h_s \tag{2.7}$$

Rotor pole height can also be obtained as in below:

$$h_r = \left(D - 2l_g - D_{sh} - 2b_{ry}\right)/2 \tag{2.8}$$

2.2.4 Sensitivity analysis of stator and rotor parameters

Fig. 2.5 shows the design algorithm. To achieve a satisfactory design, machine dimensions are optimally designed to maximize the average torque under a constant stack length and outer diameter.

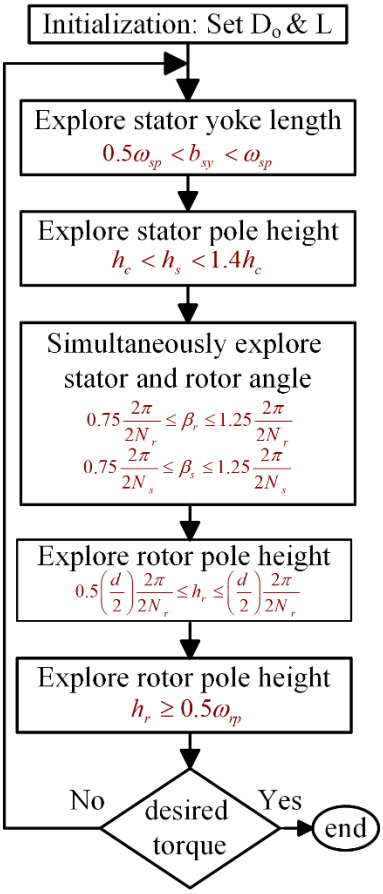

Figure 2.5: Design algorithm

Fig. 2.6(a) shows the average torque sensitivity versus simultaneous variations of rotor pole angle β_r and stator pole angle β_s, in which the optimal point is where stator and rotor teeth operate near the knee of the core saturation curve. Fig. 2.6(b) shows that a very small stator pole height h_s results in a too small winding area while a very large value decreases the air-gap radius (torque leg). The average torque sensitivity versus rotor pole height h_r is given in Fig. 2.6(c), showing that a very small value decreases the reluctance difference reducing the torque while a very large value increases the flux path length and thus, higher MMF requirements. Fig. 2.6(d) shows the average torque versus the stator yoke length b_{sy}. Fig. 2.6(e) shows the torque versus yoke thickness.

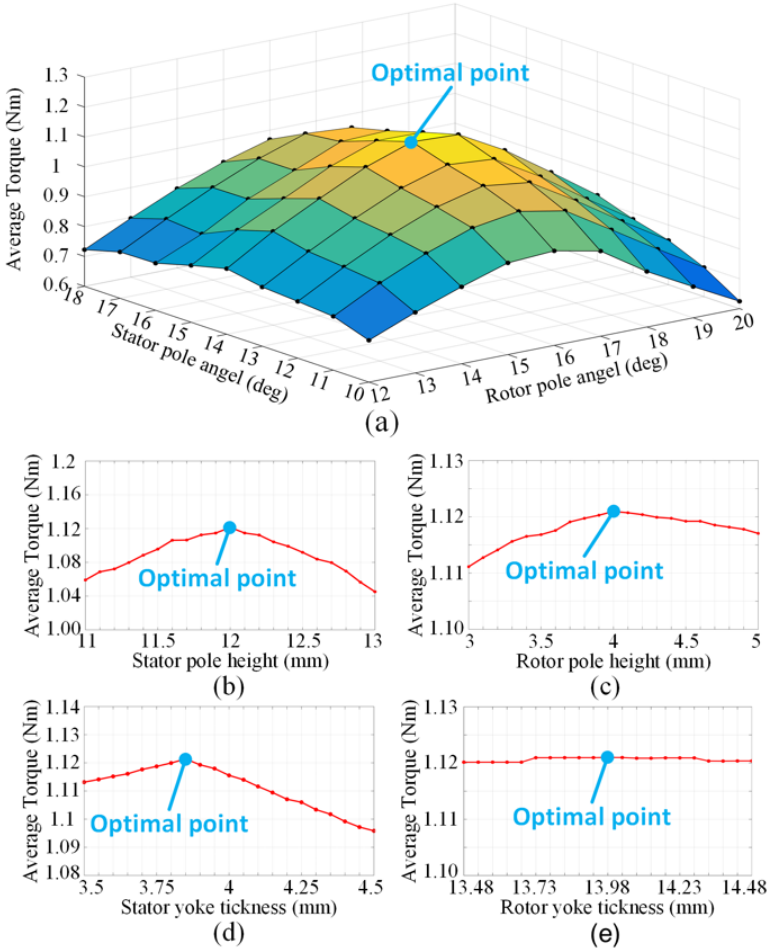

Figure 2.6: Sensitivity of average torque versus (a) variations of rotor pole angle and stator pole angle, (b) stator pole height, (c) rotor pole height, (d) stator yoke thickness, and (e) rotor yoke thickness.

2.2.5 Flux analysis

Fig. 2.7 illustrates flux lines and flux density distribution within the machine for unaligned and aligned conditions when phase 1 is excited.

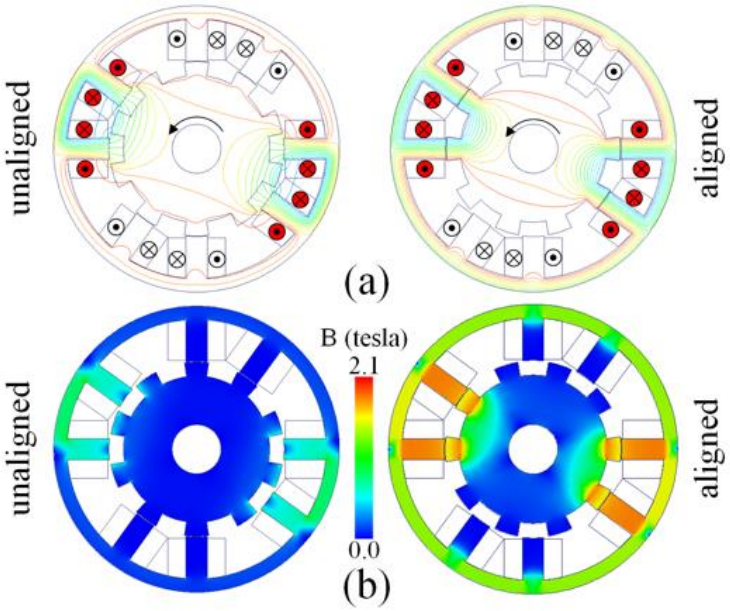

Figure 2.7: (a) Flux lines, (b) flux density distribution of machine under unaligned and aligned conditions when phase a is excited.

Flux variation in different core sections under a 360-degree rotor rotation is shown in Fig. 2.8. The core sections from which the flux lines flow and the corresponding positive directions are also depicted. It is seen from Fig. 2.8(a) that always flux flows into the stator yoke between the teeth of two different phases only in one direction—no flux reversal. Fig. 2.7(b) shows the flux traversing the stator yoke between the teeth of the same phases (assume phase 1), illustrating ten times flux reversals in a complete rotor rotation. The negative values come from energizing the other phase (phase 2), starting from zero (at the unaligned position of phase 2) to the maximum (at the aligned position of phase 2). However, it is seen in Fig. 2.7(c) that the corresponding flux density in this section is very small—minor loss. The flux flowing into a rotor tooth, as shown in Fig. 2.8(c), denotes four times flux reversals in one rotor revolution which occurs when the rotor tooth is unaligned with the pole that is to be excited. The number of flux reversals is not large in this section. Fig. 2.8(d) shows the flux flowing into the rotor yoke in a full rotor rotation, showing a very small magnitude for variations—no significant flux reversal. Figs. 2.8(e)

and (f) illustrate the flux flowing into the stator tooth of phase 1 and 2 without any flux reversals.

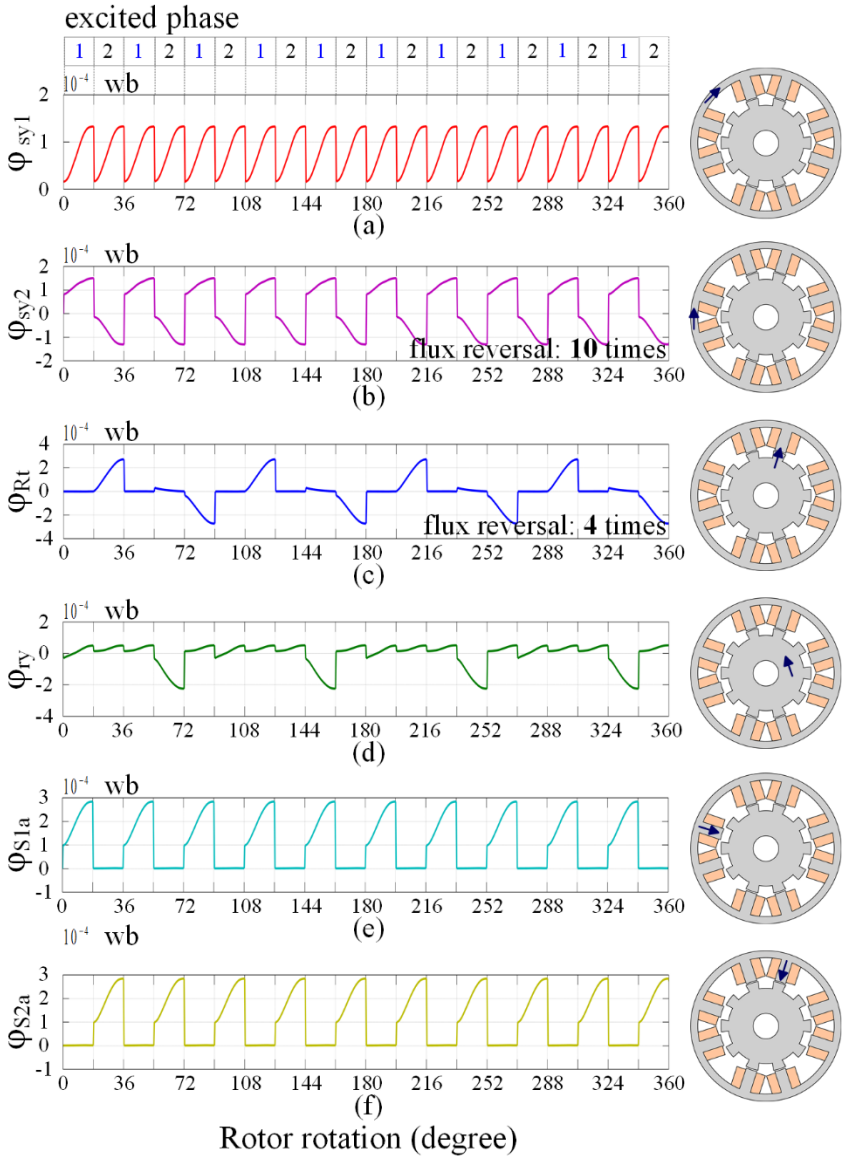

Figure 2.8: Flux analysis in core sections under a 360-degree rotor rotation: (a) stator yoke between teeth of two different phases, (b) stator yoke between teeth of two similar phases, (c) rotor tooth, (d) rotor yoke, (e) tooth of stator phase 1a, and (f) tooth

In the two valuable works done in the design of a 6/10 TPSRM [29] and a 9/12 TPSRM [30], the main disadvantage of the common pole is the negative torque (NT) caused by the flux traversing the other phase when one phase is excited. Fig. 2.9 shows the corresponding

flux lines under aligned and unaligned conditions. It is seen that when phase 1 is excited, a small part of the generated flux flows through phase 2 producing a negative torque, which is larger in 9/12 TPSRM compared to 6/10 TPSRM because a larger amount of flux flows into the adjacent phase due to its shorter path. This issue is addresses in the proposed 8/10 TPSRM by employing another wound pole of the same phase as the flux return path—no negative torque caused by passing a minor flux through the other phase.

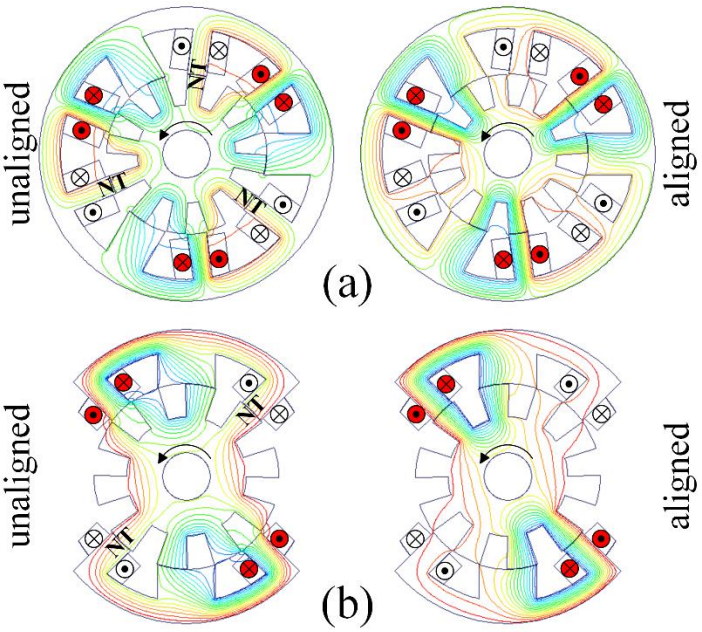

Figure 2.9: Flux lines of (a) existing 9/12 TPSRM and (b) existing 6/10 TPSRM under unaligned and aligned conditions (NT denotes the regions where negative torque is produced).

Fig. 2.10 illustrates a comparison of the regions, including flux reversals as well as those without any flux reversals or having very minor flux reversals. The major flux reversal in the proposed 8/10 TPSRM occurs in the rotor teeth due to the main flux path of a phase, while the flux reversal in the stator yoke between the teeth of the same phases occurs due to the minor flux path developed by the other phase excitation, and is less significant comparatively. In the existing 9/12 TPSRM, flux reversal happens in the essential core sections, including rotor/stator poles, rotor yoke, and the stator yoke section between the teeth of different phases. However, no flux reversal occurs in the common pole and the adjacent stator yokes. In the existing 6/10 TPSRM, major flux reversals occur in the rotor yoke and teeth, while minor flux reversals happen in the stator poles and yokes due to the excitation of the other phase. However, there is no reversal in the common pole.

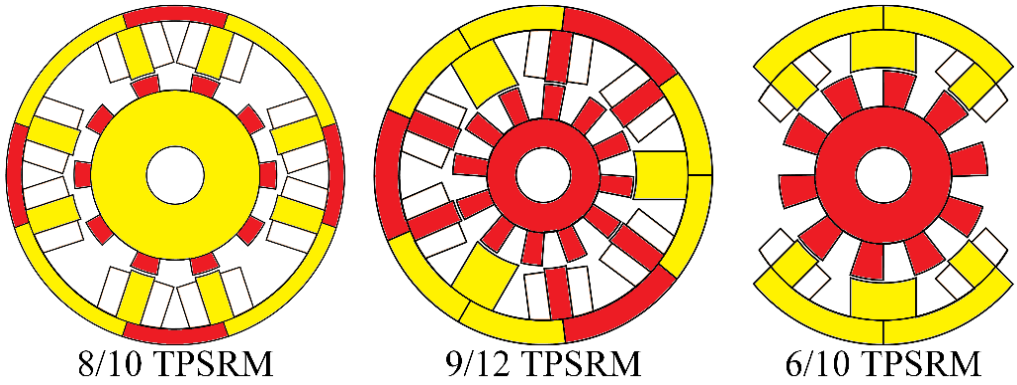

Figure 2.10: Regions with flux reversal in red

2.3 Results and comparisons

Herein, a study is carried out and the main characteristics of the proposed machine are analyzed. Saturation characteristics of the utilized iron is shown in Fig. 2.11. Fig. 2.12 shows the flux linkage characteristics of the machine for the aligned and unaligned conditions. The torque-angle characteristics under different stator currents is given in Fig. 2.13 which shows an acceptable agreement between experimental results and those obtained from FEM.

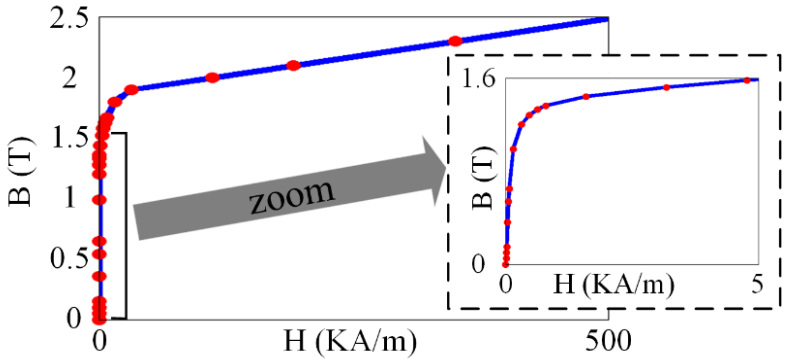

Figure 2.11: Saturation characteristics of the iron

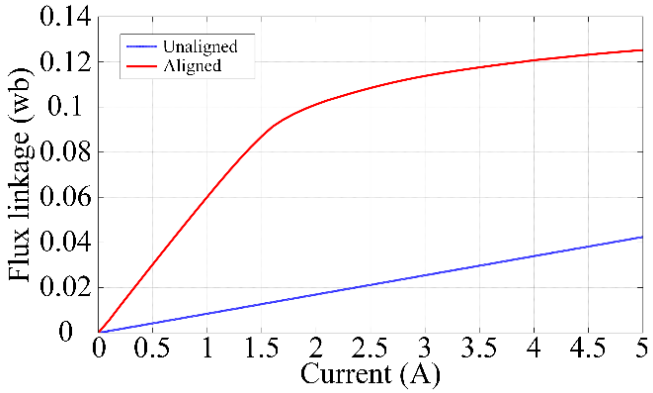

Figure 2.12: Flux linkage characteristic under aligned and unaligned positions

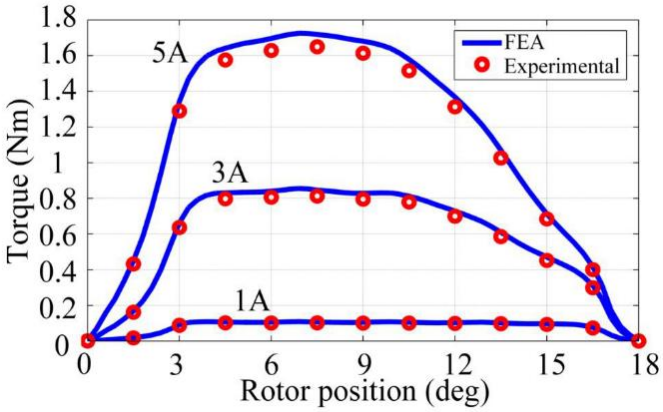

Figure 2.13: Torque-angle characteristic of the motor

In this section, a comparison between the three motors under the same volume is carried out. In Fig. 2.14, torque angle characteristics of the three motors for various stator currents are compared. Because of elimination of negative torques, higher torques are obtained for the proposed 8/10 TPSRM, while there is a negative torque in the 9/12 and 6/10 TPSRMs (yellow regions). Fig. 2.15 presents the average and peak torques of the three motors for different stator currents, showing an enhancement for the proposed structure.

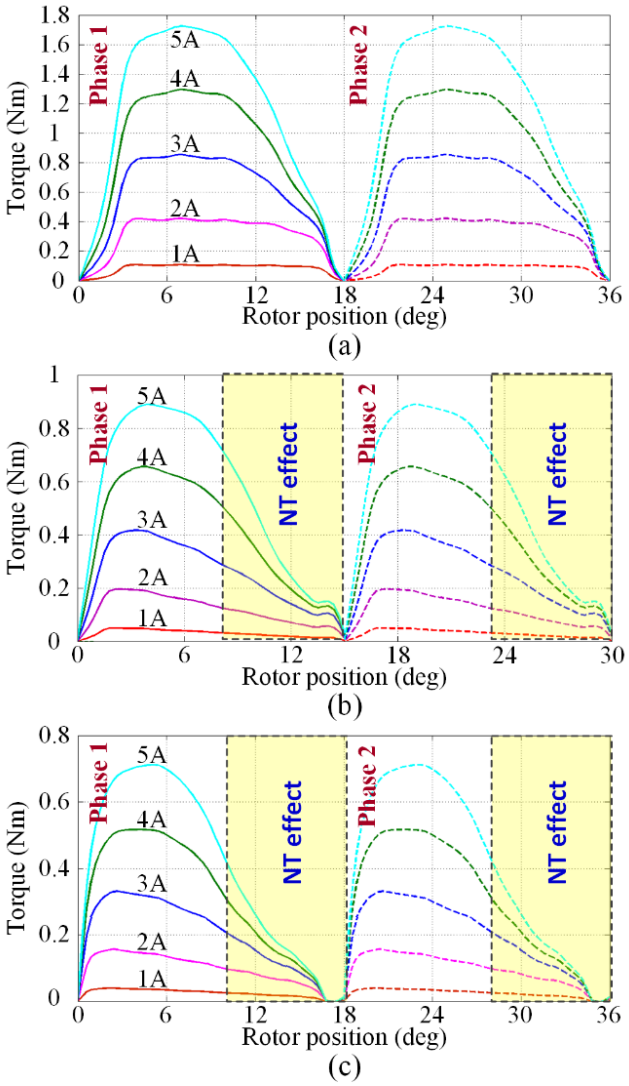

Figure 2.14: Comparison of torque-angle characteristics of (a) 8/10 TPSRM, (b) 9/12 TPSRM and (c) 6/10 TPSRM

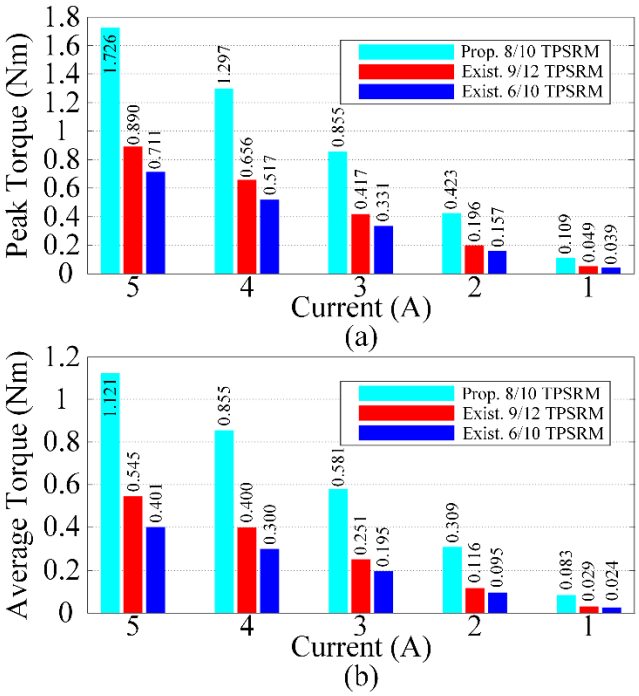

Figure 2.15: Comparisons of SRMs: (a) peak torque and (b) average torque for different stator currents.

Comparison of the torque densities, as given in Fig. 2.16(a), illustrate the superiorities of the proposed motor. Moreover, a new efficiency index is defined as the ratio of torque density to the number of windings per phase (TWP) as in below:

$$TWP = \frac{torque\ density}{number\ of\ windings\ per\ phase} \tag{2.9}$$

Fig. 2.16(b) illustrates the TWP index for the three motors which reveals the superiorities of the proposed TPSRM. The other interesting point is that the TWP of the 6/10 TPSRM is greater than that of the 9/12 TPSRM, although the torque density of the 9/12 TPSRM is greater than that of the 6/10 TPSRM. As in Table 2.2, copper loss of the proposed motor is a bit higher, reflecting the its topological ability to provide larger winding area, but the utilized iron and associated core loss is smaller. In a nutshell, the proposed motor shows higher torque to weight ratio, torque to volume ratio and efficiency.

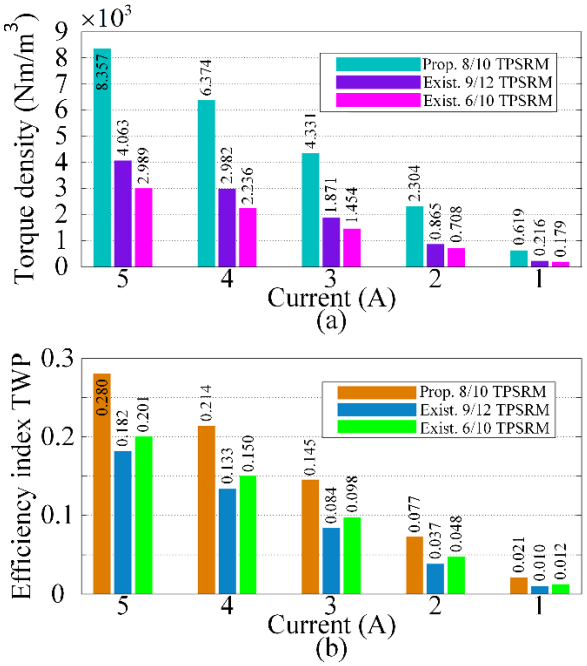

Figure 2.16: Intelligent comparisons of SRMs: (a) torque density and (b) efficiency index TWP for different stator currents.

Table 2.2: Comparison of characteristics

Parameter	8/10 SRM	9/12 SRM	6/10 SRM
iron weight (kg)	0.618	0.656	0.559
copper weight (kg)	0.14	0.105	0.07
average Torque (Nm) at 5A	1.121	0.545	0.401
torque to weight ratio (Nm/kg)	1.479	0.716	0.637
copper loss (W)	12.34	9.77	7.2
core loss (W)	0.356	1.9	1.2
output power (W)	117.39	57.07	41.99
efficiency (%)	90.24	83.02	83.33

Chapter 3

Flux-Tube Modeling

3.1 Introduction

Both numerical or analytical techniques may be used in the analysis of electrical machines. Numerical approaches like finite element method (FEM), although accurate, are usually expensive and too time-consuming to be used in the design optimizations, while analytical models by providing fast, yet accurate solutions are a very good trade-off between accuracy and the required time—useful in preliminary design stages.

Analytical frameworks for analysis of electrical machines may be performed using the solution of Laplace's and Poison's equations [18], or by employing flux-tube based techniques [31]-[34]. The former, although very powerful, might be complicated for many geometries, incapable of taking iron saturation into account, while the latter is usually simpler and effective in many configurations without any symmetry, and is able to account for iron saturation and most material properties, e.g. both PM characteristics. In this chapter, a new flux-tube based model for switched reluctance machines, as a very good example, has been developed. Analytical models are the best candidates for design optimization and parametric analysis of electric machines [35] and [36].

3.2 Flux-tube based modeling and design of switched reluctance machines

This section is about a comprehensive flux-tube based modeling of switched reluctance motors, whose related paper together with experimental verifications will be submitted as soon as possible [37]. The main advantage of the established closed-form framework is the ability to continuously calculate machine characteristics over the entire operating range. Finally, FEM is employed to evaluate effectiveness of the developed model and demonstrate its superiorities over the existing approaches. Fig. 3.1 and Table 3.1 1illustrate

the geometry and specifications of a switched reluctance machine for which the proposed model is developed.

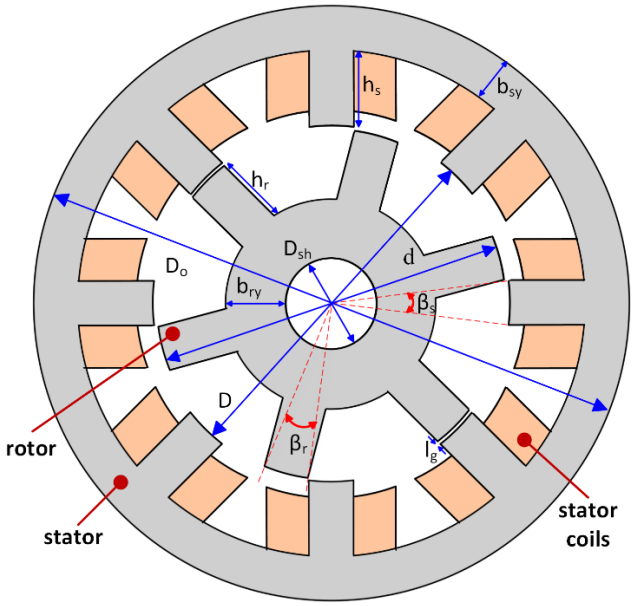

Figure 3.1: Geometry of a typical switched reluctance machine

Table 3.1: Specifications

parameter	symbol	value
stator outer diameter (mm)	D_o	80
stator back iron thickness (mm)	b_{sy}	6
stator pole height (mm)	h_s	10
stator inner diameter (mm)	D	24
air-gap length (mm)	l_g	0.2
rotor outer diameter (mm)	d	23.8
rotor pole height (mm)	h_r	10
rotor back iron thickness (mm)	b_{ry}	7.8
rotor shaft diameter (mm)	D_{sh}	6
stator pole arc (deg)	β_s	15
rotor pole arc (deg)	β_r	15
stack length (mm)	L	25
number of turns per phase	T_{ph}	100
number of phases	q	4
number of rotor poles	P_r	6
number of stator poles	P_s	8
iron material	M19-24G	

3.3 Air-gap flux tubes

To model the machine, four operating regions, shown in Fig. 3.2, are considered:

- **Region a:** no overlapping condition
- **Region b:** the beginning of overlapping
- **Region c**: overlapping condition
- **Region d:** fully aligned condition

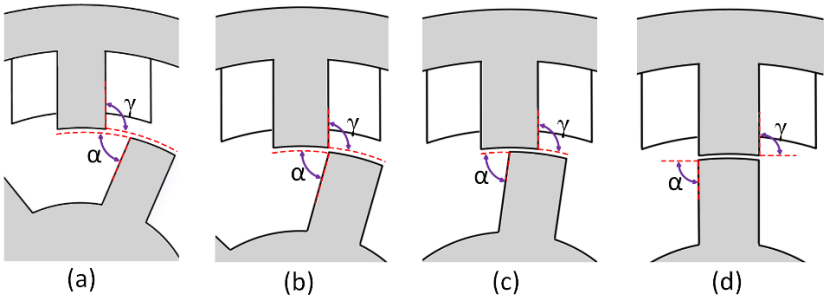

Figure 3.2: Operating regions for modeling: (a) no overlapping, (b) the beginning of overlapping, (c) overlapping and (d) fully aligned conditions

Each row of Figs. 3.3, i.e. (a)-(d), illustrates the scheme for defining the reluctances for each of the mentioned regions. The first column shows the corresponding flux paths within the whole machine (1), the second column provides more detail one (2), and the third column depicts the reluctance elements (3). The air-gap permeances are as in below:

- $\boldsymbol{P_{g1}}$**:** the permeance of the flux from the base of the stator tooth to the upper part of the rotor tooth. The tube width is l_g.
- $\boldsymbol{P_{g2}}$**:** the permeance of the flux from the middle part of the stator tooth to the top of the rotor tooth.
- $\boldsymbol{P_{g3}}$**:** the permeance of the flux from the upper part of the stator tooth to the upper part of the rotor tooth. (it does not appear in the region b)
- $\boldsymbol{P_{g4}}$**:** the permeance of the flux from the top of the stator tooth to the middle section of the rotor tooth.
- $\boldsymbol{P_{g5}}$**:** the permeance of the flux from the upper section of the stator tooth to the base of the rotor tooth.
- $\boldsymbol{P_{g6}}$**:** the permeance of the flux from top of stator tooth to top of rotor tooth. (only in the regions c and d)

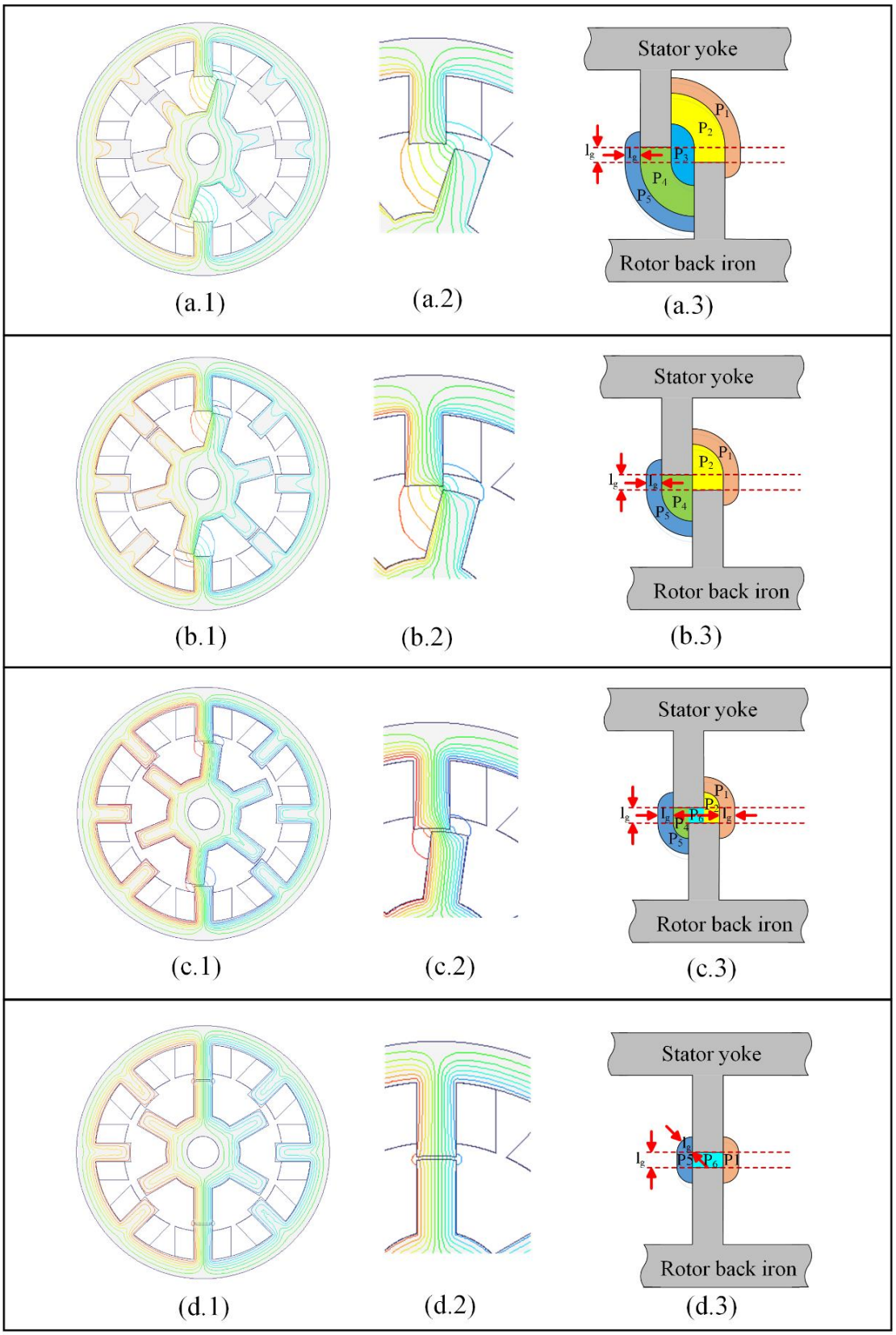

Figure 3.3: Flux lines within the whole machine (1), in the air-gap area (2) and the corresponding reluctances (3) for the four conditions a, b, c and d

In order to achieve a comprehensive model including detailed elements, a separate circuit is considered for each of the mentioned permeances P_{gj} (j=1,2,…,6), as shown in Fig. 3.4. This enables us to more accurately model the iron-part reluctances (stator/ rotor teeth and yokes).

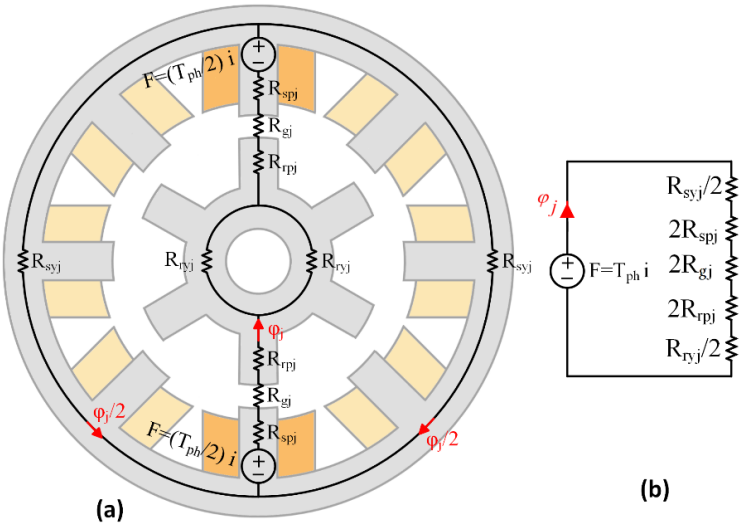

Figure 3.4: (a) MEC and (b) simplified circuit of the jth branch

The rotor pole pitch θ_{rp} and half of it θ_0 are defined as in below:

$$\theta_{rp} = \left(2\pi / N_r\right) \tag{3.1}$$

$$\theta_o = \theta_{rp} / 2 \tag{3.2}$$

As seen in Fig. 3.5, the angular distance between the centers of rotor and stator teeth is θ_0-θ. Although many studies have approximated the angles α and γ to be *90* degrees, herein their actual values are calculated to obtain a higher accuracy as:

$$\alpha = \arccos\left(\frac{\left(\theta_o - \beta_r/2 + \beta_s/2 - \theta\right)\left(D/2\right)}{\left(D/2\right)}\right) = \arccos\left(\left(\theta_o - \beta_r/2 + \beta_s/2 - \theta\right)\right) \tag{3.3}$$

$$\begin{aligned}\gamma &= \pi - \cos^{-1}\left(\frac{\left(\theta_o\left(\theta_o - \beta_s/2 + \beta_r/2 - \theta\right) - \theta\right)\left(D/2 - l_g\right)}{2\left(D/2 - l_g\right)}\right) \\ &= \pi - \cos^{-1}\left[\left(\theta_o\left(\theta_o - \beta_s/2 + \beta_r/2 - \theta\right) - \theta\right)/2\right]\end{aligned} \tag{3.4}$$

It is worth noting that the impact of α and γ on the whole precision arises in cases near the unaligned condition where these angles are faraway from *90* degrees; as seen in Fig. 3.5, reluctance estimations is rough in the linearized model.

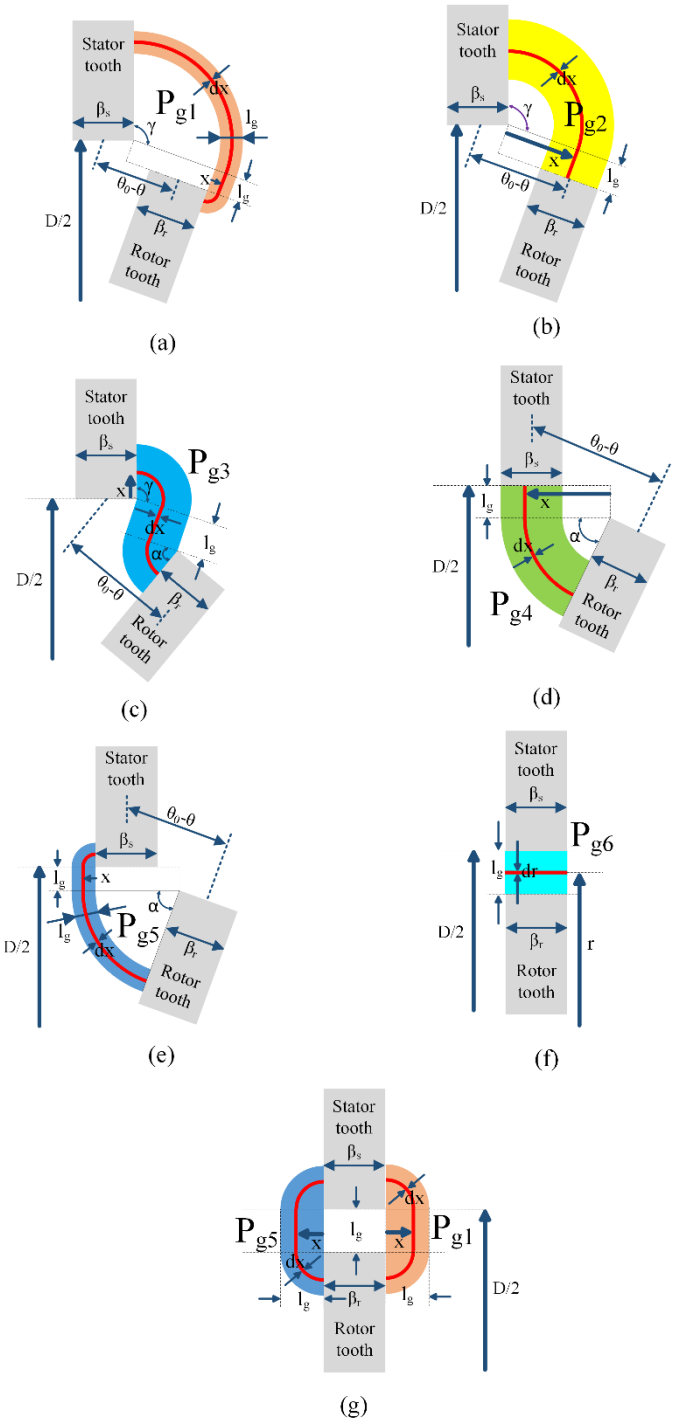

Figure 3.5: Integration paths for (a) Pg1, (b) Pg2, (c) Pg3, (d) Pg4, (e) Pg5, (f) Pg6, (g) Pg1 and Pg5 for region d

According to the integration paths shown in Fig. 3.5, Pg1 to P_{g6} are calculated as:

$$P_{g1}(\theta)=\int_0^{l_g}\frac{\mu_0 L dx}{(\pi/2)x+l_g+\gamma\left(x+(\theta_o-\beta_s/2+\beta_r/2-\theta)(D/2)\right)} \tag{3.5}$$

Executing the integration yields:

$$P_{g1}(\theta)=\frac{\mu_0 L}{(\pi/2+\gamma)}Ln\left\{1+\frac{(\pi/2+\gamma)l_g}{l_g+\gamma(\theta_o-\beta_s/2+\beta_r/2-\theta)(D/2)}\right\} \tag{3.6}$$

We have:

$$P_{g2}(\theta)=\begin{cases}\int_{(\theta_o-\beta_s/2+\beta_r/2-\theta)(D/2)}^{(\theta_o-\beta_s/2+\beta_r/2-\theta)(D/2)}\frac{\mu_0 L dx}{\gamma x+\lg}; & 0\le\theta\le\theta_o-(\beta_r+\beta_s)/2\\ \int_0^{(\theta_o-\beta_s/2+\beta_r/2-\theta)(D/2)}\frac{\mu_0 L dx}{\gamma x+\lg}; & \theta_o-(\beta_r+\beta_s)/2\le\theta\le\theta_o\end{cases} \tag{3.7}$$

Executing the integration yields:

$$P_{g2}(\theta)=\begin{cases}\frac{\mu_0 L}{\gamma}ln\left\{1+\frac{\gamma\beta_r(D/2)}{\gamma\left(\theta_o-\frac{\beta_s}{2}-\frac{\beta_r}{2}-\theta\right)\left(\frac{D}{2}\right)+l_g}\right\} & ;\ 0\le\theta\le\theta_o-(\beta_r+\beta_s)/2\\ \frac{\mu_0 L}{\gamma}ln\left\{1+\gamma\left(\theta_o-\frac{\beta_s}{2}+\frac{\beta_r}{2}-\theta\right)\left(\frac{D}{2}\right)/l_g\right\} & ;\ \theta_o-(\beta_r+\beta_s)/2\le\theta\le\theta_o\end{cases} \tag{3.8}$$

Also,

$$P_{g3}(\theta)=\begin{cases}\int_0^{(\theta_o-\beta_s/2-\beta_r/2-\theta)(D/2-l_g/2)}\frac{\mu_0 L dx}{\gamma x+l_g+\alpha x}=\int_0^{(\theta_o-\beta_s/2-\beta_r/2-\theta)}\frac{\mu_0 L dx}{\pi x+l_g} & ;\ 0\le\theta\le\theta_o-(\beta_r+\beta_s)/2\\ 0 & ;\theta_o-(\beta_r+\beta_s)/2\le\theta\le\theta_o\end{cases} \tag{3.9}$$

Executing the integration yields:

$$P_{g3}(\theta)=\begin{cases}\dfrac{\mu_0 L}{(\alpha+\gamma)}Ln\left\{1+\dfrac{(\alpha+\gamma)(\theta_o-\beta_s/2-\beta_r/2-\theta)(D-l_g)/2}{l_g}\right\}; & 0\le\theta\le\theta_o-(\beta_r+\beta_s)/2\\ 0 & ;\ \theta_o-(\beta_r+\beta_s)/2\le\theta\le\theta_o\end{cases} \tag{3.10}$$

$$P_{g4}(\theta)=\begin{cases}\displaystyle\int_{(\theta_o-\beta_r/2-\beta_s/2-\theta)(D/2-l_g)}^{(\theta_o-\beta_r/2+\beta_s/2-\theta)(D/2-l_g)}\frac{\mu_0 L\,dx}{\alpha x+l_g}; & 0\le\theta\le\theta_o-(\beta_r+\beta_s)/2\\ \displaystyle\int_{0}^{(\theta_o-\beta_r/2+\beta_s/2-\theta)(D/2-l_g)}\frac{\mu_0 L\,dx}{\alpha x+l_g}; & \theta_o-(\beta_r+\beta_s)/2\le\theta\le\theta_o\end{cases} \tag{3.11}$$

it yields:

$$P_{g4}(\theta)=\begin{cases}\dfrac{\mu_0 L}{\alpha}ln\left\{1+\dfrac{\alpha\beta_r(D/2-l_g)}{\alpha\left(\theta_o-\dfrac{\beta_r}{2}-\dfrac{\beta_s}{2}-\theta\right)\left(\left(\dfrac{D}{2}\right)-l_g\right)+l_g}\right\}; & 0\le\theta\le\theta_o-(\beta_r+\beta_s)/2\\ \dfrac{\mu_0 L}{\alpha}Ln\left\{1+\alpha(\theta_o-\beta_r/2+\beta_s/2-\theta)(D/2-l_g)/l_g\right\}; & \theta_o-(\beta_r+\beta_s)/2\le\theta\le\theta_o\end{cases} \tag{3.12}$$

$$P_{g5}(\theta)=\int_0^{l_g}\frac{\mu_0 L\,dx}{\dfrac{\pi}{2}x+l_g+\alpha\left(x+\left(\theta_o-\dfrac{\beta_r}{2}+\dfrac{\beta_s}{2}-\theta\right)\left(\dfrac{D}{2}-l_g\right)\right)} \tag{3.13}$$

it yields:

$$P_{g5}(\theta)=\frac{\mu_0 L}{(\pi/2+\alpha)}ln\left\{1+\frac{(\pi/2+\alpha)l_g}{l_g+\alpha(\theta_o-\beta_r/2+\beta_s/2-\theta)(D/2-l_g)}\right\} \tag{3.14}$$

$$P_{g6}(\theta)=\begin{cases}0 & ;0\le\theta\le\theta_o-(\beta_r+\beta_s)/2\\ \dfrac{1}{R_{g6}}=\left[\displaystyle\int_{(D/2-l_g)}^{(D/2)}\frac{dr}{\mu_0 Lr\left(\theta-\theta_0+\dfrac{\beta_s}{2}+\dfrac{\beta_r}{2}\right)}\right]^{-1}; & \theta_o-(\beta_r+\beta_s)/2\le\theta\le\theta_o\end{cases} \tag{3.15}$$

so,

$$P_{g6}(\theta)=\begin{cases}0 & ;0\le\theta\le\theta_o-(\beta_r+\beta_s)/2\\ \left[\dfrac{1}{\mu_0 L\left(\theta-\theta_0+\dfrac{\beta_s}{2}+\dfrac{\beta_r}{2}\right)}Ln\left\{1+\dfrac{l_g}{\left(\dfrac{D}{2}-l_g\right)}\right\}\right]^{-1} & ;\ \theta_o-(\beta_r+\beta_s)/2\le\theta\le\theta_o\end{cases} \tag{3.16}$$

According to the integration path shown in Fig. 3.5(g), in the case of fully aligned condition ($\theta=\theta_0$), the P_{g1} and P_{g5} are calculated as in below:

$$\begin{aligned} &If:\quad \alpha=\gamma=90^{\circ}\quad\Rightarrow\\ &P_{g1}(\theta=\theta_o)=P_{g5}(\theta=\theta_o)=\int_0^{l_g}\frac{\mu_0\,L\,dx}{(\pi/2)x+l_g+(\pi/2)x}=\int_0^{l_g}\frac{\mu_0 L\,dx}{\pi x+l_g}\end{aligned} \tag{3.17}$$

We achieve

$$P_{g1}(\theta=\theta_o)=P_{g5}(\theta=\theta_o)=\frac{\mu_0 L}{\pi}Ln(1+\pi) \tag{3.18}$$

3.4 Iron-part Reluctances

Having the permeability of iron, the corresponding reluctance are calculated as in below:

$$R_{spj}=l_{spj}/\mu_{spj}A_{spj} \tag{3.19}$$

$$R_{rpj}=l_{rpj}/\mu_{rpj}A_{rpj} \tag{20}$$

$$R_{ryj}=l_{ryj}/\mu_{ryj}A_{ryj} \tag{21}$$

$$R_{syj}=l_{syj}/\mu_{syj}A_{syj} \tag{3.22}$$

Most existing frameworks simplify the modeling by assumptions such as equal areas for the rotor/stator pole reluctances (the whole pole [40] or divided by the number of paths [39]; A_{rp}, A_{sp}), equal areas for rotor/stator yoke reluctances (the whole yoke area or divided by the number of paths; A_{ry}, A_{sy}) [39], equal lengths for rotor/stator pole reluctances (the whole pole height; h_s, h_r) [40].

In our model, by defining the factor K_j, it has been assumed that the area associated with each reluctance element is proportional to the corresponding flowing flux as in below:

$$mmf_g \approx \frac{\varphi_{g1}}{P_{g1}} \approx \frac{\varphi_{g2}}{P_{g2}} \approx ... \approx \frac{\varphi_{gj}}{P_{gj}} \;\Rightarrow\; K_j(\theta) = \frac{\varphi_{gj}(\theta)}{\varphi_t(\theta)} = \frac{P_{gj}(\theta)}{P_t(\theta)}, \mathrm{j} = 1,\ldots,6 \tag{3.23}$$

where, P_t is the total permeance by the following:

$$P_t(\theta) = \sum_{j=1}^{6} P_{gj}(\theta) \tag{3.24}$$

Thus, effective areas associated with the j^{th} branch are calculated as:

$$A_{spj}(\theta) = K_j(\theta)\, A_{sp} \tag{3.25}$$

$$A_{rpj}(\theta) = K_j(\theta)\, A_{rp} \tag{3.26}$$

$$A_{syj}(\theta) = K_j(\theta)\, A_{sy} \tag{3.27}$$

$$A_{ryj}(\theta) = K_j(\theta)\, A_{ry} \tag{3.28}$$

where A_{spj}, A_{rpj}, A_{syj} and A_{ryj} are respectively total areas of stator pole, rotor pole, stator yoke and rotor yoke, as in below:

$$A_{sp} = L(\beta_s D/2) \tag{3.29}$$

$$A_{rp} = L\left(\beta_r\left(D/2 - l_g\right)\right) \tag{3.30}$$

$$A_{sy} = L b_{sy} \tag{3.31}$$

$$A_{ry} = L b_{ry} \tag{3.32}$$

Relatively accurate values of the lengths of all stator/rotor pole reluctances are calculated. According to Fig. 3.6(a), the lengths of the j^{th} stator and rotor yokes reluctances are calculated as in below:

$$l_{syj} = b_{sy}/2 + \pi\left(D_o - b_{sy}\right)/2 + b_{sy}/2 \tag{3.33}$$

$$l_{ryj} = b_{ry}/2 + \pi\left(D_{sh} + b_{ry}\right)/2 + b_{ry}/2 \tag{3.34}$$

According to Fig. 3.6(b), the effective lengths of stator pole reluctance for each branch is determined as in the following:

$$l_{sp1} = h_s - \left[\left(\theta_o - \beta_s / 2 + \beta_r / 2 - \theta \right) \left(D / 2 \right) + \left(l_g / 2 \right) \right] \tag{3.35}$$

$$l_{sp2} = h_s - \left[\left(\theta_o - \beta_s / 2 - \theta \right) \left(D / 2 \right) \right] \tag{3.36}$$

$$l_{sp3} = h_s - \left[\left(\theta_o - \beta_s / 2 - \beta_r / 2 - \theta \right) \left(D / 2 \right) / 2 \right] \tag{3.37}$$

$$l_{sp4} = h_s \tag{3.38}$$

$$l_{sp5} = h_s - \left(l_g / 2 \right) \tag{3.39}$$

$$l_{sp6} = h_s \tag{3.40}$$

Similarly, for the rotor, we have:

$$l_{rp1} = h_r - \left(l_g / 2 \right) \tag{3.41}$$

$$l_{rp2} = h_r \tag{3.42}$$

$$l_{rp3} = h_r - \left[\left(\theta_o - \beta_r / 2 - \beta_s / 2 - \theta \right) \left(D / 2 - l_g \right) / 2 \right] \tag{3.43}$$

$$l_{rp4} = h_r - \left[\left(\theta_o - \beta_r / 2 - \theta \right) \left(D / 2 - l_g \right) \right] \tag{3.44}$$

$$l_{rp5} = h_r - \left[\left(\theta_o - \beta_r / 2 + \beta_s / 2 - \theta \right) \left(D / 2 - l_g \right) + \left(l_g / 2 \right) \right] \tag{3.45}$$

$$l_{rp6} = h_r \tag{3.46}$$

Finally, the flux flowing into the j^{th} branch is determined as:

$$\varphi_{gj} = T_{ph} i / R_{eqj} \tag{3.47}$$

where, R_{eqj} is the equivalent reluctance given below

$$R_{eqj} = \left(1 / 2 \right) \left(R_{syj} + R_{ryj} \right) + 2 \left(R_{spj} + R_{gj} + R_{rpj} \right) \tag{3.48}$$

Air-gap flux density within the j^{th} branch is calculated as:

$$B_{gj} = \varphi_{gj} / A_{gj} \tag{3.49}$$

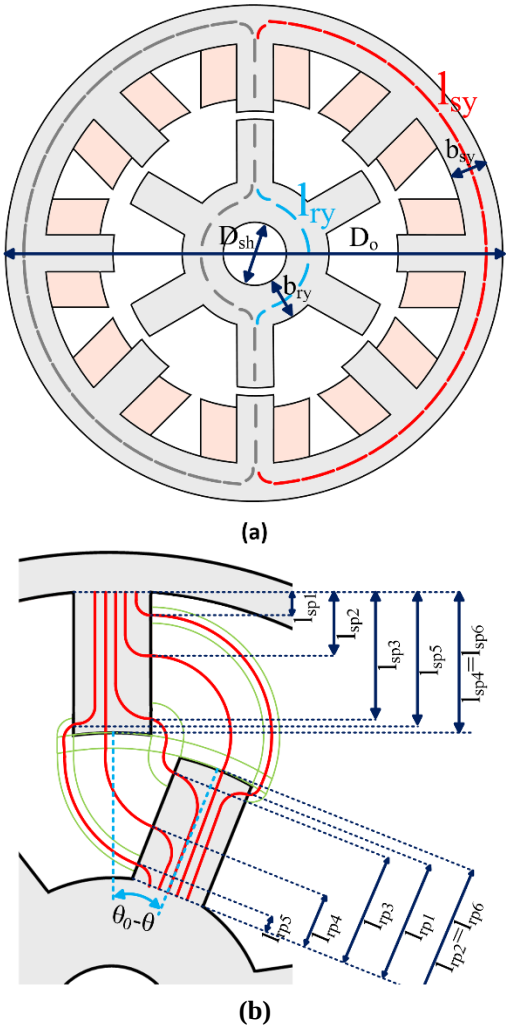

Figure 3.6: Flux lines in (a) teeth and (b) yokes of stator and rotor.

3.5 Nonlinear Algorithm

An iterative algorithm, whose diagram is shown in Fig. 3.7, is used to calculate the permeability of iron reluctances. Assigning an initial value, air-gap flux density for each branch is calculated. Then, the corresponding flux densities within the stator pole, rotor pole, stator yoke and rotor yoke are determined as in below:

$$\varphi_{spj} = \varphi_{gj} \quad \Rightarrow \quad B_{spj} = B_{gj} A_{gj} / A_{spj} \tag{3.50}$$

$$\varphi_{rpj} = \varphi_{gj} \quad \Rightarrow \quad B_{rpj} = B_{gj} A_{gj} / A_{rpj} \tag{3.51}$$

$$\varphi_{syj} = \varphi_{gj} \quad \Rightarrow \quad B_{syj} = B_{gj} A_{gj} / 2A_{syj} \tag{3.52}$$

$$\varphi_{ryj} = \varphi_{gj} \quad \Rightarrow \quad B_{ryj} = B_{gj} A_{gj} / 2A_{ryj} \tag{3.53}$$

where areas associated with air-gap flux tubes are as follows:

$$A_{g1} = Ll_g \tag{3.54}$$

$$A_{g2} = \begin{cases} L\beta_r\left(D - l_g\right), 0 \le \theta \le \theta_o - \left(\beta_r + \beta_s\right)/2 \\ L\left(\theta_0 - \theta\right)\left(D - l_g\right), \theta_o - \left(\beta_r + \beta_s\right)/2 \le \theta \le \theta_o \end{cases} \tag{3.55}$$

$$A_{g3} = \begin{cases} L\left(\theta_0 - \theta - \beta_r\right), 0 \le \theta \le \theta_o - \left(\beta_r + \beta_s\right)/2 \\ 0, \theta_o - \left(\beta_r + \beta_s\right)/2 \le \theta \le \theta_o \end{cases} \tag{3.56}$$

$$A_{g4} = \begin{cases} L\beta_s D, 0 \le \theta \le \theta_o - \left(\beta_r + \beta_s\right)/2 \\ L\left(\theta_0 - \theta\right)D, \theta_o - \left(\beta_r + \beta_s\right)/2 \le \theta \le \theta_o \end{cases} \tag{3.57}$$

$$A_{g5} = Ll_g \tag{3.58}$$

$$A_{g6} = \begin{cases} 0, 0 \le \theta \le \theta_o - \left(\beta_r + \beta_s\right)/2 \\ L\left(\beta_r - \left(\theta_0 - \theta\right)\right), \theta_o - \left(\beta_r + \beta_s\right)/2 \le \theta \le \theta_o \end{cases} \tag{3.59}$$

Afterward, the new relative permeabilities are found using the saturation curve [31] and [38]. First, the auxiliary permeabilities are directly extracted from the *B*-*H* curve:

$$\hat{\mu}_{spj}^{(k)} = B_{spj}^{(k-1)} / \mu_0 H_{spj}^{(k-1)} \tag{3.60}$$

$$\hat{\mu}_{rpj}^{(k)} = B_{rpj}^{(k-1)} / \mu_0 H_{rpj}^{(k-1)} \tag{3.61}$$

$$\hat{\mu}_{syj}^{(k)} = B_{syj}^{(k-1)} / \mu_0 H_{syj}^{(k-1)} \tag{3.62}$$

$$\hat{\mu}_{ryj}^{(k)} = B_{ryj}^{(k-1)} / \mu_0 H_{ryj}^{(k-1)} \tag{3.63}$$

Then, the actual relative permeabilities are determined by:

$$\mu_{spj}^{(k)} = [\hat{\mu}_{spj}^{(k)}]^d [\mu_{spj}^{(k-1)}]^{1-d} \tag{3.64}$$

$$\mu_{rpj}^{(k)} = [\hat{\mu}_{rpj}^{(k)}]^d [\mu_{rpj}^{(k-1)}]^{1-d} \tag{3.65}$$

$$\mu_{syj}^{(k)} = [\hat{\mu}_{syj}^{(k)}]^d [\mu_{syj}^{(k-1)}]^{1-d} \tag{3.66}$$

$$\mu_{ryj}^{(k)} = [\hat{\mu}_{ryj}^{(k)}]^d [\mu_{ryj}^{(k-1)}]^{1-d} \tag{3.67}$$

where *d* is the damping constant (chosen 0.15). The stop criteria is as in below:

$$\left|[\mu_{spj}^{(k)} - \mu_{spj}^{(k-1)}] / \mu_{spj}^{(k-1)}\right| \leq \varepsilon \tag{3.68}$$

$$\left|[\mu_{rpj}^{(k)} - \mu_{rpj}^{(k-1)}] / \mu_{rpj}^{(k-1)}\right| \leq \varepsilon \tag{3.69}$$

$$\left|[\mu_{syj}^{(k)} - \mu_{syj}^{(k-1)}] / \mu_{syj}^{(k-1)}\right| \leq \varepsilon \tag{3.70}$$

$$\left|[\mu_{ryj}^{(k)} - \mu_{ryj}^{(k-1)}] / \mu_{ryj}^{(k-1)}\right| \leq \varepsilon \tag{3.71}$$

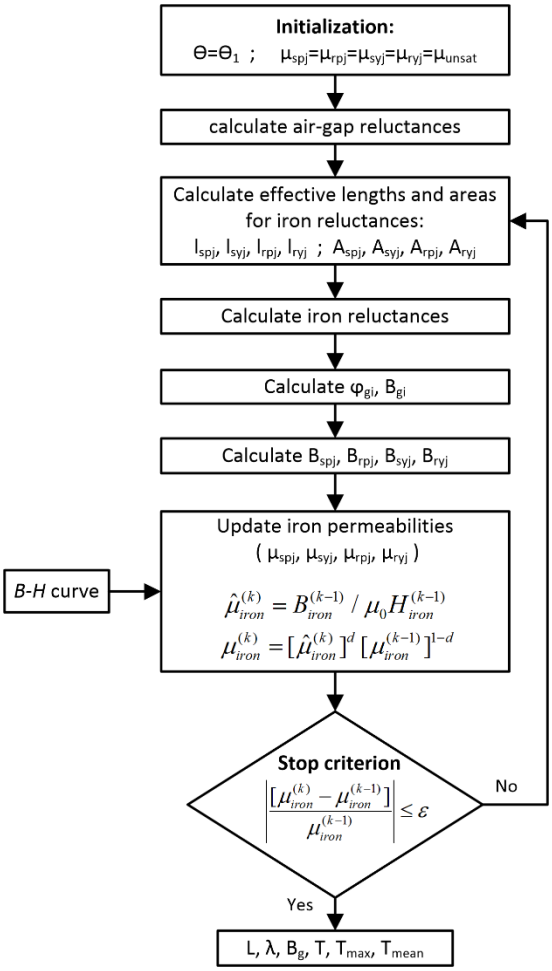

Figure 3.7: Nonlinear algorithm

3.6 Flux Linkage and Inductance Calculations

The inductance associated with each branch is calculated as:

$$L_j(\theta, i) = T_{ph}\varphi_{gj} / i \tag{3.72}$$

Thus, the total inductance and flux linkage as a function of θ are determined by:

$$L\left(\theta,i\right)=\sum_{j=1}^{6}L_j\left(\theta,i\right) \tag{3.73}$$

$$\lambda\left(\theta,i\right)=L\left(\theta,i\right)\ i=i\sum_{j=1}^{6}L_j\left(\theta,i\right) \tag{3.74}$$

3.7 Flux Density Distribution

By dividing the developed MEC into six separate branches, the flux flowing into each branch and then the step-wise approximation of flux densities is obtained as in below:

$$B_{gj}=\varphi_{gj}/A_{gj}\qquad (\mathrm{j}=1,2,...,6) \tag{3.75}$$

3.8 Torque Calculations

Co-energy is calculated as follows:

$$W_c\left(\theta,i\right)=\frac{1}{2}L\left(\theta\right)\cdot i^2 \tag{3.76}$$

The developed torque under a constant current is determined by:

$$T\ \left(\theta,i\ \right)=\left.\frac{\partial W_c\left(\theta,i\ \right)}{\partial\theta}\right|_{i\ =const} \tag{3.77}$$

into which by substituting (76), we achieve the following:

$$T\left(\theta,i\right)=\frac{1}{2}i^2\cdot\frac{dL\left(\theta\right)}{d\theta} \tag{3.78}$$

3.9 Evaluation

Herein, characteristics of a typical machine, whose specifications are given in Table I, are extracted and then evaluated and compared with those obtained from FEM as well as the existing model [39]. Fig. 3.8 shows the saturation curve of the utilized steel (M19-24G). Fig. 3.9 illustrates the flux linkage characteristic of the machine for different rotor positions from unaligned to aligned conditions, obtained by the proposed model, existing model and FEM, illustrating the higher accuracy of the proposed model. The air-gap flux density

distribution for the four main operating conditions of the machine (aligned, overlapping, beginning of overlapping, unaligned) is shown in Fig. 3.10, in which the comparison with FEM demonstrate its admired precision. Fig. 3.11 shows the torque-angle characteristic of the machine for different stator currents, from which a satisfactory correlation between the analytical framework and FEM can be seen. In addition, it is worth noting that unlike the existing models in which computation are done for discrete points, in the proposed model, these calculations are continuously performed over any range of angular position. In Fig. 3.12, the maximum and mean torques of the machine versus stator current are shown, illustrating a very close agreement with FEM. Table 3.2 lists the discrepancies between models, showing the superiorities of the proposed approach.

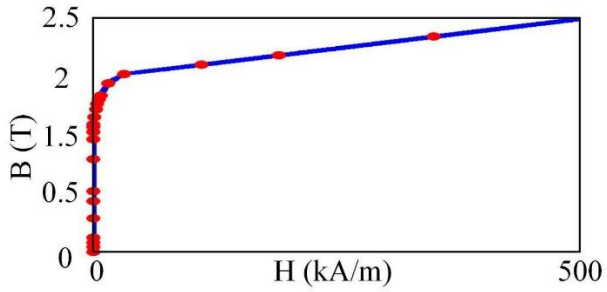

Figure 3.8: B-H characteristic of the utilized steel with grade M19-24G

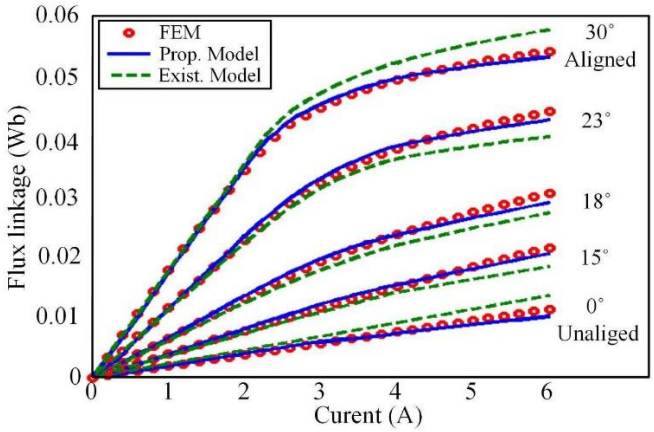

Figure 3.9: Flux linkage characteristics at different rotor positions

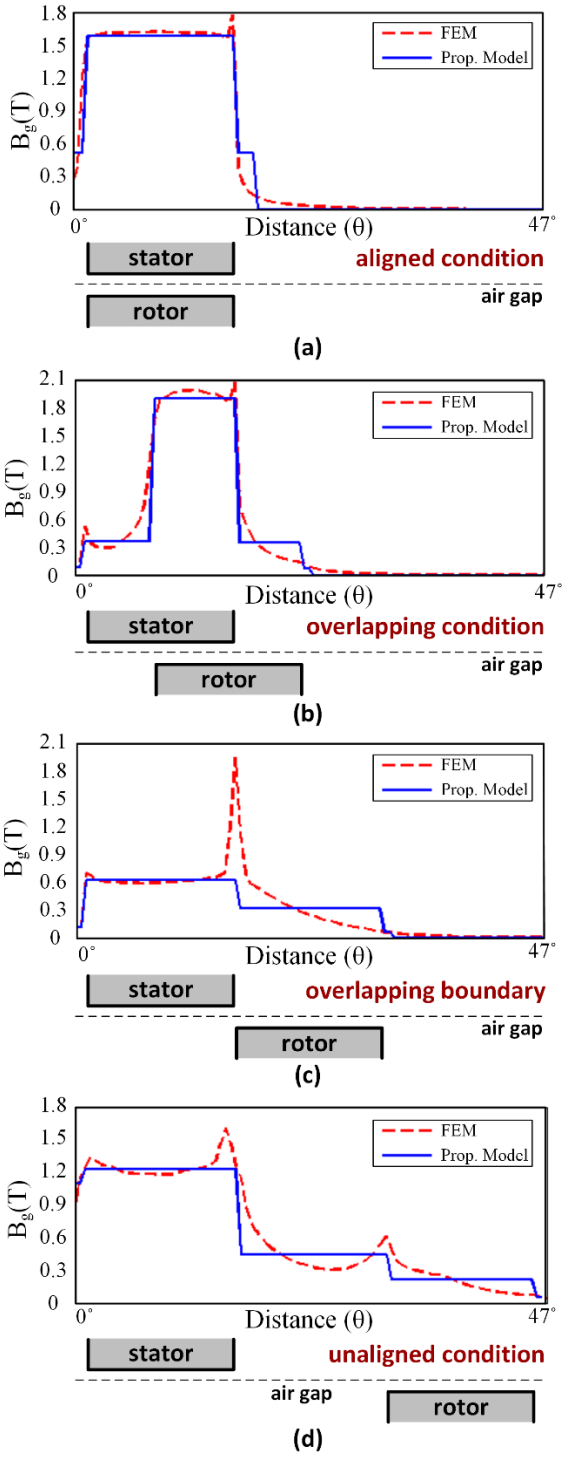

Figure 3.10: Air-gap flux density distribution at different positions

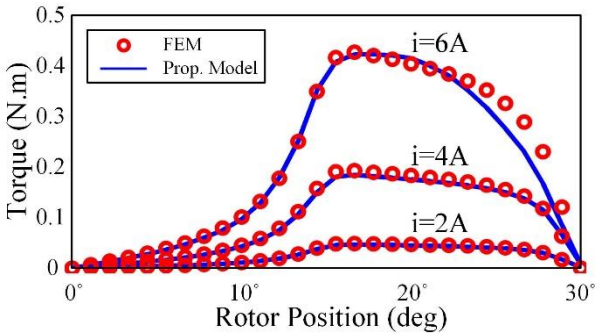

Figure 3. 11: Torque-angle characteristics of the machine

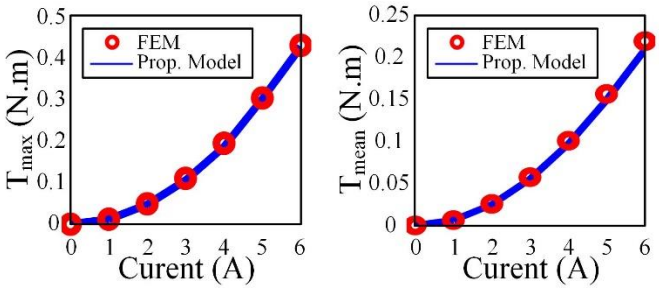

Figure 3.12: Maximum torque-current and average torque-current characteristics

Table 3.2: Comparison of characteristics

Angle (deg)	Proposed model (%)	Existing model (%)
0	10.61	20.35
15	4.65	14.41
18	5.22	10.78
23	3.16	9.27
30	1.84	6.46

Chapter 4

Analytical Framework for Radial-Flux Magnetically-Geared Machines

4.1 Introduction and Machine geometry

Almost more works has been done in the study of magnetic gears and magnetically-geared machines by finite element analysis than using analytical methods, so there is still a big demand for the modeling of magnetic gears and specially magnetically-geared machines. Such can be used in the investigation of the nature of the machine as well as preliminary design stages and optimizations. A magnetic equivalent circuit is presented for magnetic gears very recently [16]-[17] which is a nice contribution to the field, but a set of formulas and matrices has to be solved for each set of machine parameters. Another valuable work is [18], in which a magnetic gear has been modeled by solving Laplace's and Poison's equation; the accuracy of the framework is not very good and generally, such models do not have a flexibility in dealing with complex geometries. The books [41]-[43] are great one on electromagnetic study of electric machines. Another valuable piece on permanent magnet machines is [44]

In this chapter, we are trying to propose an analytical framework and closed-form expressions for magnetically-geared machines that can be employed in the preliminary design stages of the device as well as analysis and performance predictions. This analytical models can also be utilized in design optimizations. Fig. 4.1 shows the cross section of an inside-out radial-flux magnetically-geared synchronous machine. It consists of three main parts: the stator, the modulator rotor and the permanent magnet rotor; either of the rotors can be the stationary part while the other part will be the rotating part. The stator, having any type of winding, is the inner part of the machine, a series of alternating surface permanent magnets are used on the inner side of the outer back-iron, and the modulator ring is placed in between.

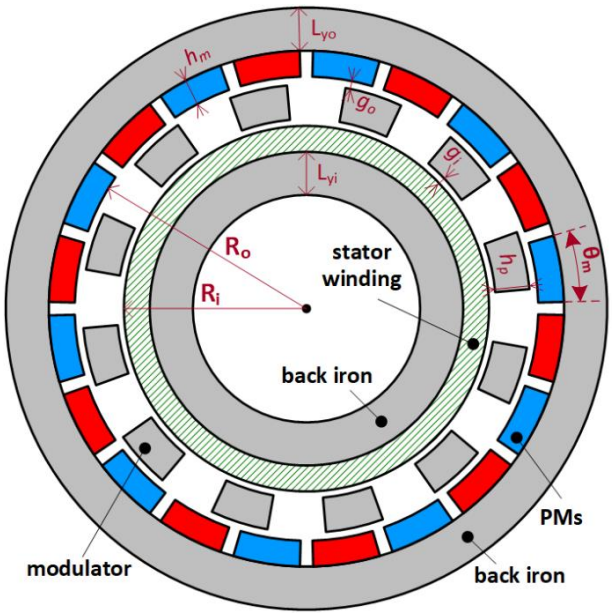

Figure 4.1: Cross section of an inside-out radial-flux magnetically-geared machine.

Table 4.1 illustrates any symbol in the Fig. 4.1. It is seen that there is still a relationship between the stator pole pairs (consider P_s=2), PM rotor pole pairs (P_m=10) and the number of flux modulators (P_p=12). we have:

$$P_p = P_m + P_s \tag{4.1}$$

Table. 4.1: Geometric parameters of the machine.

Parameter	Symbol
inner air-gap	g_i
outer air-gap	g_o
modulator height	h_p
permanent magnet height	h_m
stator pole pairs	P_s
PM pole pairs	P_m
number of modulators	P_{mod}
outer radius of stator (after applying carter's coefficient)	R_i
inner radius of PMs	R_o
inner yoke thickness	L_{yi}
outer yoke thickness	L_{yo}
PM arc	θ_m

4.2 Linearly expansion of the geometry

In order to easily illustrate the ideas and perform the calculations, the machine geometry has been expanded linearly along the average radius of the air-gap given below:

$$R_{av} = \frac{R_i + R_o}{2} \tag{4.2}$$

The linearly expanded geometry of the machine is shown in Fig. 4.2.

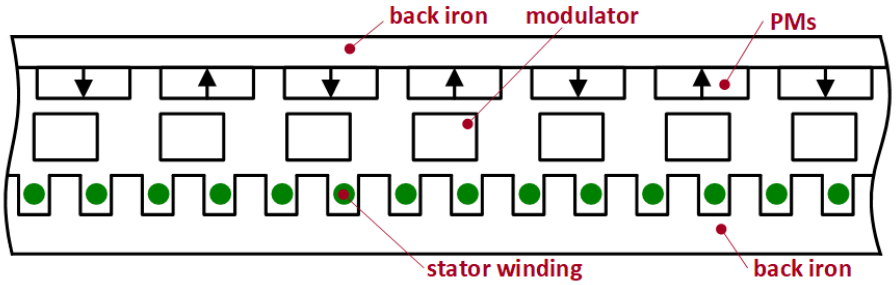

Figure 4.2: Linearly expanded geometry of the machine in slotted model.

4.3 Carter's coefficient and slot modeling

In a slotted-stator machine, the slots can be modeled by carter's coefficient [44]. Fig. 4.3 shows the flux lines and magnetic flux density distribution in an air-gap having slotted-stator on the bottom side and surface-mounted permanent magnets for the sake of modeling on the other side. It is seen that the flux lines which are facing the stator teeth take a shorter path—almost the air-gap length—, while those facing the stator slots take a longer path; therefore, the effective air-gap is larger than the physical air-gap.

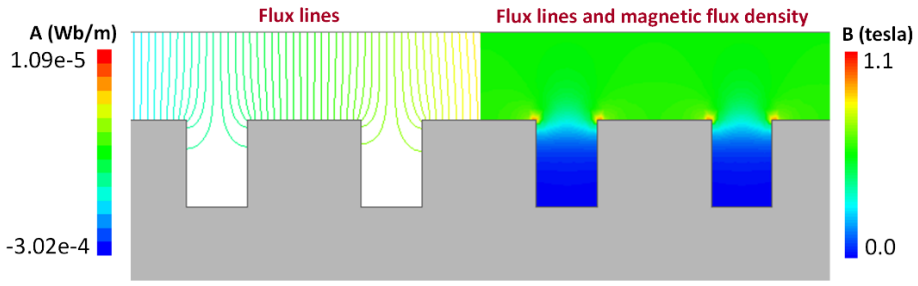

Figure 4.3: flux lines and magnetic flux density distribution in an air-gap having slots.

In order to account for the effect of the two mentioned regions, we employ a slot pitch of the stator including a tooth and a slot. The associated region is also modeled with proper

boundary conditions as in Fig. 4.4 to solve the Poisson's equation for magnetic vector potential *A* in a region without any current. In a 2d problem, vector potential as in below:

$$\nabla^2 A_z = \frac{\partial^2 A_z}{\partial x^2} + \frac{\partial^2 A_z}{\partial y^2} = 0 \tag{4.3}$$

It is worth noting that in a two-dimensional problem, magnetic vector potential $A_z(x,y)$ only has z-component while magnetic flux density and magnetic field intensity have x- and y-components. We have:

$$\vec{A} = A_z \, \hat{a}_z \tag{4.4}$$

$$\vec{B} = B_x \, \hat{a}_x + B_y \, \hat{a}_y = \nabla \times \vec{A} \quad \Rightarrow \quad \vec{B} = (\frac{\partial A_z}{\partial y}, -\frac{\partial A_z}{\partial x}, 0) \tag{4.5}$$

$$\vec{H} = H_x \, \hat{a}_x + H_y \, \hat{a}_y = \frac{1}{\mu}\vec{B} \quad \Rightarrow \quad \vec{H} = (\frac{1}{\mu}B_x, \frac{1}{\mu}B_y, 0) \tag{4.6}$$

We have Neumann boundary condition on the iron boundaries because the flux lines are perpendicular to the iron edges. In other words, magnetic field intensity *H* is zero in an infinitely permeable iron, and due to the continuity of the tangential components H_t where there isn't any surface current density on the boundary, H_t is also zero in the air-gap and on the iron boundaries.

$$\vec{H}^{iron} = 0 \;\Rightarrow\; H_t^{air} = H_t^{iron} = 0 \;\Rightarrow\; \frac{\partial A_z}{\partial n} = 0 \tag{4.7}$$

where n is the normal component of the boundary. We also have Neumann boundary condition the bottom edge of the problem to which the flux lines as well as the magnetic field intensity are perpendicular.

$$H_x = 0 \;\Rightarrow\; \frac{\partial A_z}{\partial y} = 0 \tag{4.8}$$

There is Dirichlet boundary condition on the left and right sides of the air-gap. As in below:

$$A_z\big|_{left} = A_{z1} \tag{4.9}$$

$$A_z\big|_{right} = A_{z2} \tag{4.10}$$

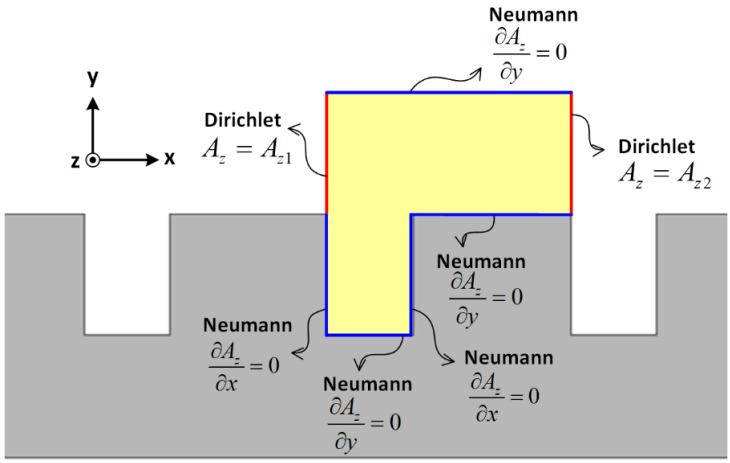

Figure 4.4: (a) Dirichlet and Neumann boundary conditions of the problem

To solve the problem, it is needed to choose two reasonable values for A_{z1} and A_{z2}. Assuming average magnetic flux density of *1 Tesla* in the air-gap, it will be possible to come up with fine values. As shown in Fig. 4.5(a), the net flux passing through a surface *S* enclosed by closed line *C* is the surface integral of magnetic flux density vector *B* over surface *S*, or is the closed line integral of the magnetic vector potential *A* over line C as in below:

$$\varphi = \iint_S \vec{B}.d\vec{s} = \oint_c \vec{A}.d\vec{l} \tag{4.11}$$

It is obtained by substituting *B* in terms of *A* and employing Stokes' theorem. In a 2D problem where *A* is only in the z-direction, flux is easily calculated as in below:

$$\varphi = L\,(A_{z1} - A_{z2})\,L = L\,\Delta A_z \tag{4.12}$$

where A_{z1} and A_{z1} are values of A_z at the two points in the *xy*-plane as shown in Fig. 4.5(b), and *L* is the axial length of the problem in the z-direction. In case of having a uniform magnetic flux density *B* or in approximations, we have:

$$\varphi = L\,w\,B_{av} \tag{4.13}$$

Combining the last two equations, we have:

$$\Delta A_z = w B_{av} \tag{4.14}$$

where $w=w_s+w_t$ in our case.

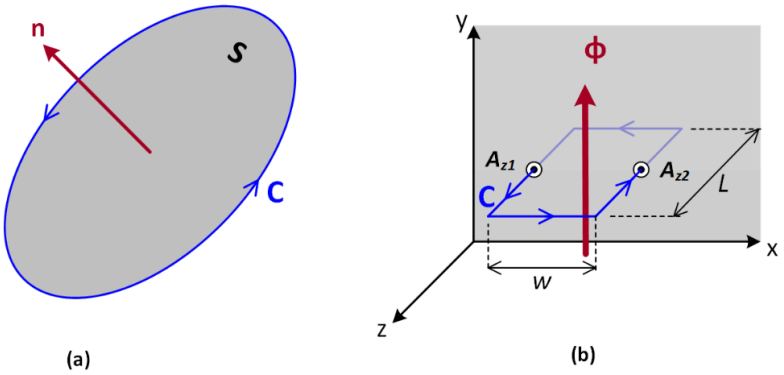

Figure 4.5: Closed line C enclosed by open surface S in (a) 3D problem and (b) 2D problem.

We take $w_s=4\ mm$, $w_t=5\ mm$ and $g=4\ mm$, so for $B_{av}=1\ Tesla$ in the air-gap we have $\Delta A_z=0.009\times1=0.009\ wb/m$. we assign $A_{z1}=0$ to the left side and $A_{z2}=0.009\ wb/m$ to the right side of the air-gap. As shown in Fig. 4.6, flux lines have the expected values and behave the way that we expected, magnetic vector potential is in the z-direction, average magnetic flux density distribution in the air-gap is *1 Tesla*, and magnetic flux density vectors have a downward direction that matches the flux pathing through the surface which is *-0.009 wb* per unit length.

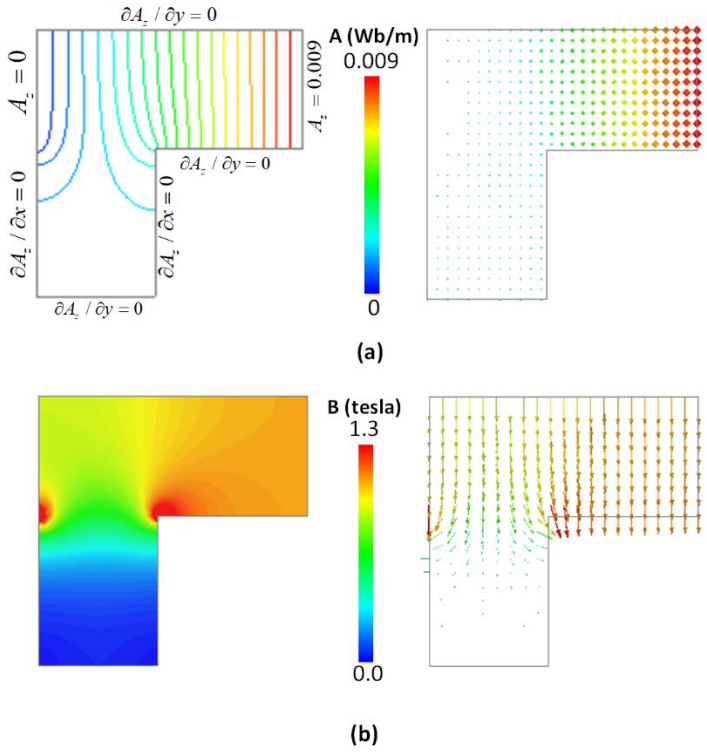

Figure 4.6: Field simulation in one slot pitch region: (a) flux lines and magnetic vector potential and (b) magnetic flux density distribution and vectors.

It is worth noting that the slot depth h_s is large enough that no flux reaches the bottom of the slot and all flux lines are attracted to the sides. Based on the flux lines in the region, the flux tube model is offered to determine the reluctance in an air-gap facing a slotted stator. The permeance P_{g1} is calculated as in below:

$$P_{g1} = \int_0^{w_s/2} \frac{\mu_0 L \, dl}{g_i + \frac{\pi}{2} l} \tag{4.15}$$

We have:

$$P_{g1} = \frac{2\mu_0 L}{\pi} \ln\left(1 + \frac{\pi w_s}{4 g_i}\right) \tag{4.16}$$

The permeance P_{g2} is calculated as in below:

$$P_{g2} = \frac{\mu_0 w_t L}{g_i} \tag{4.17}$$

The total permeance is:

$$P_g = 2P_{g1} + P_{g2} \tag{4.18}$$

We have:

$$P_g = \mu_0 \, L \left\{ \frac{w_t}{g_i} + \frac{4}{\pi} \ln\left(1 + \frac{\pi \, w_s}{4 \, g_i} \right) \right\} \tag{4.19}$$

In case of ignoring the fringing effect due to the slots, the air-gap permeance is:

$$P_g' = \frac{\mu_0 \, w L}{g_i} \tag{4.20}$$

Therefore, the Carter's coefficient is:

$$k_c = \frac{R_g}{R_g'} = \frac{P_g'}{P_g} = \left[1 - \frac{w_s}{w} + \frac{4g}{\pi \, w} \ln\left(1 + \frac{\pi \, w_s}{4 \, g_i} \right) \right]^{-1} \tag{4.21}$$

It is seen that as long as the slot is deep enough, k_c is independent of h_s and is only a function of slot opening w_s, slot pitch w and air-gap length g_{ie}. Finally, as shown in Fig. 4.7(b), an equivalent slotless stator with efficient air-gap length g_{ie} can be employed where

$$g_{ie} = k_c \, g_i \quad ; \; k_c \geq 1 \tag{4.22}$$

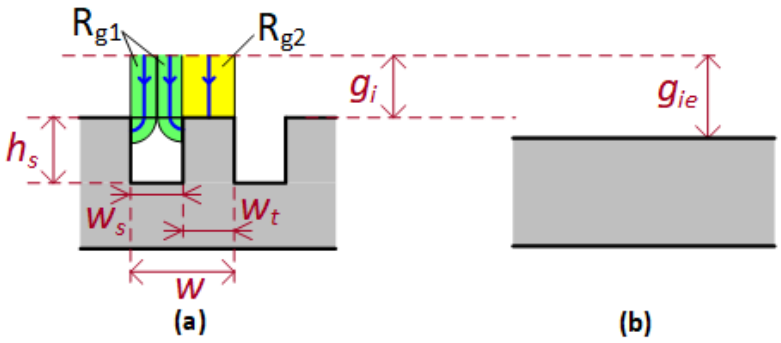

Figure 4.7: (a) flux-tube modeling of an air-gap having slotted stator and (b) equivalent slotless stator with efficient air-gap length.

After applying the Carter's coefficient to the air-gap length and using the equivalent surface current density of the stator winding, we get the original and the expanded geometries of the machine as in Figs 4.8 and 4.9.

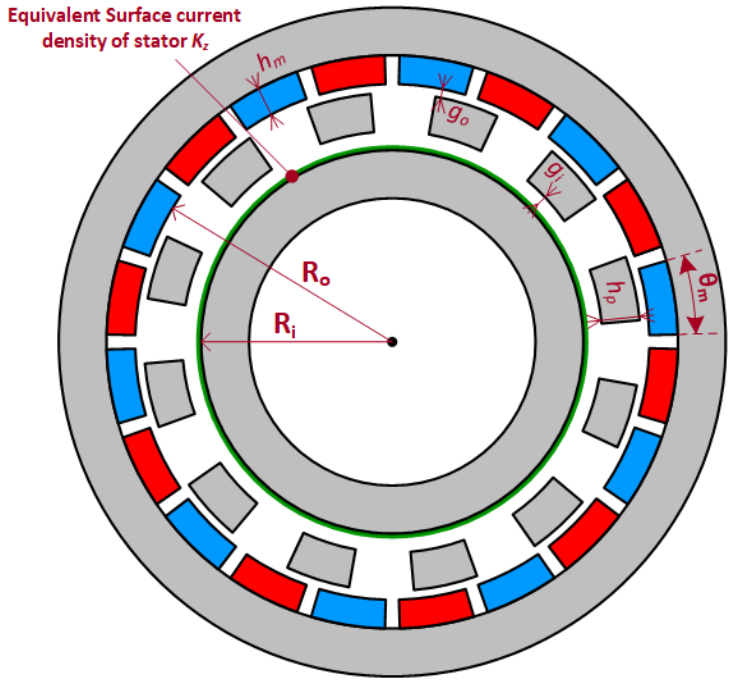

Figure 4.8: Geometry of the machine with an equivalent slotless stator

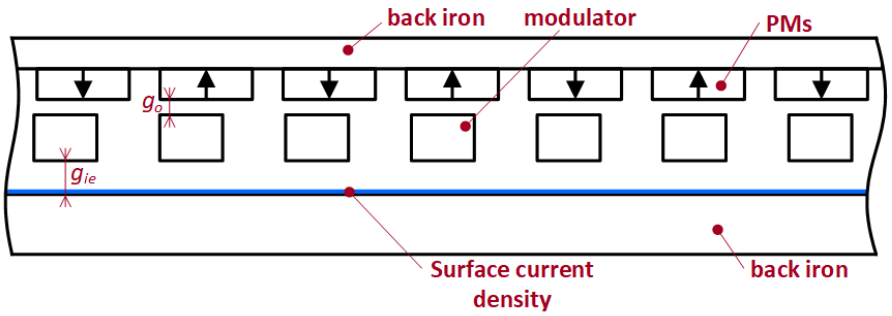

Figure 4.9: Linearly expanded geometry of the machine with an equivalent slotless stator

4.4 Permeance modeling

4.4.1 Simplified model

The air gap permeance relates magnetic flux density distribution to MMF distribution. Here we extract the permeance per unit area, so it has the dimension of H/m^2. The simplest model to approximate the permeance distribution is a square wave model shown in Fig. 4.10 in which we have:

$$\wp_{\max} = \frac{\mu_0}{g_{ie} + g_o + h_m} \tag{4.23}$$

$$\wp_{\min} = \frac{\mu_0}{g_{ie} + h_{\mathrm{mod}} + g_o + h_m} \tag{4.24}$$

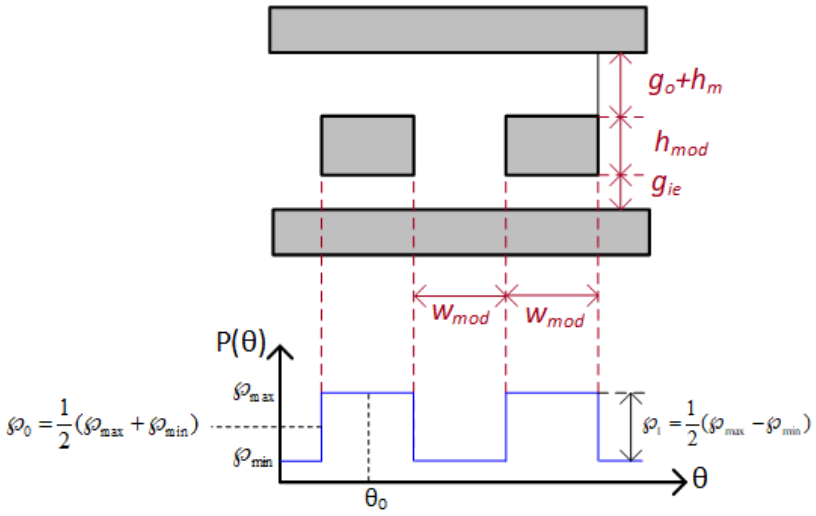

Figure 4.10: Square wave approximation of spatial distribution of the air-gap permeance

The Fourier series representation of the square wave approximation of the permeance is:

$$\wp(\theta) = \frac{1}{2}(\wp_{\max} + \wp_{\min}) + \sum_{n=1}^{+\infty} \frac{4}{n\pi} \sin\left(\frac{n\pi}{2}\right) \frac{1}{2}(\wp_{\max} - \wp_{\min}) \cos n\, p_{\mathrm{mod}}(\theta - \theta_0) \tag{4.25}$$

where

$$\wp_0 = \frac{1}{2}(\wp_{\max} + \wp_{\min}) \tag{4.26}$$

$$\wp_1 = \frac{1}{2}\frac{4}{\pi}(\wp_{\max} - \wp_{\min}) \tag{4.27}$$

The space fundamental of the waveform is:

$$\wp(\theta) = \wp_0 + \wp_1 \cos p_{\text{mod}}(\theta - \theta_0) \tag{4.28}$$

where θ_0 is shown in Fig. 4.10.

4.4.2 Flux-tube model

Flux lines and magnetic flux density distribution in the air-gap region is shown in Fig. 4.11. It is seen that when modulator height is small enough compared to the distance between two adjacent modulators, a part of the flux takes the air path, and when modulator height is large enough compared to the distance between two adjacent modulators, all of the flux take the modulator path. As shown in the latter case, all the magnetic flux tends to take the modulator path after a critical point, and thus P_{min} will be almost constant while equation (4.25) offer a value that is always decreasing with an increase in h_p—the biggest problem with the square wave model explained earlier.

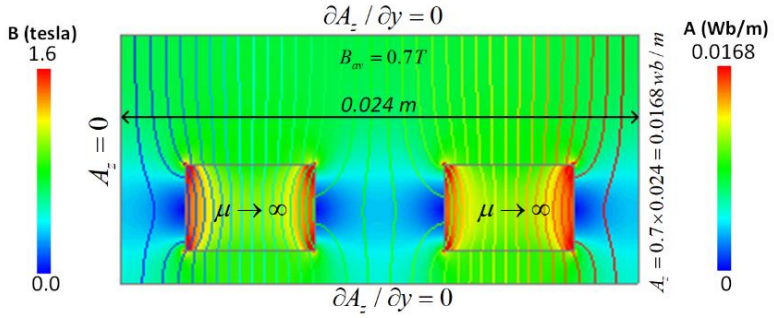

(a)

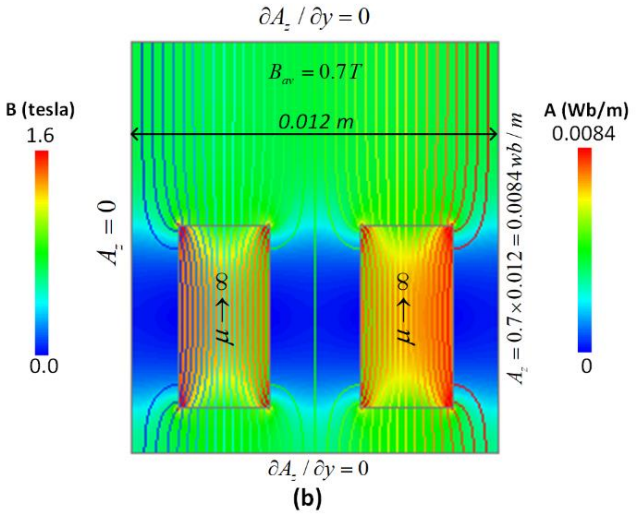

(b)

Figure 4.11: Flux lines and magnetic flux density distribution in the air-gap region (a) when modulator height is small enough compared to the distance between two adjacent modulators that a part of the flux takes the air path and (b) when modulator height is large enough compared to the distance between two adjacent modulators that all of the flux take the modulator path.

To attain a better observation, we take the highlighted region in Fig. 4.12 to be solved. All other the regions are the repetition of this pattern. The boundary conditions are illustrated. We have Neumann boundary condition on the iron edges because it is assumed to be infinitely permeable and thus the flux lines are perpendicular to its surface. We also have Dirichlet boundary condition on the left and right sides of the region.

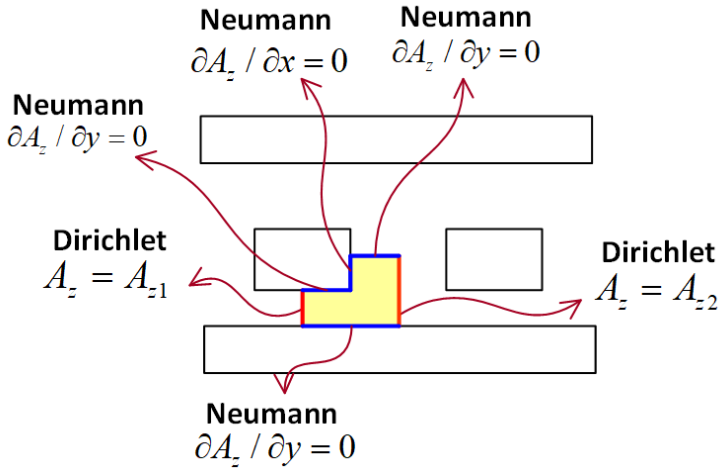

Figure 4.12: (a) Dirichlet and Neumann boundary conditions of the problem

The above problem for the two mentioned conditions has been solved as given in Fig. 4.13. It is seen that when modulator height is small enough compared to the distance between two adjacent modulators, a part of the flux lines takes the air path and there exists a non-zero magnetic flux density there, and when modulator height is large enough compared to the distance between two adjacent modulators, all of the flux lines take the modulator path and magnetic flux density distribution is zero in the top of the air region. Therefore, there will be two flux tube models but what is the boundary on which we have to switch between the two models?

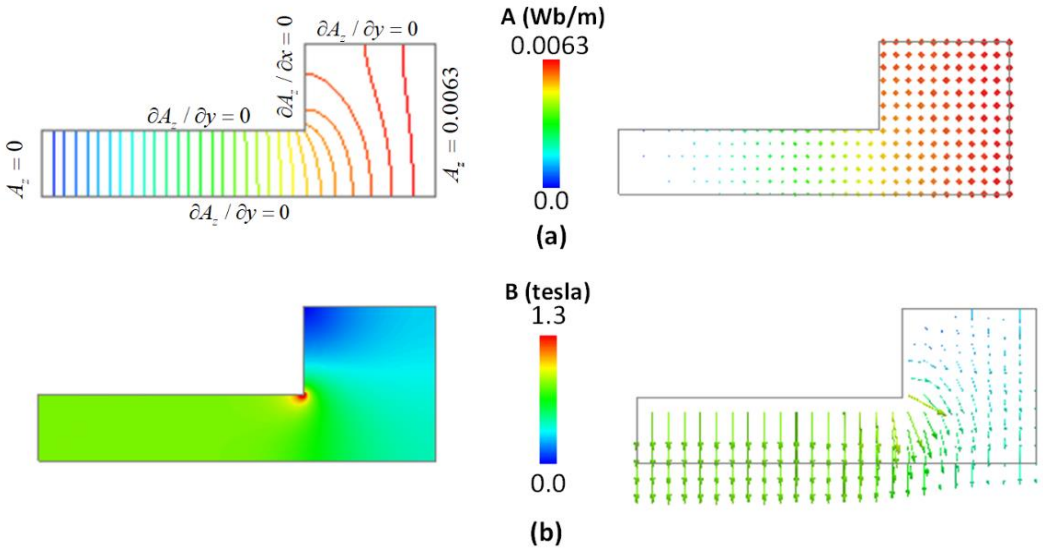

Figure 4.13: Field simulation in the selected region when the modulator height is small enough that a part of the flux takes the air path: (a) flux lines and magnetic vector potential and (b) magnetic flux density distribution and vectors.

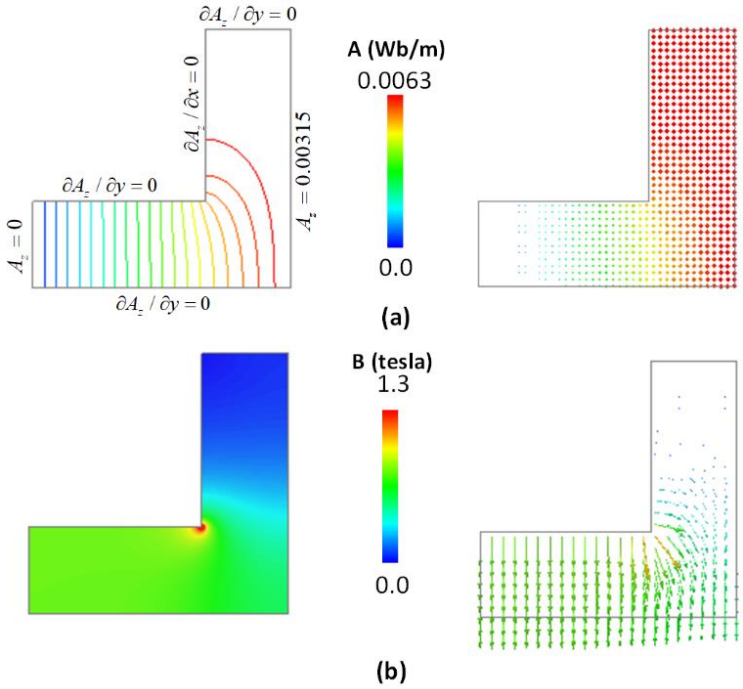

Figure 4.14: Field simulation in the selected region when the modulator height is large enough that all of the flux takes the modulator path: (a) flux lines and magnetic vector potential and (b) magnetic flux density distribution and vectors.

Based on the field observations, the two flux tube models depicted in Fig. 4.15 and Fig. 4.16 are offered for the two conditions mentioned.

Model A:

In *model A*, a part of the flux takes the air in the inter-modulator region as shown in Fig. 4.15. The yellow region is associated with the reluctance P_{max} which is biggest permeance per unit area as calculated below:

$$\wp_{\max} = \frac{\mu_0}{g_{ie} + g_o + h_m} \tag{4.29}$$

The middle permeance per unit area is related to the green region. What is the boundary point between the green and pink flux tubes? When should our model switch between these two tubes? The flux lines take the green region as long as length of the path they take in the air, given below, is shorter that the path they have to take in the inter-modulator region.

$$l(r) = g_{ie} + g_o + h_m + \pi r \tag{4.30}$$

where r is the radius of the quarter circles in the flux tube. The condition to be met is:

$$l(r) < g_{ie} + h_{\mathrm{mod}} + g_o + h_m \quad \Rightarrow \quad r < \frac{h_{\mathrm{mod}}}{\pi} \tag{4.31}$$

Therefore, the permeance areas associated with green and pink flux tubes are h_{mod}/π and w_{mod}-$2h_{mod}/\pi$. The permeance per unit area is:

$$\wp_{mid}(r) = \frac{\mu_0}{g_{ie} + g_o + h_m + \pi r} \tag{4.32}$$

To simplify calculations by stepwise approximation of curve, the permeance average permeance per unit area is

$$\wp_{mid} = \frac{1}{h_{\mathrm{mod}} / \pi} \times \int_0^{h_{\mathrm{mod}}/\pi} \frac{\mu_0 \, dr}{g_{ie} + g_o + h_m + \pi r} \tag{4.33}$$

We obtain:

$$\wp_{mid} = \frac{\mu_0}{h_{\mathrm{mod}}} \ln\left(1 + \frac{h_{\mathrm{mod}}}{g_{ie} + g_o + h_m}\right) \tag{4.34}$$

The smallest permeance per unit area is related to the pink flux tube as calculated below:

$$\wp_{\min} = \frac{\mu_0}{g_{ie} + h_{\mathrm{mod}} + g_o + h_m} \tag{4.35}$$

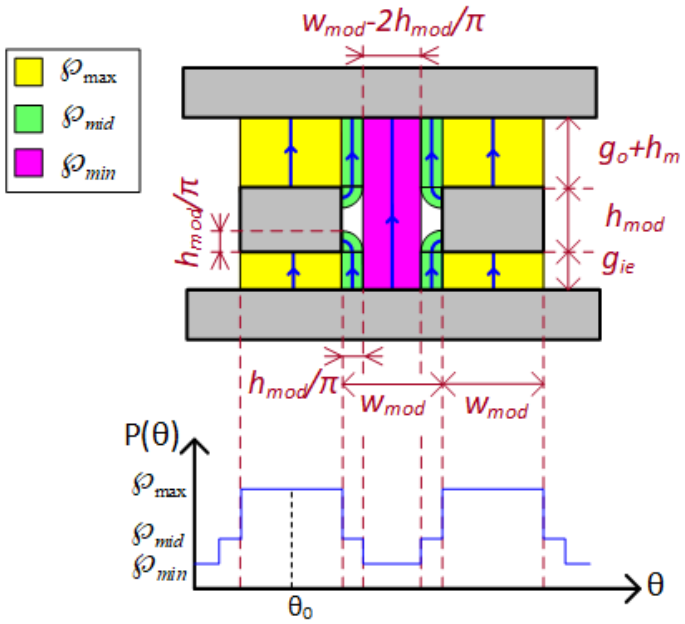

Figure 4.15: Flux tube model for hm <π wm/when the modulator height is small enough that a part of the flux takes the air path.

In this case, Fourier series representation of the reluctance spatial distribution is:

$$\wp(\theta) = a_0 + \sum_{n=1}^{+\infty} a_n \cos n\, p_{\mathrm{mod}}(\theta - \theta_0) \tag{4.36}$$

where

$$a_0 = \frac{2}{2\pi / p_{\mathrm{mod}}} \int_0^{\pi / p_{\mathrm{mod}}} \wp'(\theta)\, d\theta \tag{4.37}$$

$$a_n = \frac{4}{2\pi / p_{\mathrm{mod}}} \int_0^{\pi / p_{\mathrm{mod}}} \wp'(\theta) \cos(n\, p_{\mathrm{mod}} \theta)\; d\theta \tag{4.38}$$

After mathematical manipulation, we have:

$$a_0 = \frac{1}{2}\left(\wp_{\max} + \wp_{\min}\right) + \frac{p_{\mathrm{mod}} \Delta\theta}{\pi}\left(\wp_{mid} - \wp_{\min}\right) \tag{4.39}$$

$$a_n = \frac{2}{n\pi}\left(\wp_{\max} - \wp_{mid}\right)\sin(\frac{n\pi}{2}) + \frac{2}{n\pi}\left(\wp_{mid} - \wp_{\min}\right)\sin(\frac{n\pi}{2} + n\, p_{\mathrm{mod}} \Delta\theta) \tag{4.40}$$

where $\Delta\theta = h_{\mathrm{mod}} / \pi R_{av}$ is the angle related to area of P_{mid} calculated as in below:

For fundamental (n=1), we have:

$$\begin{aligned} \wp_0 = a_0 &= \frac{1}{2}\left(\wp_{\max} + \wp_{\min}\right) + \frac{p_{\mathrm{mod}} \Delta\theta}{\pi}\left(\wp_{mid} - \wp_{\min}\right) \\ \wp_1 = a_1 &= \frac{2}{\pi}\left(\wp_{\max} - \wp_{mid}\right) + \frac{2}{\pi}\left(\wp_{mid} - \wp_{\min}\right)\sin(\frac{\pi}{2} + p_{\mathrm{mod}} \Delta\theta) \end{aligned} \tag{4.41}$$

Then, we have $\wp(\theta, t) = \wp_0 + \wp_1 \cos\, p_{\mathrm{mod}}(\theta - \theta_0)$

Model B:

In model B, all of the flux takes the path of infinitely permeable modulators as shown in Fig. 4.16. What is the boundary to switch between the models of *model A* and *model B*? It is obvious that with an increase in modulator height h_{mod}, the pink flux tube vanishes after a critical point. This critical point is when the two green flux tubes in the inter-modulator region with total area of $2h_{mod}/\pi$ takeover the whole inter-modulator area w_{mod}, so the condition to switch to *model B* will be:

$$\frac{2h_{\mathrm{mod}}}{\pi} > w_{\mathrm{mod}} \quad \Rightarrow \quad h_{\mathrm{mod}} > \frac{\pi\, w_{\mathrm{mod}}}{2} \tag{4.42}$$

The yellow region which is associated with the reluctance P_{max} is the biggest permeance per unit area as calculated before:

$$\wp_{\max} = \frac{\mu_0}{g_{ie} + g_o + h_m} \tag{4.43}$$

The permeance per unit area which is related to the green region is calculated as in below:

$$\wp_{min} = \frac{1}{w_{\text{mod}} / 2} \times \int_0^{w_{\text{mod}}/2} \frac{\mu_0 \, dr}{g_{ie} + g_o + h_m + \pi r} \tag{4.44}$$

We obtain:

$$\wp_{min} = \frac{2\mu_0}{\pi \, w_{\text{mod}}} \ln\left(1 + \frac{\pi \, w_{\text{mod}}}{2(g_{ie} + g_o + h_m)}\right) \tag{4.45}$$

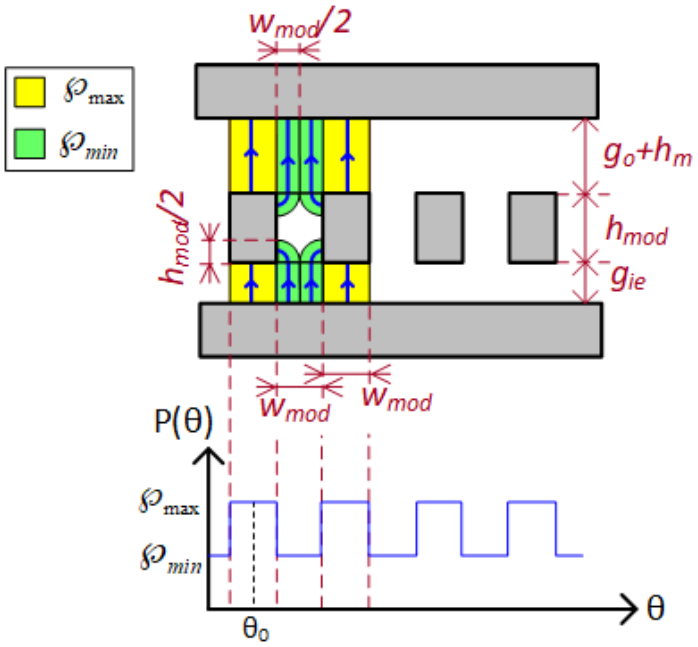

Figure 4. 16: Flux tube model for hm >π wm/2 when the modulator height is large enough that all of the flux takes the modulator path

In this case, Fourier series representation of the reluctance distribution is:

$$\wp(\theta) = \frac{1}{2}(\wp_{\max} + \wp_{\min}) + \sum_{n=1}^{+\infty} \frac{4}{n\pi} \sin\left(\frac{n\pi}{2}\right) \frac{1}{2}(\wp_{\max} - \wp_{\min}) \cos n \, p_{\text{mod}}(\theta - \theta_0) \tag{4.46}$$

where

$$\wp_0 = \frac{1}{2}(\wp_{\max} + \wp_{\min}) \tag{4.47}$$

$$\wp_1 = \frac{1}{2}\frac{4}{\pi}(\wp_{\max} - \wp_{\min}) \tag{4.48}$$

The space fundamental component is also as in the following:

$$\wp(\theta, t) = \wp_0 + \wp_1 \cos p_{\text{mod}}(\theta - \theta_0) \tag{4.49}$$

In the case of rotating modulators, we have:

$$\theta_0 = \omega_m t + \zeta \tag{4.50}$$

where ω_m is the mechanical speed of the rotor and ξ is the initial position at time $t=0$. In the case of stationary modulators and having the PMs as the rotating part, we have $\theta=0$ and then,

$$\wp(\theta) = \wp_0 + \wp_1 \cos p_{\text{mod}}\theta \tag{4.51}$$

4.5 Modeling of the stator

In this section, magneto motive force, equivalent surface current density and tangential magnetic field intensity of the stator are obtained.

4.5.1 MMF produced by stator

In this section we will obtain the magnetomotive force produced by the stator which will be used in calculation of the radial component of the magnetic field density in the air-gap. Fig. 4.17(a) shows a typical 2-pole ($P_s=1$) three-phase stator with concentrated windings. The positive direction of the pulsating fluxes produced by each phase is also depicted (negative currents produce a flux in the opposite direction). The resultant of these three pulsating fluxes is a rotating field in the air-gap.

Figs. 4.17(b)-(d) show the flux lines (closed path of Ampere's law) and the corresponding spatial distribution of the magnetomotive forces (pulsating fluxes) for the three phases at time $t=0$ where $i_a=I_s$, $i_b=-I_s/2$ and $i_c=-I_s/2$. The resultant magnetomotive

force, as shown in Fig. 4.17 (e), is a traveling wave for *t>0*. The amplitude of the MMF of each phase is obtained from Ampere's circuital law as in below:

$$\oint_C \vec{H}.d\vec{l} = I_{enc} \quad \Rightarrow \quad g\,H + g\,H = \frac{Ni_a}{p_s} \quad \Rightarrow \quad H = \frac{Ni_a}{2\,g\,p_s} \tag{4.52}$$

Also,

$$MMF = g\,H \quad \Rightarrow \quad MMF = \frac{Ni_a}{2\,p_s} \tag{4.53}$$

where N is the number of turns per phase and N/p_s is the number of turns per phase per pole, and phase currents are:

$$i_a(t) = I_s \cos(\omega t) \tag{4.54}$$

$$i_b(t) = I_s \cos(\omega t - \frac{2\pi}{3}) \tag{4.54}$$

$$i_c(t) = I_s \cos(\omega t + \frac{2\pi}{3}) \tag{4.56}$$

The Fourier series representation of the spatial distribution of the three magnetomotive forces are as in below:

$$F_a(\theta,t) = -\sum_{\substack{n=1 \\ odd}}^{+\infty} \frac{4}{n\pi} \frac{N\,i_a(t)}{2\,p_s} \sin\left(np_s\theta\right) \tag{4.57}$$

$$F_b(\theta,t) = -\sum_{\substack{n=1 \\ odd}}^{+\infty} \frac{4}{n\pi} \frac{N\,i_b(t)}{2\,p_s} \sin\left(np_s(\theta - \frac{2\pi}{3})\right) \tag{4.58}$$

$$F_c(\theta,t) = -\sum_{\substack{n=1 \\ odd}}^{+\infty} \frac{4}{n\pi} \frac{N\,i_c(t)}{2\,p_s} \sin\left(np_s(\theta + \frac{2\pi}{3})\right) \tag{4.59}$$

The Fourier representation series of the spatial distribution of the total magnetomotive forces can be obtained directly from the step-wise waveform in Fig. 4.17(e) directly or by mathematical calculations as in below:

$$F_s(\theta,t) = F_a(\theta,t) + F_b(\theta,t) + F_c(\theta,t) \tag{4.60}$$

By substitution of the magnetomotive forces and the currents, we have:

$$\begin{aligned} F_s(\theta,t) = &-\sum_{\substack{n=1\\odd}}^{+\infty} \frac{4}{n\pi}\frac{N I_s}{2 p_s}\cos(\omega t)\sin\left(np_s\theta\right) \\ &-\sum_{\substack{n=1\\odd}}^{+\infty} \frac{4}{n\pi}\frac{N I_s}{2 p_s}\cos(\omega t-\frac{2\pi}{3})\sin\left(np_s(\theta-\frac{2\pi}{3})\right) \\ &-\sum_{\substack{n=1\\odd}}^{+\infty} \frac{4}{n\pi}\frac{N I_s}{2 p_s}\cos(\omega t+\frac{2\pi}{3})\sin\left(np_s(\theta+\frac{2\pi}{3})\right) \end{aligned} \tag{4.61}$$

We have,

$$\begin{aligned} F_s(\theta,t) = -\frac{4}{n\pi}\frac{N I_s}{2 p_s}\sum_{\substack{n=1\\odd}}^{+\infty}\Big\{&\sin\left(np_s\theta-\omega t\right)+\sin\left(np_s\theta+\omega t\right) \\ &+\sin\left(np_s\theta-\omega t-(n-1)\frac{2\pi}{3})\right)+\sin\left(np_s\theta+\omega t-(n+1)\frac{2\pi}{3})\right) \\ &+\sin\left(np_s\theta-\omega t+(n-1)\frac{2\pi}{3})\right)+\sin\left(np_s\theta+\omega t+(n+1)\frac{2\pi}{3})\right)\Big\} \end{aligned} \tag{4.62}$$

For *n=1, 7, 13, etc.,* we have the first part of each pair in the three lines of the equation above, resulting in a forward traveling wave in the air-gap. The n^{th} component is as in below:

$$F_{sn}(\theta,t) = -\frac{3}{2}\frac{4}{n\pi}\frac{NI_s}{2 p_s}\sin\left(np_s\theta-\omega t\right) \tag{4.63}$$

while for *n=5, 11, etc.,* we have the first part of each pair in the three lines of the equation above, resulting in a backward traveling wave in the air-gap. The n^{th} component is as in the following:

$$F_{sn}(\theta,t) = -\frac{3}{2}\frac{4}{n\pi}\frac{NI_s}{2 p_s}\sin\left(np_s\theta+\omega t\right) \tag{4.64}$$

Therefore, the fundamental component (*n=1*) is:

$$F_s(\theta,t) = -\frac{3}{2}\frac{4}{\pi}\frac{NI_s}{2p_s}\sin\left(p_s\theta - \omega t\right) \tag{4.65}$$

In the reality, usually we will not employ full-pitched concentrated windings, so to account for the winding configuration, the winding factor k_w can be included into the above relationship as in below:

$$F_s(\theta,t) = F_{s1}\sin\left(p_s\theta - \omega t - \delta\right) \tag{4.66}$$

$$F_{s1} = -\frac{3}{2}\frac{4}{\pi}\frac{NI_s}{2p_s}k_w \tag{4.67}$$

where δ is the current angle and the winding factor is defined as in below:

$$k_w = k_p\, k_d \tag{4.68}$$

where k_p and k_b are pitch and distribution factors, respectively. In a short-pitched winding, the pitch factor for the n^{th} harmonic is as in below:

$$k_{pn} = \sin\frac{n\alpha}{2} \tag{4.69}$$

where α refers to the angular displacement between the two sides of a coil in electrical degrees. For a full-pitched coil $\alpha=\pi$.

In a distributed winding, the distribution factor for the n^{th} harmonic is given below:

$$k_{dn} = \frac{\sin\frac{nm\gamma}{2}}{m\sin\frac{n\gamma}{2}} \tag{4.70}$$

where γ is the slot angular pitch in electrical degrees and m is the number of slots per pole per phase. For a concentrated winding $m=1$ and so $k_d=1$.

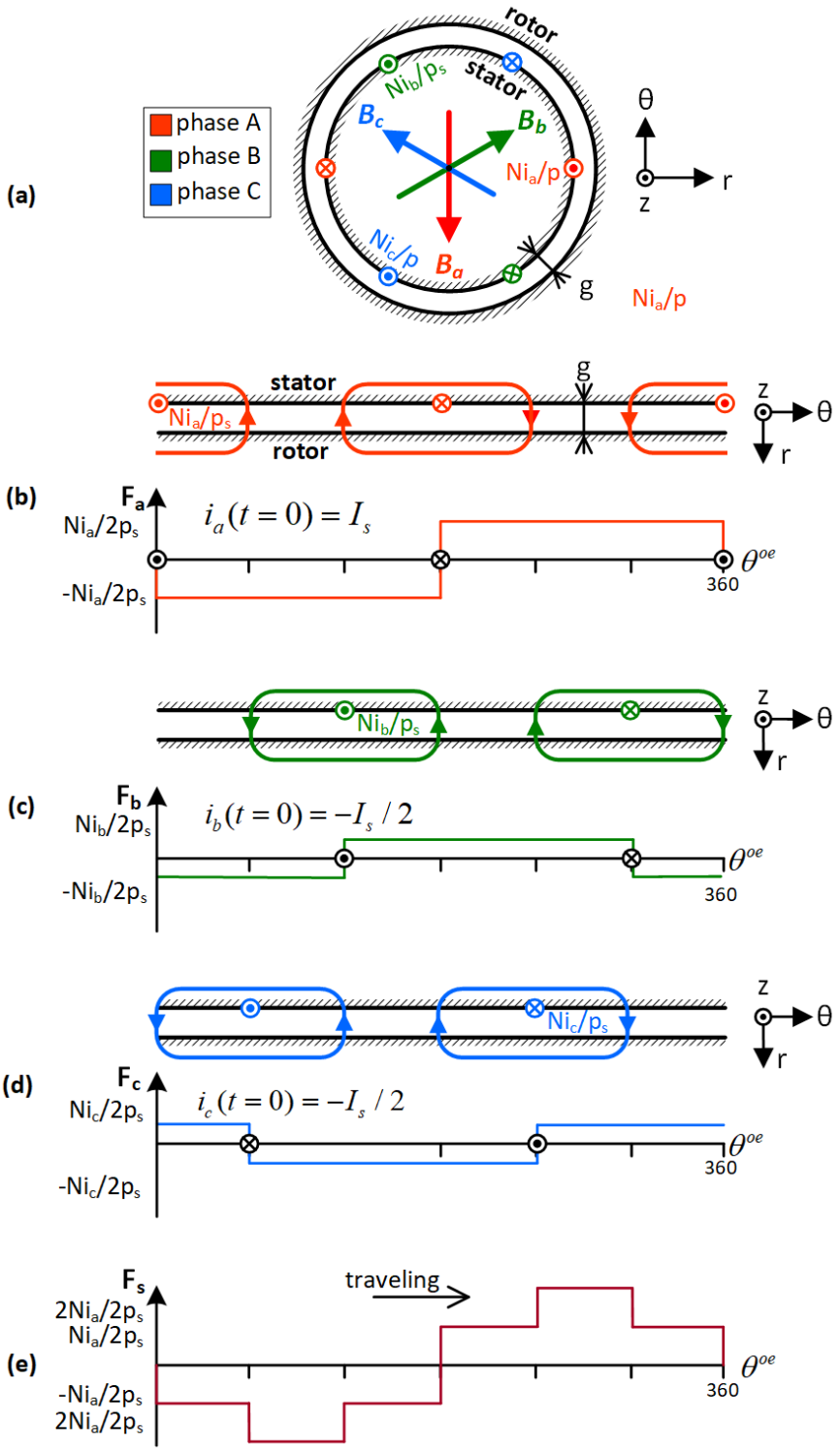

Figure 4.17: A typical three-phase two-pole stator with concentrated windings: (a) stator phases and field axis of each phase, (b) flux lines and MMF produced by phase a, (c) flux lines and MMF produced by phase b, (d) flux lines and MMF produced by phase c, and (e) the resultant traveling MMF in the air-gap

4.5.2 Equivalent surface current density of stator

In this section, we obtain the equivalent surface current density of the stator that plays the role of the stator winding embedded the slots in the slotless winding after employing the carter's coefficient. It will be used in torque calculations on the stator as well as in extracting the tangential component of the magnetic field intensity on the surface of the stator. Using the Ampere's circuital law for the closed curve *C* in Fig. 4.18, we have:

$$\oint_C \vec{H}.d\vec{l} = K_z R_i \Delta\theta \tag{4.71}$$

Magnetic field intensity is zero in infinitely permeable irons, so it leads to:

$$g H_r\big|_{\theta-\Delta\theta/2} - g H_r\big|_{\theta+\Delta\theta/2} = K_z R_i \Delta\theta \Rightarrow K_z = -\frac{g}{R_i}\frac{H_r\big|_{\theta+\Delta\theta/2} - H_r\big|_{\theta-\Delta\theta/2}}{\Delta\theta} \tag{4.72}$$

The limit of the difference quotient above as $\Delta\theta$ approaches to zero leads to the derivative of H_r with respect to θ as in below:

$$K_z = \lim_{\Delta\theta\to 0} -\frac{g}{R_i}\frac{H_r\big|_{\theta+\Delta\theta/2} - H_r\big|_{\theta-\Delta\theta/2}}{\Delta\theta} = -\frac{g}{R_i}\frac{\partial H_r}{\partial\theta} \tag{4.73}$$

On the other hand, we know that

$$F_s = g H_r \tag{4.74}$$

Combining the two leads to:

$$K_z(\theta,t) = \frac{-1}{R_i}\frac{\partial F_s}{\partial\theta} \tag{4.75}$$

By substitution of F_s, we obtain the fundamental component as in below

$$K_z(\theta,t) = \frac{3}{2}\frac{4}{\pi}\frac{NI_s}{2R_i}k_w \cos\left(p_s\theta - \omega t - \delta\right) \tag{4.76}$$

It can be written as in below:

$$K_z(\theta,t) = K_{z1}\cos\left(p_s\theta - \omega t - \delta\right) \tag{4.77}$$

$$K_{z1} = \frac{3}{2}\frac{4}{\pi}\frac{NI_s}{2R_i}k_w \tag{4.78}$$

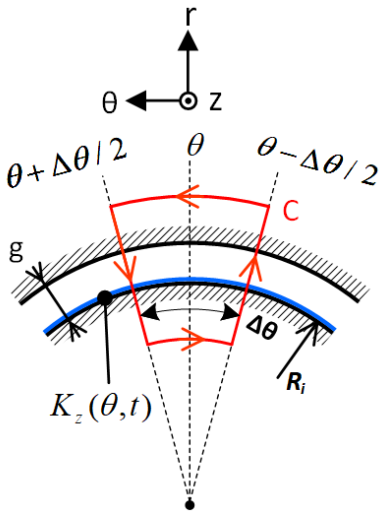

Figure 4.18: Closed line of the Ampere's law enclosing the surface current density of the stator.

4.5.3 Tangential component of magnetic field intensity on surface of stator

Tangential component of the magnetic field intensity on the surface of the stator will be used in determining the shear stress on the stator surface using Maxwell stress tensor. Using Ampere's law over the contour *C* shown in Fig. 4.19, and knowing that magnetic intensity within infinitely permeable iron of stator is zero, we have:

$$H_\theta - 0 = K_z \;\Rightarrow\; H_\theta = K_z \tag{4.79}$$

By substituting K_z, we obtain the fundamental component as in below:

$$H_\theta(\theta,t) = H_{\theta 1}\cos\left(p_s\theta - \omega t - \delta\right) \tag{4.80}$$

$$H_{\theta 1} = \frac{3}{2}\frac{4}{\pi}\frac{NI_s}{2R_i}k_w \tag{4.81}$$

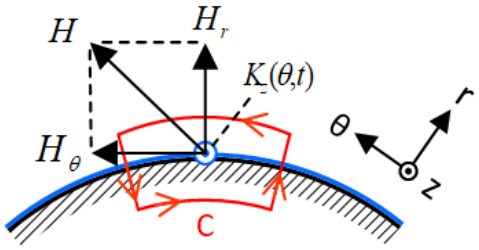

Figure 4.19: Closed line of the Ampere's law around the boundary of stator surface

4.6 Permanent magnet modeling

This part is devoted to calculation of the magnetomotive force, equivalent magnetic charge and equivalent Amperian current of the PMs.

4.6.1 MMF force produced by PMs

The magnetomotive force produced by permanent magnets, which will be used in calculation of the radial component of the magnetic flux density distribution, can be written as in below:

$$F_m(\theta) = h_m M(\theta) \tag{4.82}$$

where h_m is the PM height and the magnetization density of permanent magnets $\boldsymbol{M}$, shown in Fig. 4.20(a), is related to PM's residual flux density B_r as in below:

$$M = \frac{1}{\mu_0} B_r \tag{4.83}$$

We also know that

$$\vec{H} = \mu_0(\vec{B} + \vec{M}) \tag{4.84}$$

The permanents magnets are alternating in the polarity and have an arc angle of θ_m, so Fourier series representation of the demagnetization density distribution can be written as in below:

$$M(\theta) = \sum_{\substack{n=1 \\ odd}}^{+\infty} \frac{B_r}{\mu_0} \frac{4}{n\pi} \sin \frac{n\, p_m \theta_m}{2} \cos n\, p_m (\theta - \theta_0) \tag{4.85}$$

Then, the fundamental component leads to a continuous magnetization sheet as shown in Fig. 4.21(a). It can be represented as in the following:

$$M(\theta, t) = M_0 \cos p_m (\theta - \theta_0) \tag{4.86}$$

where

$$M_0 = \frac{4}{\pi} \frac{B_r}{\mu_0} \sin \frac{p_m \theta_m}{2} \tag{4.87}$$

In the case of rotating magnets, we have:

$$\theta_0 = \omega_m t + \zeta \tag{4.88}$$

where ω_m is the mechanical speed of the rotor and ξ is the initial position at time $t=0$. When the modulators are the rotating part and PMs are stationary, we have $\theta_0=0$ and then,

$$M(\theta) = M_0 \cos p_m \theta \tag{4.89}$$

4.6.2 Coulombian magnetic charge model of PMs

Using the so-called Coulombian model, the permanent magnets can be represented by fictitious magnetic charges that can be used in torque calculation by employing Kelvin magnetization force density [42] and [43]. The magnetization density $\boldsymbol{M}$ results in the fictitious charge density ρ_m as in below:

$$\rho_m = -\nabla . \mu_0 \vec{M} \tag{4.90}$$

In radially magnetized permanent magnets, we have:

$$\rho_m = -\mu_0 \frac{\partial M_r}{r} \tag{4.91}$$

In a permanent magnet having a uniform magnetization, the divergence of $\boldsymbol{M}$ is zero throughout the volume. In this case, a magnetic surface charge density is defined as in the following:

$$\sigma_m = -\hat{n}.\mu_0(M^a - M^b) \tag{4.92}$$

where $\boldsymbol{n}$ is the unit normal vector of the surface boundary. It is worth noting that positive and negative magnetic surface charge densities should be assigned to the surface boundaries of a permanent magnet such that *M* vectors originate from negative charges and terminates on positive charges—the rule. As shown in Fig. 4.20(b), the surfaces magnetic charges on the two sides on PMs, whose normal vector are in the radial direction, are obtained as in below:

$$\sigma_m = \pm\mu_0 M \tag{4.93}$$

The fundamental component as shown in Fig. 4.21(b), obtained from the fundamental component of the surface charge density distribution shown in Fig. 4.21(a), is obtained as:

$$\sigma_m(\theta, t) = -\mu_0 M_0 \cos p_m(\theta - \theta_0) \tag{4.94}$$

When the modulators are the rotating part and PMs are stationary, we have $\theta_0=0$ and then,

$$\sigma_m(\theta) = -\mu_0 M_0 \cos p_m\theta \tag{4.95}$$

4.6.3 Amperian current model of PMs

Magnetization of permanent magnets can be modeled by an equivalent current density called Amperian currents [42]–[43] which can be used in torque calculations by employing Lorentz force. The equivalent current density of magnetization $\boldsymbol{M}$ can be extracted as in below:

$$\vec{J}_m = \nabla \times \vec{M} \tag{4.96}$$

For radially magnetized PMs, the equivalent current is in the z-direction is obtained as in the following:

$$J_m = -\frac{1}{r}\frac{\partial M}{\partial \theta} \tag{4.97}$$

In a permanent magnet having a uniform magnetization, the curl of $\boldsymbol{M}$ is zero throughout the volume. In this case, a surface current density is defined as in the following:

$$\vec{K}_m = \vec{M} \times \hat{n} \tag{4.98}$$

where $\boldsymbol{n}$ is the unit normal vector of the surface boundary. It is worth noting that positive (in +z direction) and negative (in -z direction) surface current densities should be assigned to the surface boundaries of a permanent magnet such that they produce a flux in the same direction as *M*—right hand rule in Ampere's law. As shown in Fig. 4.20(c), the surfaces current densities on the two sides of PMs, whose normal vector are in the θ direction, are obtained as in below:

$$K_m = \pm M \tag{4.99}$$

This is singularity at the side surfaces of a radially-magnetized PM. The radius *r* in the curl representation of Amperian currents can be seen by looking at the nature of an impulse. If θ_0 is the left side position of the right PM, on which there is a singularity, according to the definition of an impulse, we have:

$$\int_{\theta_{0-}}^{\theta_{0+}} J_m(\theta)\, dl = M \Rightarrow \int_{\theta_{0-}}^{\theta_{0+}} J_m(\theta)\, r\, d\theta = M \Rightarrow \int_{\theta_{0-}}^{\theta_{0+}} J_m(\theta)\, d\theta = \frac{M}{r} \tag{4.100}$$

The fundamental component as shown in Fig. 4.21(c), obtained from the fundamental component of the magnetization density distribution shown in Fig. 4.21(a), is obtained as:

$$J_m(r,\theta,t) = -\frac{1}{r}\frac{\partial M}{\partial \theta} = \frac{M_0 p_m}{r}\sin p_m(\theta - \theta_0) \tag{4.101}$$

When the modulators are the rotating part and PMs are stationary, we have $\theta_0=0$ and then,

$$J_m(r,\theta)=\frac{M_0 p_m}{r}\sin p_m\theta \tag{4.102}$$

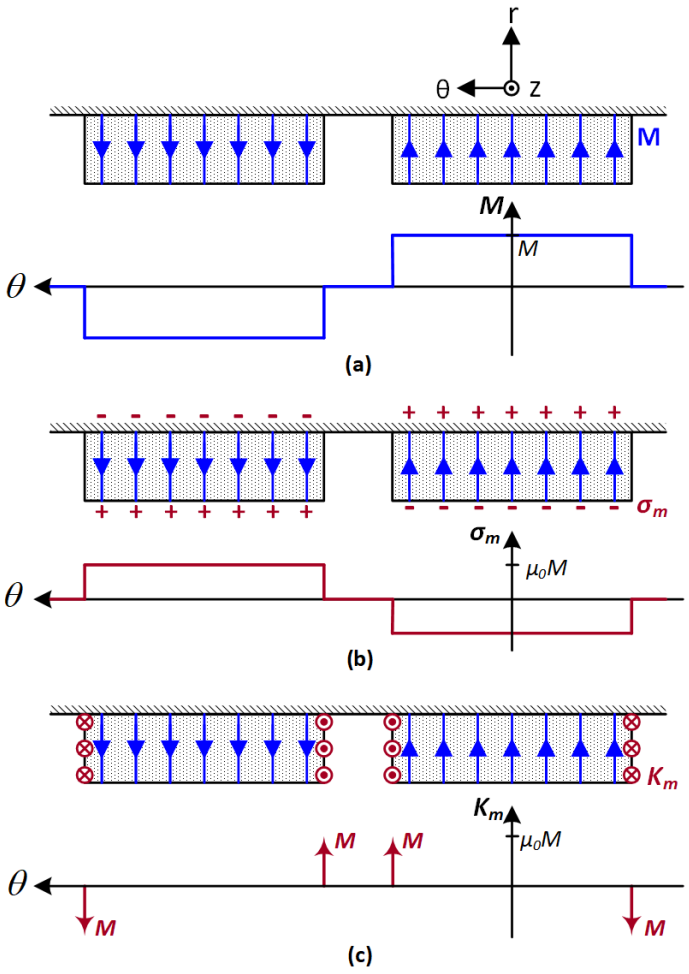

Figure 4.20: Permanent magnet modeling: (a) magnetization, (b) equivalent fictitious charge and (c) equivalent surface current density

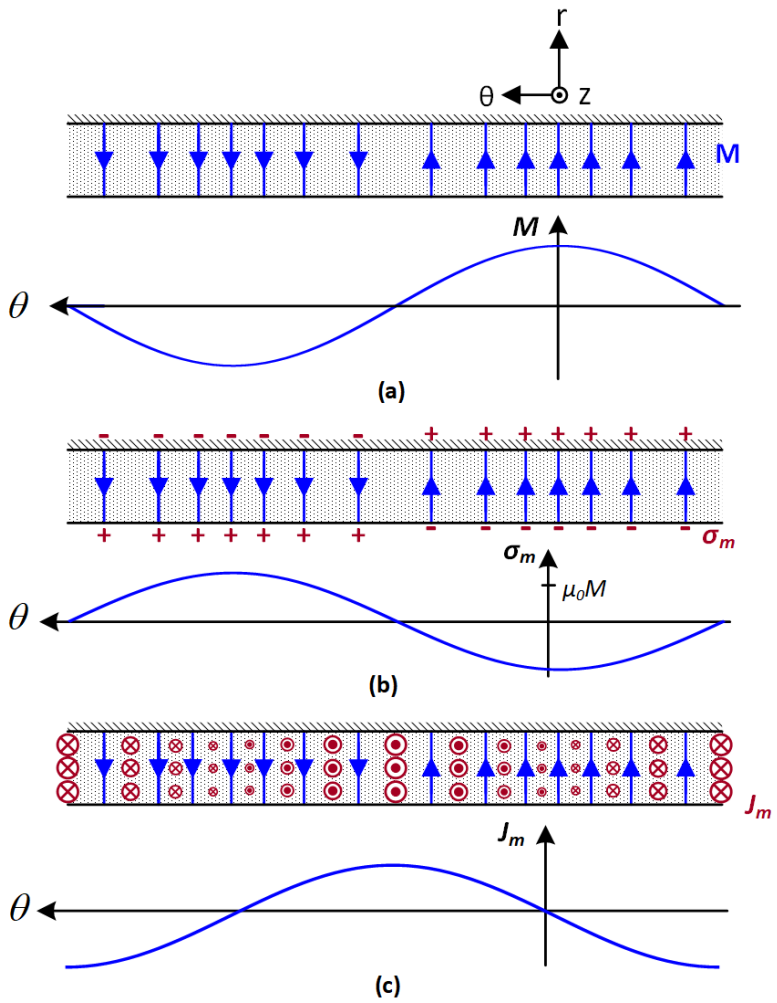

Figure 4.21: Permanent magnet modeling using the fundamental component: (a) magnetization, (b) equivalent fictitious charge and (c) equivalent surface current density

4.6.4 Tangential component of the magnetic field intensity on the surface of PMs

Tangential component of the magnetic field intensity on the surface of the PMs will be used in determining the shear stress on the surface of PMs using Kelvin force density. The tangential component of the field H_θ can be approximated based on the radial component of the field H_r. The filed is perpendicular to the surface of the infinitely permeable iron, so

$$H_\theta\big|_{r=R_o+h_m} = 0 \tag{4.103}$$

As shown in Fig. 4.22, using a linear approximation of H_θ in the PM region, H_θ can be represented as a linear function of r with the rate of $\partial H_\theta/\partial\theta$.

$$H_\theta\big|_{r=R_o} - H_\theta\big|_{r=R_o+h_m} = \frac{\partial H_\theta}{\partial r}[R_o - (R_o + h_m)] \tag{4.104}$$

It leads to:

$$H_\theta\big|_{r=R_o} = -h_m \frac{\partial H_\theta}{\partial r} \tag{4.105}$$

Ampere's law in a current-free region says that:

$$\nabla \times H = 0 \;\Rightarrow\; (0-0)a_r + (0-0)a_\theta + (\frac{\partial H_\theta}{\partial r} - \frac{1}{r}\frac{\partial H_r}{\partial \theta})a_z = 0 \tag{4.106}$$

so,

$$\frac{\partial H_\theta}{\partial r} = \frac{1}{r}\frac{\partial H_r}{\partial \theta} \tag{4.107}$$

Substituting (4.107) into (4.105), we obtain H_θ as a function of H_r on the surface of the PM ($r=R_o$):

$$H_\theta\big|_{r=R_o} = -\frac{h_m}{R_o}\frac{\partial H_r}{\partial \theta} \tag{4.108}$$

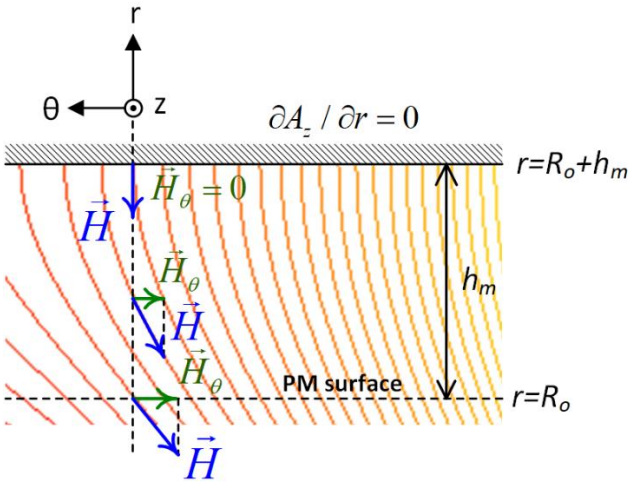

Figure 4.22: Linear approximation of the flux lines at the surface of PMs

4.7 Radial component of the magnetic flux density distribution

In this section, radial component of the magnetic flux density distribution will be calculated for the cases of rotating modulators and rotating PMs.

4.7.1 Modulators as the rotor

In the case of rotating modulators, radial component of the magnetic flux density can be obtained from the following equation:

$$B_r(\theta,t) = \{F_s(\theta,t) + F_m(\theta)\}\,\wp(\theta,t) \tag{4.109}$$

where

$$F_s(\theta,t) = F_{s1}\sin\left(p_s\theta - \omega t - \delta\right) \tag{4.110}$$

$$F_m(\theta) = h_m M_0 \cos p_m\theta \tag{4.111}$$

$$\wp(\theta,t) = \wp_0 + \wp_1\cos[p_{\text{mod}}\theta - p_{\text{mod}}(\omega_m t + \zeta)] \tag{4.112}$$

Substitution of the three above equations leads to:

$$\begin{aligned} B_r(\theta,t) = \{&F_{s1}\sin\left(p_s\theta - \omega t - \delta\right) + h_m M_0\cos p_m\theta\}\times \\ &\{\wp_0 + \wp_1\cos[p_{\text{mod}}\theta - p_{\text{mod}}(\omega_m t + \zeta)]\} \end{aligned} \tag{4.113}$$

We have:

$$\begin{aligned} B_r(\theta,t) = {}& F_{s1}\wp_0\sin\left(p_s\theta - \omega t - \delta\right) \\ &+ F_{s1}\wp_1\sin\left(p_s\theta - \omega t - \delta\right)\cos[p_{\text{mod}}\theta - p_{\text{mod}}(\omega_m t + \zeta)] \\ &+ h_m M_0\wp_0\cos p_m\theta \\ &+ h_m M_0\wp_1\cos p_m\theta\cos[p_{\text{mod}}\theta - p_{\text{mod}}(\omega_m t + \zeta)] \end{aligned} \tag{4.114}$$

Using

$$\sin\alpha\cos\beta = \frac{1}{2}\sin(\alpha-\beta) + \frac{1}{2}\sin(\alpha+\beta) \tag{4.115}$$

$$\cos\alpha\cos\beta = \frac{1}{2}\cos(\alpha-\beta) + \frac{1}{2}\cos(\alpha+\beta) \tag{4.116}$$

we end up in the six terms below:

$$
\begin{aligned}
B_r(\theta,t) = {} & F_{s1}\wp_0 \sin\left(p_s\theta - \omega t - \delta\right) \\
& + \frac{1}{2}F_{s1}\wp_1 \sin\left[(p_s - p_{\mathrm{mod}})\theta - (\omega - p_{\mathrm{mod}}\omega_m)t - \delta + p_{\mathrm{mod}}\zeta\right] \\
& + \frac{1}{2}F_{s1}\wp_1 \sin\left[(p_s + p_{\mathrm{mod}})\theta - (\omega + p_{\mathrm{mod}}\omega_m)t - \delta - p_{\mathrm{mod}}\zeta\right] \\
& + h_m M_0 \wp_0 \cos p_m\theta \\
& + \frac{1}{2}h_m M_0 \wp_1 \cos\left[(p_m - p_{\mathrm{mod}})\theta + p_{\mathrm{mod}}\omega_m t + p_{\mathrm{mod}}\zeta\right] \\
& + \frac{1}{2}h_m M_0 \wp_1 \cos\left[(p_m + p_{\mathrm{mod}})\theta - p_{\mathrm{mod}}\omega_m t - p_{\mathrm{mod}}\zeta\right]
\end{aligned}
\tag{4.117}
$$

Knowing that the periodic traveling wave $A\ sin(p\theta-\omega t)$ has p poles and rotation speed of ω/p, the whole idea of modulation can be seen in the above formula as shown in Fig. 4.23.

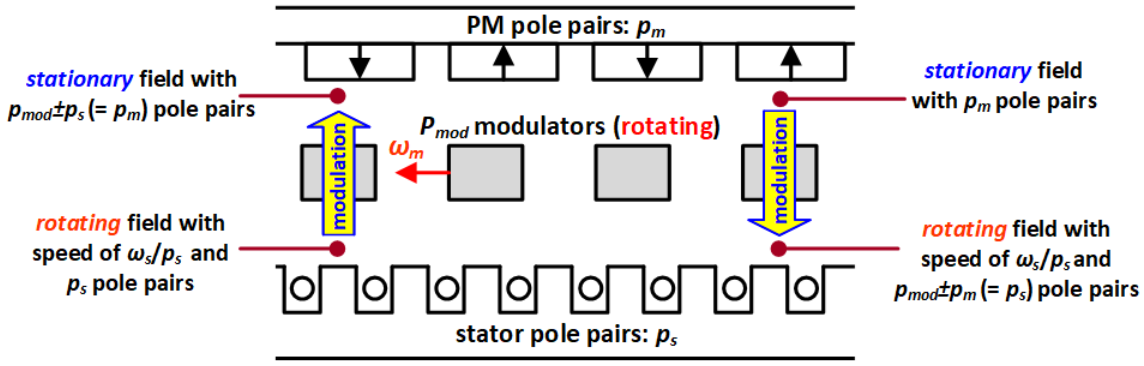

Figure 4.23: Modulation of the rotating field produced by stator and stationary PMs to the other side of the air-gap through rotating modulators

We will show in the future that:

- The first three terms are the magnetic fields produced by MMF of the stator having p_s pole pairs, so we have three fields having the following pole pairs as shown in Fig. 4.24:

  - p_s pole pairs out of interaction with the DC component
  - $p_{mod}+p_s$ and p_{mod} - p_s pole pairs out of interaction with the fundamental harmonic of the permeance

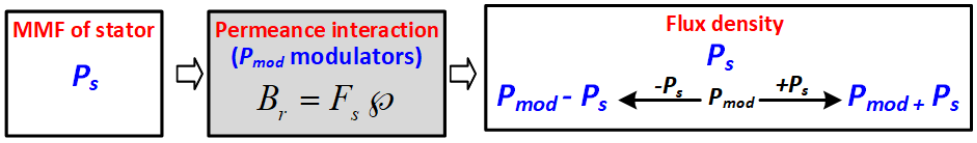

Figure 4.24: The pole pair of fields produced by the interaction of stator MMF having ps pole with pmod modulators

- In the finite element analysis, we will show that the magnitude of the harmonic $p_{mod} - p_s$ is actually higher than that the magnitude of the harmonic $p_{mod} + p_s$ which might be a result of leakage fluxes of interaction of other harmonics of the air-gap and magneto motives forces of stator and PMs.

- The last three terms are the magnetic fields produced by MMF of the PMs having p_m pole pairs, so we have three fields having the following pole pairs as shown in Fig. 4.25:

  - p_m pole pairs out of interaction with the DC component
  - $p_{mod}+p_m$ and $p_{mod} - p_m$ pole pairs out of interaction with the fundamental harmonic of the permeance

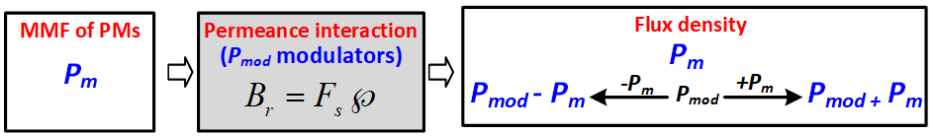

Figure 4.25: The pole pair of fields produced by the interaction MMF of PMs having pm pole with p_{mod} modulators

- The first term is the rotating field produced by the stator (having electrical frequency ω) in the stator air-gap which has p_s pole pairs and rotation speed of ω/p_s. The forth term is the stationary field produced by PMs in the PM air-gap which has p_m pole pairs. These two terms do not contribute in energy conversion and average torque production.

- The second and the third terms are actually **stationary magnetic fields in the PM air-gap** (having p_m pole pairs) that are modulated form of the **rotating magnetic field of the stator in the stator air-gap** (having p_s pole pairs and rotation speed of ω/p_s) using **rotating modulators** and are able to contribute in energy conversion in the PM air-gap and produce a torque by interaction with the field produced by the PMs in the certain conditions below:

1. Matching the pole pair of one of these stationary fields ($p_s \pm p_{mod}$) with the number of PM poles ($\pm p_m$) so that they can be locked at a specific torque angle.
2. Rotor mechanical speed of $\omega_m = \pm \omega / p_{mod}$.

Then, they can simply be represented as in below:

$$\frac{1}{2} F_{s1} \wp_1 \sin\left\{\pm p_{\mathrm{m}} \theta - \delta + p_{\mathrm{mod}} \zeta\right\} \tag{4.118}$$

$$\frac{1}{2} F_{s1} \wp_1 \sin\left\{\pm p_m \theta - \delta - p_{\mathrm{mod}} \zeta\right\} \tag{4.119}$$

- The fifth and the sixth terms are actually **rotating magnetic fields in the stator air-gap** (having p_s pole pairs and rotation speed of ω/p_s) that are modulated form of the **stationary magnetic field of PMs in the PM air-gap** (having p_m pole pairs) using **rotating modulators** and are able to contribute in energy conversion in the stator air-gap and produce a torque by interaction with the field produced by the stator in the certain conditions below:
  1. Matching the pole pair of one of these rotating fields ($p_m \pm p_{mod}$) with the number of PM poles ($\pm p_s$) so that they can be locked at a specific torque angle.
  2. Rotor mechanical speed of $\omega_m = \pm \omega / p_{mod}$.

  Then, they can simply be represented as in below:

$$\frac{1}{2} h_m M_0 \wp_1 \cos\left\{\pm p_s \theta \pm \omega_s t + p_{\mathrm{mod}} \zeta\right\} \tag{4.120}$$

$$\frac{1}{2} h_m M_0 \wp_1 \cos\left\{\pm p_s \theta \pm \omega_s t + p_{\mathrm{mod}} \zeta\right\} \tag{4.121}$$

4.7.2 Permanent magnets as the rotor

In the case of rotating PMs, radial component of the magnetic flux density can be obtained from the following equation:

$$B_r(\theta, t) = \left\{F_s(\theta, t) + F_m(\theta, t)\right\} \wp(\theta) \tag{4.122}$$

where

$$F_s(\theta,t) = F_{s1}\sin\left(p_s\theta - \omega t - \delta\right) \tag{4.123}$$

$$F_m(\theta,t) = h_m M_0 \cos[p_m\theta - p_{\mathrm{m}}(\omega_m t + \zeta)] \tag{4.124}$$

$$\wp(\theta) = \wp_0 + \wp_1 \cos p_{\mathrm{mod}}\theta \tag{4.125}$$

Substitution of the three above equations leads to:

$$\begin{aligned} B_r(\theta,t) = \left\{F_{s1}\sin\left(p_s\theta - \omega t - \delta\right) + h_m M_0 \cos[p_m\theta - p_{\mathrm{m}}(\omega_m t + \zeta)]\right\} \times \\ \left\{\wp_0 + \wp_1 \cos p_{\mathrm{mod}}\theta\right\} \end{aligned} \tag{4.126}$$

We have:

$$\begin{aligned} B_r(\theta,t) = {} & F_{s1}\wp_0 \sin\left(p_s\theta - \omega t - \delta\right) \\ & + F_{s1}\wp_1 \sin\left(p_s\theta - \omega t - \delta\right) \cos p_{\mathrm{mod}}\theta \\ & + h_m M_0 \wp_0 \cos[p_m\theta - p_{\mathrm{m}}(\omega_m t + \zeta)] \\ & + h_m M_0 \wp_1 \cos[p_m\theta - p_{\mathrm{m}}(\omega_m t + \zeta)] \cos p_{\mathrm{mod}}\theta] \end{aligned} \tag{4.127}$$

Like the previous section, it can be rewritten as in below:

$$\begin{aligned} B_r(\theta,t) = {} & F_{s1}\wp_0 \sin\left(p_s\theta - \omega t - \delta\right) \\ & + \frac{1}{2}F_{s1}\wp_1 \sin\left[(p_s - p_{\mathrm{mod}})\theta - \omega t - \delta\right] \\ & + \frac{1}{2}F_{s1}\wp_1 \sin\left[(p_s + p_{\mathrm{mod}})\theta - \omega t - \delta\right] \\ & + h_m M_0 \wp_0 \cos(p_m\theta - p_{\mathrm{m}}\omega_m t - p_{\mathrm{m}}\zeta) \\ & + \frac{1}{2}h_m M_0 \wp_1 \cos\left[(p_m - p_{\mathrm{mod}})\theta - p_{\mathrm{m}}\omega_m t - p_{\mathrm{m}}\zeta\right] \\ & + \frac{1}{2}h_m M_0 \wp_1 \cos\left[(p_m + p_{\mathrm{mod}})\theta - p_{\mathrm{m}}\omega_m t - p_{\mathrm{m}}\zeta\right] \end{aligned} \tag{4.128}$$

Similar to the previous section, the whole idea of modulation can be seen in the above formula as shown in Fig. 4.26.

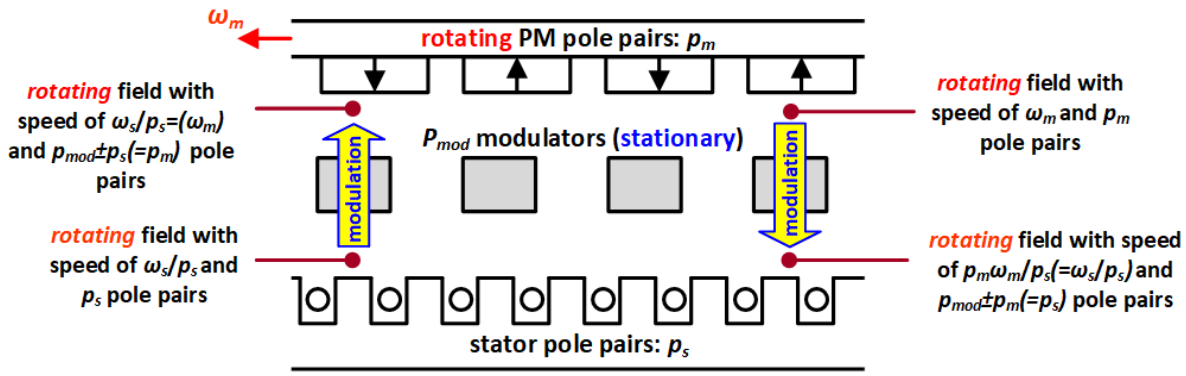

Figure 4. 26: Figure 4.26: Modulation of the rotating field produced by stator and rotating PMs to the other side of the air-gap through stationary modulators

We will show in the future that:

- The first three terms are the magnetic fields produced by MMF of the stator having p_s pole pairs, so we have three fields having the following pole pairs:
  - p_s pole pairs out of interaction with the DC component
  - $p_{mod}+p_s$ and p_{mod} - p_s pole pairs out of interaction with the fundamental harmonic of the permeance
- The last three terms are the magnetic fields produced by MMF of the PMs having p_m pole pairs, so we have three fields having the following pole pairs:
  - p_m pole pairs out of interaction with the DC component
  - $p_{mod}+p_m$ and p_{mod} - p_m pole pairs out of interaction with the fundamental harmonic of the permeance
- The first term is the rotating field produced by the stator (having electrical frequency ω) in the stator air-gap which has p_s pole pairs and rotation speed of ω/p_s. The forth term is the rotating field produced by PMs in the PM air-gap which has p_m pole pairs and rotation speed of ω_m. These two terms do not contribute in energy conversion and average torque production.
- The second and the third terms are actually **rotating magnetic fields in the PM air-gap** (having p_m pole pairs and rotation speed of ω_m) that are modulated form

of **rotating magnetic fields of stator in the stator air-gap** (having p_s pole pairs and rotation speed of ω/p_s) using **stationary modulators** and are able to contribute in energy conversion in the PM air-gap and produce a torque by interaction with the field produced by the PMs in the certain conditions below:

1. Matching the pole pair of one of these rotating fields ($p_s \pm p_{mod}$) with the number of PM poles ($\pm p_m$) so that they can be locked at a specific torque angle.
2. Rotor mechanical speed of $\omega_m = \pm\omega/p_{mod}$.

Then, they can simply be represented as in below:

$$\frac{1}{2} F_{s1} \wp_1 \sin\{(p_s - p_{\text{mod}})\theta - \omega t - \delta\} \tag{4.129}$$

$$\frac{1}{2} F_{s1} \wp_1 \sin\{(p_s + p_{\text{mod}})\theta - \omega t - \delta\} \tag{4.130}$$

- The fifth and the sixth terms are actually the **rotating magnetic field in the stator air-gap** (having p_s pole pairs and rotation speed of ω/p_s) that are modulated form of the **rotating magnetic field of PMs in the PM air-gap** (having p_m pole pairs and rotation speed of ω_m) using **stationary modulators** and are able to produce a torque by interaction with the field generated by the stator in the certain conditions below:

  1. Matching the pole pair of one of these rotating fields ($p_m \pm p_{mod}$) with the number of PM poles ($\pm p_s$) so that they can be locked at a specific torque angle.
  2. Rotor mechanical speed of $\omega_m = \pm\omega/p_{mod}$.

  Then, they can simply be represented as in below:

$$\frac{1}{2} h_m M_0 \wp_1 \cos\{(p_m - p_{\text{mod}})\theta - \omega_s t - p_{\text{m}}\zeta)\} \tag{4.131}$$

$$\frac{1}{2} h_m M_0 \wp_1 \cos\{(p_m + p_{\text{mod}})\theta - \omega_s t - p_{\text{m}}\zeta)\} \tag{4.132}$$

4.7.3 Finite element analysis of magnetic field modulation and gearing effect

In this section, we perform a finite element analysis to evaluate the idea of field modulation as well as the modeling. For the ease of analysis, we employ a stationary field produced by a sinusoidal surface current density $K_z(\theta)$ on an infinitely permeable back iron, in front of which we have the modulator ring and then the second back iron. The field in the two air-gaps will be analyzed to see how the modulation works when the field produced in the first air-gap passes the modulator ring and reaches the second air-gap. We also take a linearized geometry. The magnetomotive F is produced by the surface current density K_z given below:

$$F(x) = F_m \cos\left[p_s \left(\frac{2\pi}{L} \right) x \right] \tag{4.133}$$

Also,

$$K_z(x) = K_s \sin\left[p_s \left(\frac{2\pi}{L} \right) x \right] \tag{4.134}$$

where L is the horizontal length of the system and p_s is the number of poles of the stator. The DC component and the first three components of the air-gap permeance is taken into account as given below:

$$\wp(x) = \wp_0 + \wp_1 \cos\left[p_{\text{mod}} \left(\frac{2\pi}{L} \right) x \right] + \wp_2 \cos\left[2p_{\text{mod}} \left(\frac{2\pi}{L} \right) x \right] + \wp_3 \cos\left[3p_{\text{mod}} \left(\frac{2\pi}{L} \right) x \right] \tag{4.135}$$

where p_{mod} is the number of modulators. The magnetic flux density distribution is then calculated as in below:

$$B_y(x) = F(x)\wp(x) \tag{4.136}$$

By expressing the product of the two cosines in a sums, it is seen that the produced field has seven components with the following pole pairs:

- p_s pole pairs
- $p_{mod} \pm p_s$ pole pairs (with the same magnitude)

- *2* $p_{mod}\pm p_s$ pole pairs (with the same magnitude)
- *3* $p_{mod}\pm p_s$ pole pairs (with the same magnitude)

As shown in Fig. 4.27, finite element analysis is performed for such system in which $p_s=4$, $p_{mod}=15$, $L=10cm$ and $K_m=0.1\ A/mm^2$. The concept of modulation and flux paths can be seen.

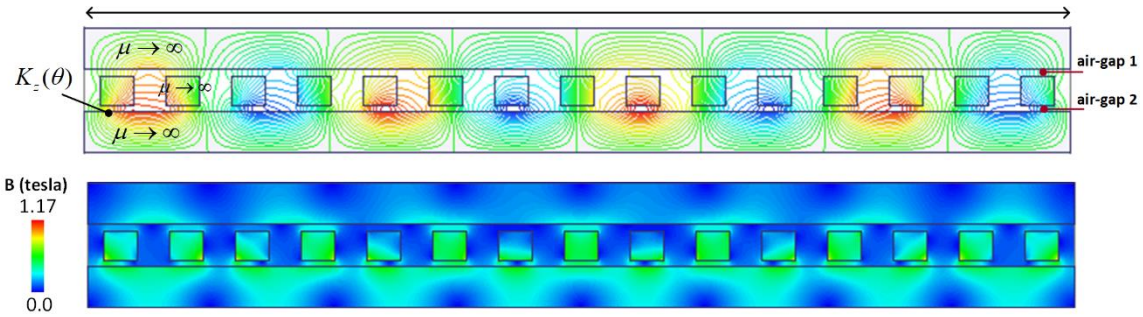

Figure 4.27: Flux lines and magnetic flux density distribution produced by a sinusoidal surface current density on the surface of the bottom back iron

Fig. 4.28 illustrates magnetic flux density distribution in the first and the second air-gaps whose FFT is shown in Fig. 4.29. The mentioned components obtained out of analytical computations can be observed in the space harmonic spectrum.

Observations:

- The significant point is that the magnitudes of the pairs of $p_{mod}\pm p_s$, *and* $2p_{mod}\pm p_s$, *or* $3p_{mod}\pm p_s$ are not the same, while they were equal in the analytical calculations. For example, magnitude of p_{mod}-p_s pole-pair spectrum is larger than $p_{mod}+p_s$ in the second air-gap. The reason might be the leakage fluxes or the effect of higher harmonics of the permeance distribution or the accuracy of its modeling.

- The ***gearing idea*** is to match the number of pole pairs of the PMs on the second back iron with one of the harmonics produced by modulation of the field generated in the first air-gap. Considering the first pair ($p_{mod}\pm p_s$), we have two options:

1) $p_m = p_{\text{mod}} - p_s$ (4.137)

2) $p_m = p_{\text{mod}} + p_s$ (4.138)

- Based on the FFF of the special distribution of field in the second air-gap, the first one has a higher magnitude, so it will be the best candidate for pole matching. Therefore, given the pole pair values of the stator p_s and the PM rotor p_m, the following number will be the candidate for the number of modulator pieces:

$$p_m = p_{\text{mod}} - p_s \quad \Rightarrow \quad p_{\text{mod}} = p_m + p_s \tag{4.139}$$

  For the studied case, we have $p_m=11$.

- Another reason for taking this option is that a higher number of modulator pieces means that the width of the modulators is smaller which allows flor less flux leakage.

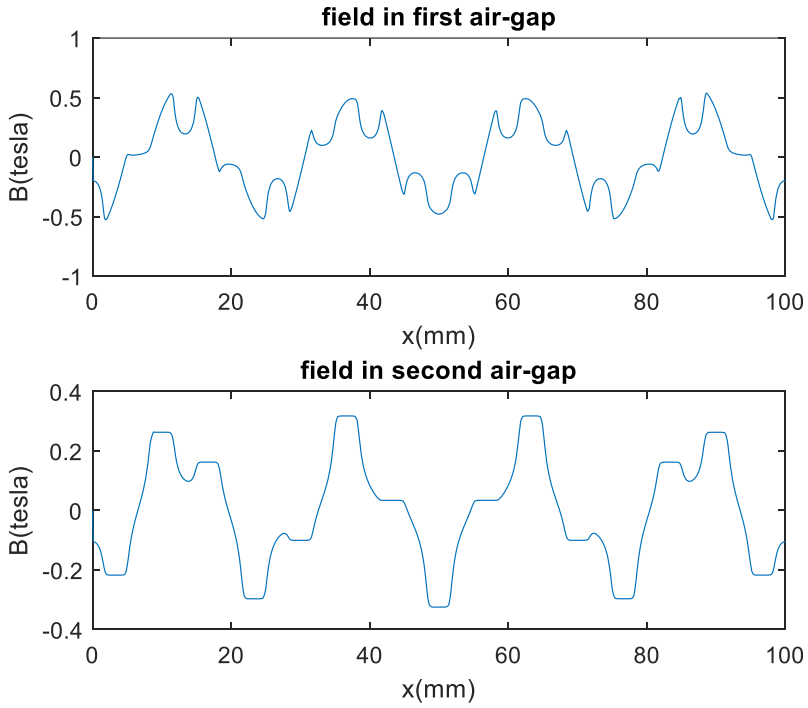

Figure 4.28: Magnetic flux density distribution in the first air-gap and the second air-gap

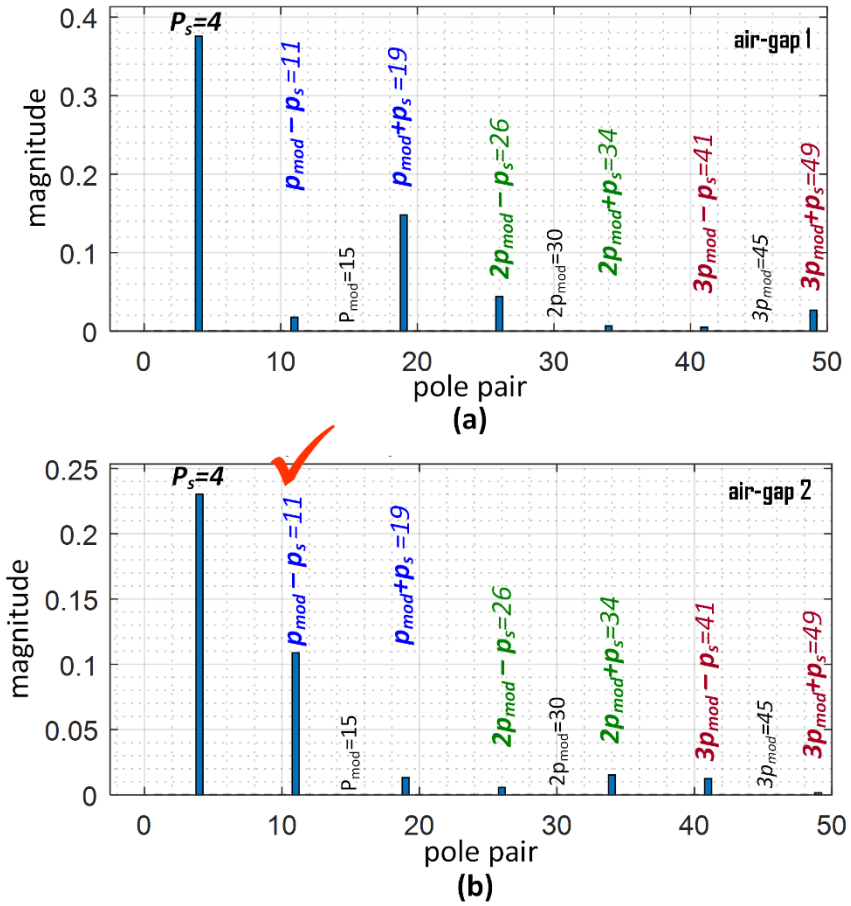

Figure 4.29: Space harmonic spectrum (pole pair of the field components) in the first and second air-gaps

4.8 Torque production in a geared machine with rotating modulators

Two analytical frameworks are proposed here to model magnetically-geared machines in which the modulators are the rotor. Fig. 4.30 shows the block diagram of the first method in which the developed torque is obtained using Maxwell stress tensor and Kelvin force. The stator current produces a MMF from which an equivalent surface current density on the surface of stator, which is also equal to the tangential component of the magnetic field intensity, is derived. Also, the MMF produced by permanent magnets and an equivalent surface charge density is derived. The radial component of the magnetic flux density is also obtained using the total MMF and the air-gap reluctance derived from flux tube modeling. Carter coefficient is used in the air-gap length corrections as well. Having both tangential and normal components of the magnetic field on the stator surface, the shear stress and

subsequently the developed torque on the stator side is determined using Maxwell stress tensor. Having the equivalent surface charge and the tangential component of the magnetic field on the surface of PMs, the shear stress and subsequently the developed torque on the PM side is determined using Kelvin force.

Fig. 4.31 shows the block diagram of the second method in which the developed torques on both stator and PM sides are obtained using Lorentz force. The stator current produces a MMF from which an equivalent surface current density on the surface of stator is derived. Also, the MMF produced by permanent magnets and an equivalent Amperian current density is derived. The radial component of the magnetic flux density is also obtained using the total MMF and the air-gap reluctance derived from flux tube modeling. Carter coefficient is used in the air-gap length corrections as well. Having the surface current density on the stator surface, Amperian current density in the PM region and also the radial component of the magnetic flux density, the developed torque can be easily obtained in both sides using Lorentz force.

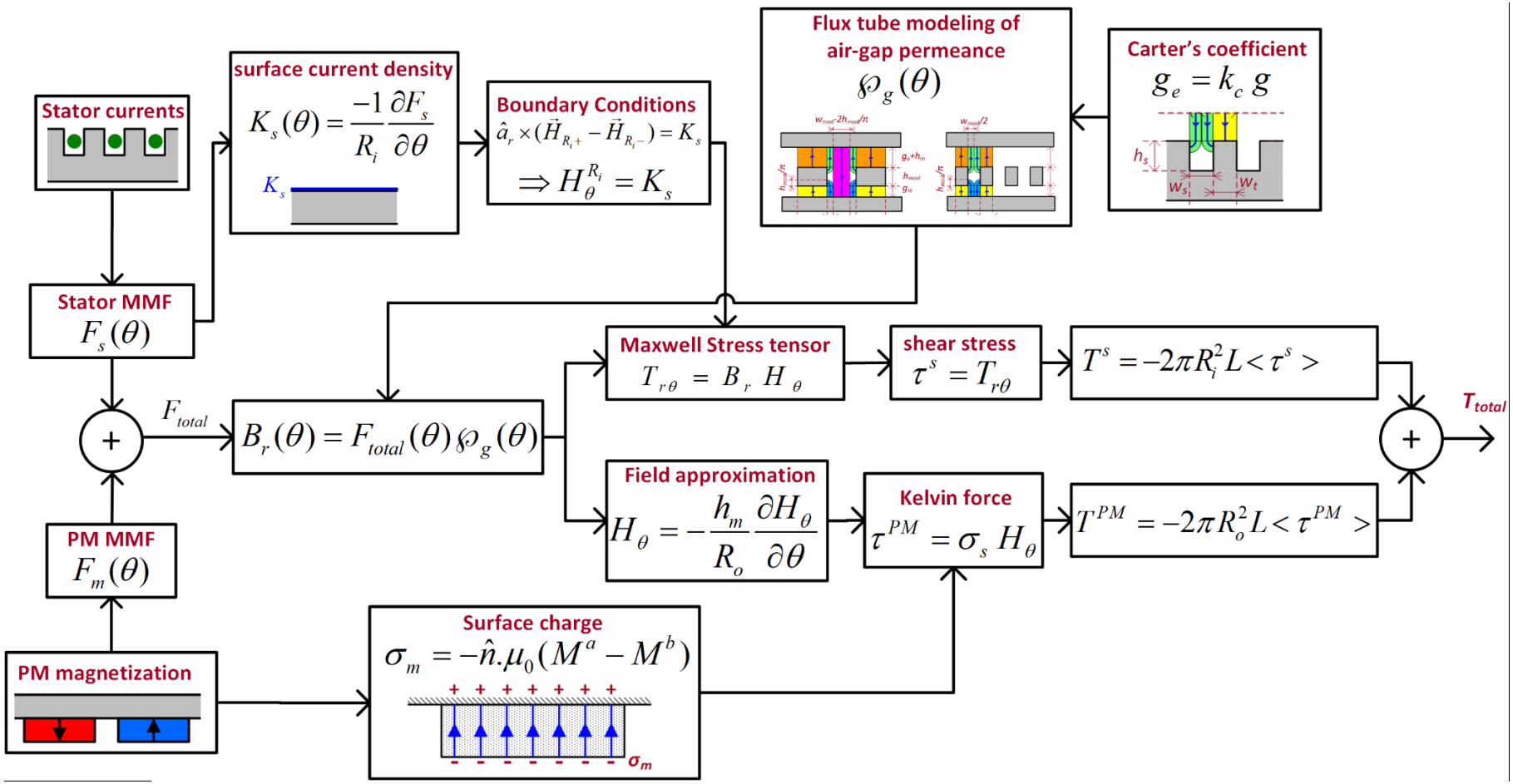

Figure 4.30: Block diagram of the analytical framework based on Maxwell stress tensor and Kelvin force

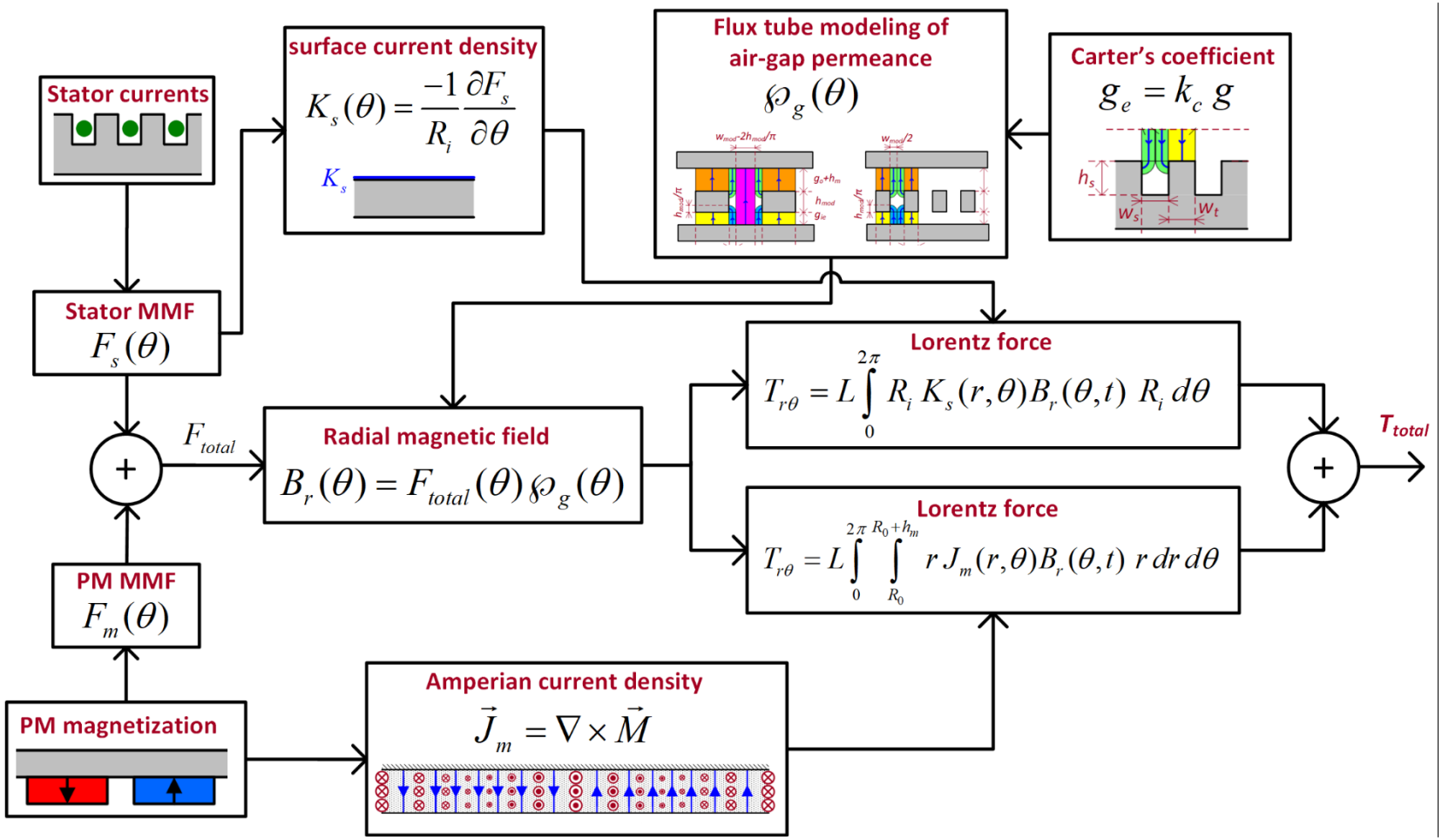

Figure 4. 31: Block diagram of the analytical based on framework using Lorentz force

4.8.1 Toque calculations using Maxwell stress tensor in radial-flux rotating machines

Maxwell stress tensor is usually employed in microscopic field description of forces—the way Poynting's theorem is used in field discretion of energy flow. Maxwell stress tensor is the rewritten form of Lorenz law and is solely in terms of magnetic fields, so it can be used to calculate force in situations in which the currents (charged particles) are not available or hard to calculate to be used in Lorentz force. In cylindrical coordinates *(r, θ, z)*, Maxwell stress tensor is as in below:

$$T = \begin{bmatrix} T_{rr} & T_{r\theta} & T_{rz} \\ T_{\theta r} & T_{\theta\theta} & T_{\theta z} \\ T_{zr} & T_{z\theta} & T_{zz} \end{bmatrix} \tag{4.140}$$

where stress tensor T_{ij} in electromagnetics is as in the following:

$$T_{ij} = \varepsilon_0 E_i E_j + \frac{1}{\mu_0} B_i B_j - \frac{1}{2}(\varepsilon_0 E^2 + \frac{1}{\mu_0} B^2)\,\delta_{ij} \tag{4.141}$$

where i and j can be r, θ or z, and δ_{ij} is the Kronecker's delta which is *1* if $i=j$, otherwise *0*. For magnetic fields, e.g. in electric machines, we have:

$$T_{ij} = \frac{1}{\mu_0} B_i B_j - \frac{1}{2\mu_0} B^2\,\delta_{ij} \tag{4.142}$$

where

$$B^2 = B_r^{\,2} + B_\theta^{\,2} + B_z^{\,2} \;\;;\;\; \vec{B} = B_r\,\hat{a}_r + B_\theta\,\hat{a}_\theta + B_z\,\hat{a}_z \tag{4.143}$$

Maxwell stress tensor can be rewritten as in below:

$$T = \frac{1}{\mu_0} \begin{bmatrix} \dfrac{B_r^{\,2} - B_\theta^{\,2} - B_z^{\,2}}{2} & B_r\,B_\theta & B_r\,B_z \\ B_\theta\,B_r & \dfrac{B_\theta^{\,2} - B_r^{\,2} - B_z^{\,2}}{2} & B_\theta\,B_z \\ B_z\,B_r & B_z\,B_\theta & \dfrac{B_z^{\,2} - B_r^{\,2} - B_\theta^{\,2}}{2} \end{bmatrix} \tag{4.144}$$

Similar to the role of Poynting vector *S* in field description of energy flow in Poynting's theorem, the divergence of the sensor in cylindrical coordinates is the vector of *volume force density* (with the dimension of N/m^3) as in the following:

$$\begin{aligned} f_v = \nabla.T = & \left(\frac{\partial A_{rr}}{\partial r} + \frac{1}{r}\frac{\partial A_{r\theta}}{\partial \theta} + \frac{\partial A_{rz}}{\partial z} + \frac{A_{rr} - A_{\theta\theta}}{r} \right) \hat{a}_r \\ & + \left(\frac{\partial A_{\theta r}}{\partial r} + \frac{1}{r}\frac{\partial A_{\theta\theta}}{\partial \theta} + \frac{\partial A_{\theta z}}{\partial z} + \frac{A_{\theta r} + A_{r\theta}}{r} \right) \hat{a}_\theta \\ & + \left(\frac{\partial A_{zr}}{\partial r} + \frac{1}{r}\frac{\partial A_{z\theta}}{\partial \theta} + \frac{\partial A_{zz}}{\partial z} + \frac{A_{zr}}{r} \right) \hat{a}_z \end{aligned} \tag{4.145}$$

Then, force (with the dimension of *N*) on an object surrounded by closed surface *S* having the volume *vol* can be obtained as in below:

$$F = \begin{bmatrix} F_r \\ F_\theta \\ F_z \end{bmatrix} = \iiint_{vol} \nabla.T \, dv \tag{4.146}$$

Using Stokes' theorem, we have:

$$F = \begin{bmatrix} F_r \\ F_\theta \\ F_z \end{bmatrix} = \oiint_S T.\hat{n} \, dA \tag{4.147}$$

As shown in Fig. 4.32, the stress on a surface has two components: the normal component which is called normal stress and the parallel component which is called shear stress. There are actually three stresses operating on a surface, two of which are parallel to surface whose resultant is the shear stress. The normal stress, which is actually the normal force per unit area, will be as in below:

$$\vec{\sigma}_n = (\vec{\sigma}.\hat{n})\,\hat{n} \tag{4.148}$$

The shear stress, which is actually the tangential force per unit area, is then the remaining as in below:

$$\vec{\tau} = \vec{\sigma} - (\vec{\sigma}.\hat{n})\hat{n} \tag{4.149}$$

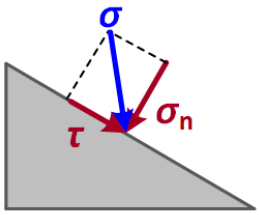

Figure 4.32: Stress, shear stress and normal stress

Then, the developed torque on a lever arm vector ***r*** is as in below:

$$T^e = \oiint_S \vec{r} \times (T.\hat{n})\, dA \tag{4.150}$$

Generally, for a surface having the unit normal vector of $n=(n_r, n_\theta, n_z)$, the *surface force density* (with the dimension of N/m^2) is as in below:

$$\vec{f} = \begin{bmatrix} f_r \\ f_\theta \\ f_z \end{bmatrix} = T.\hat{n} = \begin{bmatrix} T_{rr} & T_{r\theta} & T_{rz} \\ T_{\theta r} & T_{\theta\theta} & T_{\theta z} \\ T_{zr} & T_{z\theta} & T_{zz} \end{bmatrix} . \begin{bmatrix} n_r \\ n_\theta \\ n_z \end{bmatrix} = \begin{bmatrix} T_{rr}\,\hat{a}_r + T_{r\theta}\,\hat{a}_\theta + T_{rz}\,\hat{a}_z \\ T_{\theta r}\,\hat{a}_r + T_{\theta\theta}\,\hat{a}_\theta + T_{\theta z}\,\hat{a}_z \\ T_{zr}\,\hat{a}_r + T_{z\theta}\,\hat{a}_\theta + T_{zz}\,\hat{a}_z \end{bmatrix} \tag{4.151}$$

In two-dimensional analysis of radial-flux rotating machines having internal rotor, the magnetic field does not have any z-component ($B_z=0$), so $T_{iz}=T_{zi}=0$. As shown in Fig. 4.33, for a cylinder of radius R encompassing the rotor, normal vector of the side surface (S_{r+}), top surface (S_{z+}) and bottom surface (S_{z-}) are $n=(1, 0, 0)$, $n=(0, 0, 1)$ and $n=(0, 0, -1)$, respectively.

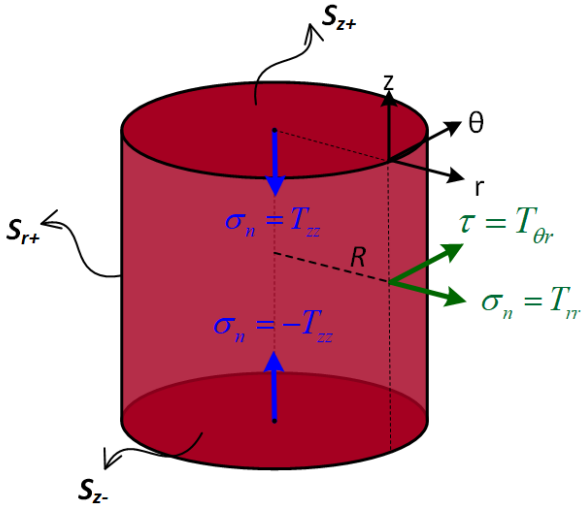

Figure 4.33: Stresses on a cylinder encompassing the rotor of a radial-flux rotating machine.

The force density on the closed surface integral over a cylinder surrounding the rotor can be separated into three open surface integrals of the side surface, the top surface and the bottom surface as in below:

$$F = \oiint_{S} (T.\hat{n})\, dA = \iint_{S_r} (T.\hat{a}_r)\, R\, d\theta\, dz + \iint_{S_{z+}} (T.\hat{a}_z)\, r\, dr\, d\theta + \iint_{S_{z-}} (T.-\hat{a}_z)\, r\, dr\, d\theta \quad (4.152)$$

As shown in Fig. 4.33, the tensor (force density vector) operating on the three surfaces of the cylinder are calculated as in below:

$$\vec{f}_{S_{r+}} = T.\hat{a}_r = \begin{bmatrix} T_{rr} = \dfrac{B_r{}^2 - B_\theta{}^2}{2\mu_0} & T_{r\theta} = \dfrac{1}{\mu_0} B_r\, B_\theta & 0 \\ T_{\theta r} = \dfrac{1}{\mu_0} B_\theta\, B_r & T_{\theta\theta} = \dfrac{B_\theta{}^2 - B_r{}^2}{2\mu_0} & 0 \\ 0 & 0 & T_{zz} = \dfrac{-B^2}{2\mu_0} \end{bmatrix} . \begin{bmatrix} 1 \\ 0 \\ 0 \end{bmatrix} = \begin{bmatrix} T_{rr} \\ T_{\theta r} \\ 0 \end{bmatrix} = T_{rr}\, \hat{a}_r + T_{\theta r}\, \hat{a}_\theta$$

(4.153)

$$\vec{f}_{S_{z+}} = T.\hat{a}_z = \begin{bmatrix} T_{rr} = \dfrac{B_r{}^2 - B_\theta{}^2}{2\mu_0} & T_{r\theta} = \dfrac{1}{\mu_0} B_r\, B_\theta & 0 \\ T_{\theta r} = \dfrac{1}{\mu_0} B_\theta\, B_r & T_{\theta\theta} = \dfrac{B_\theta{}^2 - B_r{}^2}{2\mu_0} & 0 \\ 0 & 0 & T_{zz} = \dfrac{-B^2}{2\mu_0} \end{bmatrix} . \begin{bmatrix} 0 \\ 0 \\ 1 \end{bmatrix} = \begin{bmatrix} 0 \\ 0 \\ T_{zz} \end{bmatrix} = T_{zz}\hat{a}_z \quad (4.154)$$

$$\vec{f}_{S_{z-}} = T.-\hat{a}_z = \begin{bmatrix} T_{rr} = \dfrac{B_r{}^2 - B_\theta{}^2}{2\mu_0} & T_{r\theta} = \dfrac{1}{\mu_0} B_r\, B_\theta & 0 \\ T_{\theta r} = \dfrac{1}{\mu_0} B_\theta\, B_r & T_{\theta\theta} = \dfrac{B_\theta{}^2 - B_r{}^2}{2\mu_0} & 0 \\ 0 & 0 & T_{zz} = \dfrac{-B^2}{2\mu_0} \end{bmatrix} . \begin{bmatrix} 0 \\ 0 \\ -1 \end{bmatrix} = \begin{bmatrix} 0 \\ 0 \\ -T_{zz} \end{bmatrix} = -T_{zz}\hat{a}_z$$

(4.155)

Therefore, the three integral can rewritten as in below:

$$F = \iint_{S_r} (T_{rr}\,\hat{a}_r + T_{\theta r}\,\hat{a}_\theta)\,R\,d\theta\,dz + \iint_{S_{z+}} T_{zz}\hat{a}_z\,r\,dr\,d\theta + \iint_{S_{z-}} (-T_{zz}\hat{a}_z)\,r\,dr\,d\theta \tag{4.156}$$

The last two terms will cancel. In fact, the negative sign in T_{zz} shows that the last two terms are just the forces which tend to keep the rotor within the stator region, produced by fluxes which tend to take the shortest path with the minimum reluctance. These normal stresses on these top and base surfaces are as in below:

$$S_{z+}: \quad \vec{\sigma}_n = \frac{-B^2}{2\mu_0}\vec{a}_z \tag{4.157}$$

$$S_{z-}: \quad \vec{\sigma}_n = \frac{B^2}{2\mu_0}\vec{a}_z \tag{4.158}$$

The stress on the side surface of the cylinder has two components: $T_{\theta r}$ in the tangential direction the contributes to the torque production and T_{rr} whose spatial average around the cylinder is zero because the normal force at any point on the cylinder will be canceled by a negative value on the opposite side. On the side surface, the shear stress and the normal stress can be obtained as:

$$S_{r+}: \quad \vec{\sigma}_n = (\vec{\sigma}.\hat{n})\,\hat{n} = [(T_{rr}\,\hat{a}_r + T_{\theta r}\,\hat{a}_\theta).\hat{a}_r]\,\hat{a}_r = T_{rr}\,\hat{a}_r = \frac{B_r{}^2 - B_\theta{}^2}{2\mu_0}\hat{a}_r \tag{4.159}$$

$$S_{r+}: \quad \vec{\tau} = \vec{\sigma} - (\sigma.\hat{n})\,\hat{n} = (T_{rr}\,\hat{a}_r + T_{\theta r}\,\hat{a}_\theta) - T_{rr}\,\hat{a}_r = T_{\theta r}\,\hat{a}_\theta = \frac{1}{\mu_0}B_r B_\theta\,\hat{a}_\theta \tag{4.160}$$

Therefore, the developed electromagnetic torque is as in below:

$$T^e = \iint_{S_{r+}} \vec{r} \times (T.\hat{n})\,dA \tag{4.161}$$

It leads to the following:

$$T^e = \int_0^L \int_0^{2\pi} R\,B_r H_\theta\,R\,d\theta\,dz = R^2 L \int_0^{2\pi} B_r(\theta) H_\theta(\theta)\,d\theta \tag{4.162}$$

where *C* can be any closed circle of radius *R* in the air-gap as shown in Fig. 4.34. In certain conditions where the shear stress on the surface has a spatial average of

$$< \tau >= \frac{1}{2\pi} \int_0^{2\pi} B_r(\theta) H_\theta(\theta)\, d\theta \tag{4.163}$$

the average toque will be

$$T^e = 2\pi R^2 L < \tau > \tag{4.164}$$

Observation:

- The clear observation in the above equation is that the developed torque is just the average shear stress <τ> (average force density) times the surface area $2\pi RL$ times the torque leg *R*.

- We know that this equation leads to the same torque regardless of the circle path *C* of radius *R* we take, so the stress should be larger for lower radii.

  $$R_1 < R_2 \;\Rightarrow\; \tau_1 > \tau_2 \tag{4.165}$$

- The the torque is independent of *R* and can be calculated from the closed line integral over ANY circle *C* in the air-gap region.

  $$< \tau >= \frac{1}{2\pi} \oint_C B_r(\theta) H_\theta(\theta)\, dl \tag{4.166}$$

  $$T^e = R^2 L \oint_C B_r(\theta) H_\theta(\theta)\, d\theta \tag{4.167}$$

- Since the shear stress and the torque are independent of the radius of the cylinder, they can be obtained from averaging over air-gap volume (or air-gap area in 2D analysis). It is useful in FEM when the meshed air-gap is not very fine.

  $$T^e = \frac{1}{R_o - R_i} \int_0^L \int_{R_i}^{R_o} \int_0^{2\pi} r\, B_r(\theta) H_\theta(\theta)\, r\, dr\, d\theta\, dz \tag{4.168}$$

  so

$$T^e = \frac{1}{R_o - R_i} \int_0^L \int_{R_i}^{R_o} \int_0^{2\pi} r\, B_r(\theta) H_\theta(\theta)\, r\, dr\, d\theta\, dz = \frac{L}{R_o - R_i} \iint_{S_g} B_r(\theta) H_\theta(\theta)\, r^2 dr\, d\theta \tag{4.169}$$

where R_i and R_o can be inner and outer radii of the air-gap region (hollow cylinder). The arbitrary circle C in the air-gap and the air-gap surface area S_g (yellow area) are shown in Fig. 4.34.

- If the normal and tangential components of the field are orthogonal, the average shear stress will be zero. The following trigonometric pairs are orthogonal:
  - $\sin p_1\theta$ *and* $\sin p_2\theta$ *where* $p_1 \neq p_2$
  - $\sin p_1\theta$ *and* $\cos p_2\theta$ *where* $p_1 \neq p_2$
  - $\sin p\theta$ *and* $\cos p\theta$

  Therefore, the pair that results in a nonzero average shear stress is:
  - $\sin p\theta$ *and* $\sin(p\theta - \theta_0)$ *where* $\theta_0 \neq \frac{\pi}{2}$

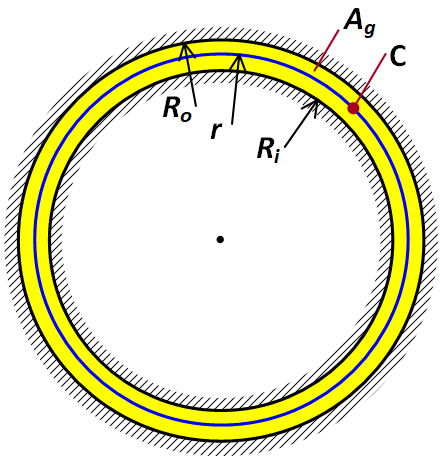

Figure 4.34: Arbitrary closed line C and air-gap surface area Ag employed in torque calculations using Maxwell stress tensor.

It is worth noting that the developed electromagnetic torque can be obtained from the shear stress on either stator or rotor. As illustrated in Fig. 4.35, it can be shown that the shear stresses on the two sides of the air-gap are in opposite directions. Unit normal vector of the rotor surface is in +r direction, so we have:

$$T^{rotor}.\hat{a}_r = \begin{bmatrix} T_{rr} & T_{r\theta} & T_{rz} \\ T_{\theta r} & T_{\theta\theta} & T_{\theta z} \\ T_{zr} & T_{z\theta} & T_{zz} \end{bmatrix}.\begin{bmatrix} 1 \\ 0 \\ 0 \end{bmatrix} = \begin{bmatrix} T_{rr}\,\hat{a}_r + T_{r\theta}\,\hat{a}_\theta \\ 0 \\ 0 \end{bmatrix} \tag{4.170}$$

Unit normal vector of the stator surface is in -r direction, so we have:

$$T^{stator}.-\hat{a}_r = \begin{bmatrix} T_{rr} & T_{r\theta} & T_{rz} \\ T_{\theta r} & T_{\theta\theta} & T_{\theta z} \\ T_{zr} & T_{z\theta} & T_{zz} \end{bmatrix}.\begin{bmatrix} -1 \\ 0 \\ 0 \end{bmatrix} = \begin{bmatrix} -(T_{rr}\,\hat{a}_r + T_{r\theta}\,\hat{a}_\theta) \\ 0 \\ 0 \end{bmatrix} \tag{4.171}$$

It is seen that both shear and normal stresses are in the opposite directions.

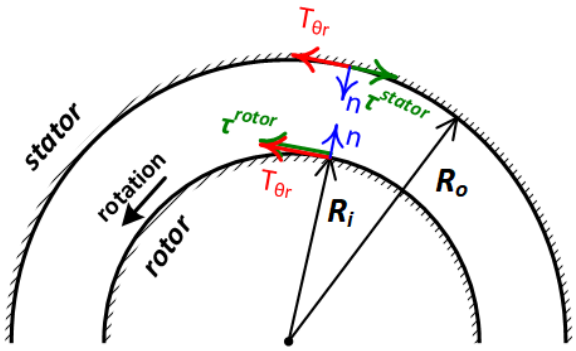

Figure 4.35: Maxwell stress tensor and shear stress on the surfaces of rotor and stator

We should be careful about the fact that a minus sign comes in if the torque calculated using the shear stress on the stationary part—the stator, so

$$T^e = 2\pi R_i^2 L < \tau_{rotor} > = -2\pi R_o^2 L < \tau_{stator} > \tag{4.172}$$

The point is that we take the one whose calculation is easier according to the situation we have. For example, in case of having a surface current density on the surface of an infinitely permeable iron, the tangential magnetic field intensity is just equal to the surface current density. Since the calculated torque is constant regardless of the radius, the shear stress is larger on the surface of rotor than on the surface of stator for an inner-rotor radial-flux machine:

$$R_i < R_o \quad \Rightarrow \quad |\tau_{rotor}| > |\tau_{stator}| \tag{4.173}$$

It is also consistent with fact that the fields B_r and H_θ are larger on rotor surface (smaller radii) than on stator surface (larger radii). Also, in cases where the air-gap length is very small compared to rotor radius ($g<<R_i$), the torque can be calculated using the average radius and the shear stress on either side, and also the shear stresses have equal amplitudes but opposite directions.

$$T^e = 2\pi {R_{ave}}^2 L < \tau_{rotor} > = -2\pi {R_{ave}}^2 L < \tau_{stator} > \tag{4.174}$$

$$< \tau_{rotor} > \approx - < \tau_{stator} > \tag{4.175}$$

4.8.2 Torque on stator side using Maxwell stress tensor

Fig. 4.36 shows the stress tensors and shear stresses on the surfaces of stator, PM ring and modulator ring for the radial-flux magnetically-geared machine having rotating modulators. It is seen that:

- shear stresses on the two sides of each of the air-gaps are in the opposites direction.
- the shear stress on a surface whose normal is in +z direction is equal to the Maxwell stress tensor on that surface, i.e. the stator surface and outer surface of the modulator ring.
- the shear stress on a surface whose normal is in -z direction is equal to the minus Maxwell stress tensor on that surface, i.e. surface of the PM ring and inner surface of the modulator ring.

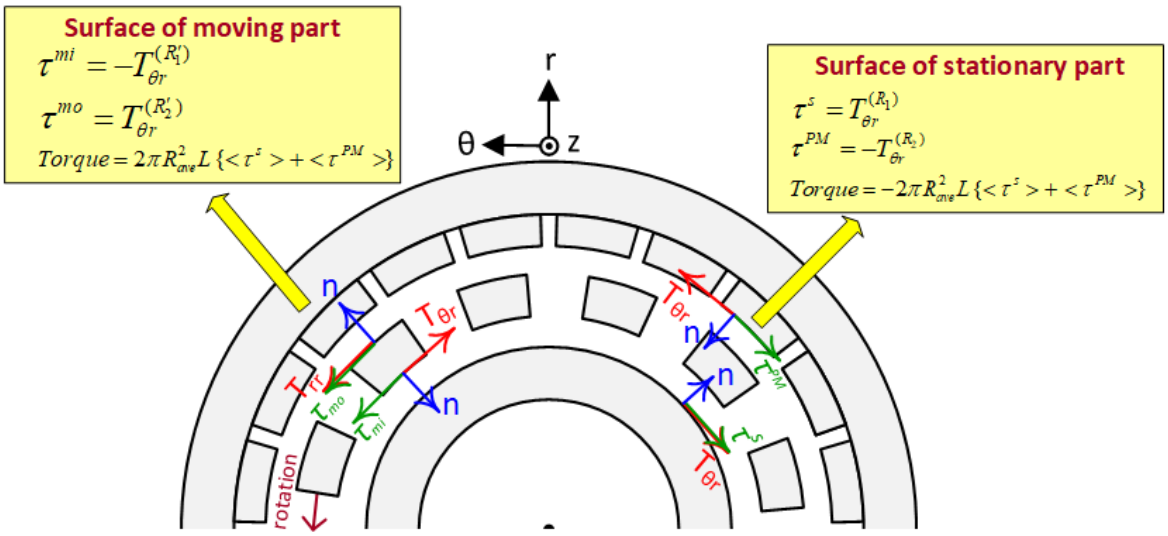

Figure 4.36: Maxwell stress tensors and shear stresses on the surfaces of stator, PM ring and modulator ring in a magnetically-geared machine

For the ease of calculation of the torque produced in the first air-gap, we try to extract the Maxwell stress tensor and the shear stress on the surface of the stator on which H_θ can be easily obtained through boundary conditions. As calculated, we have:

$$H_\theta(\theta,t) = H_{\theta 1}\cos\left(p_s\theta - \omega t - \delta\right) \tag{4.176}$$

The shear stress, which is also equal to the Maxwell stress tensor $T_{\theta r}$ radius R_i, is as in the following:

$$\begin{aligned}
\tau_s = T_{\theta r} &= H_\theta B_r \\
&= H_{\theta 1}\cos\left(p_s\theta - \omega t - \delta\right)\times \\
&\quad \left\{F_{s1}\wp_0 \sin\left(p_s\theta - \omega t - \delta\right)\right. \\
&\quad + \frac{1}{2}F_{s1}\wp_1 \sin\left[(p_s - p_{\text{mod}})\theta - (\omega - p_{\text{mod}}\omega_m)t - \delta + p_{\text{mod}}\zeta\right] \\
&\quad + \frac{1}{2}F_{s1}\wp_1 \sin\left[(p_s + p_{\text{mod}})\theta - (\omega + p_{\text{mod}}\omega_m)t - \delta - p_{\text{mod}}\zeta\right] \\
&\quad + h_m M_0 \wp_0 \cos p_m\theta \\
&\quad + \frac{1}{2}h_m M_0 \wp_1 \cos\left[(p_m - p_{\text{mod}})\theta + p_{\text{mod}}\omega_m t + p_{\text{mod}}\zeta\right] \\
&\quad \left. + \frac{1}{2}h_m M_0 \wp_1 \cos\left[(p_m + p_{\text{mod}})\theta - p_{\text{mod}}\omega_m t - p_{\text{mod}}\zeta\right]\right\}
\end{aligned} \tag{4.177}$$

It can be observed that:

- the first, the second, the third and the forth terms of the radial component of flux density are orthogonal to the tangential component of the field intensity, so the spatial average of their multiplication is zero, and their interaction doesn't produce any average shear stress.
- the fifth and the sixth terms are not orthogonal to the tangential component of the field intensity, so their interaction might be able to produce a shear stress and contribute in the torque production in certain conditions: *matching of pole pairs and rotation speeds*.
- either the fifth term or the sixth term can produce an average shear stress. They cannot average to a non-zero value at the same time because the number of poles in H_θ cannot match the number of poles of both terms (p_m-p_{mod} and p_m+p_{mod}). Both cases will be analyzed.

Employing the fifth term of the flux density:

By employing the fifth term of the radial component of the magnetic flux density, the shear stress can be written as:

$$\begin{aligned}\tau_s &= H_{\theta 1}\cos\left(p_s\theta-\omega t-\delta\right)\\ &\times\frac{1}{2}h_m M_0 \wp_1\cos\left[(p_m-p_{\mathrm{mod}})\theta+p_{\mathrm{mod}}\omega_m t+p_{\mathrm{mod}}\zeta\right]\end{aligned} \tag{4.178}$$

To produce an average shear stress, the pole pairs and the rotation speeds must match. By the way, the product of the two cosines can be expressed in a sum as in below:

$$\begin{aligned}\tau_s &= \frac{1}{4}H_{\theta 1}h_m M_0 \wp_1\cos\left[(p_s-p_m+p_{\mathrm{mod}})\theta-(\omega+p_{\mathrm{mod}}\omega_m)t-\delta-p_{\mathrm{mod}}\zeta\right]\\ &+\frac{1}{4}H_{\theta 1}h_m M_0 \wp_1\cos\left[(p_s+p_m-p_{\mathrm{mod}})\theta-(\omega-p_{\mathrm{mod}}\omega_m)t-\delta+p_{\mathrm{mod}}\zeta\right]\end{aligned} \tag{4.179}$$

Any of the two parts above might lead to a constant value and have a non-zero spatial average if the two conditions below are met:

- ***pole condition:*** the coefficient of θ is zero

- ***speed condition:*** the coefficient of *t* is zero

Again, either the first part or the second part can meet the two mentioned conditions. They cannot both meet the two conditions at the same time. Both cases will be analyzed.

Meeting the pole and speed conditions for the first part of the fifth term:

- *pole condition:*

$$p_s - p_m + p_{\text{mod}} = 0 \;\Rightarrow\; p_{\text{mod}} = p_m - p_s \tag{4.180}$$

- *speed condition:*

$$\omega + p_{\text{mod}}\omega_m = 0 \;\Rightarrow\; \omega_m = -\frac{\omega}{p_{\text{mod}}} \tag{4.181}$$

The first condition is the proposed number of modulators and the second is the mechanical speed of the rotor in the reverse direction of the excitation. In this case, the shear stress is:

$$\tau_s = \frac{1}{4} H_{\theta 1} h_m M_0 \wp_1 \cos\left(\delta + p_{\text{mod}}\zeta\right) \tag{4.182}$$

This situation is a candidate.

Meeting the pole and speed conditions for the second part of the fifth term:

- *pole condition:*

$$p_s + p_m - p_{\text{mod}} = 0 \;\Rightarrow\; p_{\text{mod}} = p_m + p_s \tag{4.183}$$

- *speed condition:*

$$\omega - p_{\text{mod}}\omega_m = 0 \;\Rightarrow\; \omega_m = \frac{\omega}{p_{\text{mod}}} \tag{4.184}$$

The first condition is the proposed number of modulators and the second is the mechanical speed of the rotor in the same direction as the excitation. In this case, the shear stress is:

$$\tau_s = \frac{1}{4} H_{\theta 1} h_m M_0 \wp_1 \cos\left(\delta - p_{\text{mod}}\zeta\right) \tag{4.185}$$

This situation is a candidate.

Which term should be chosen?

As observed in the finite element analysis of the radial component of the magnetic flux density distribution (section 4.7.3), magnitude of the lowest harmonics produced by the modulation is larger, so it would be the candidate ($p_{mod}=p_s+p_m$). Another reason for taking this option is that a higher number of modulator pieces means that the width of the modulators is smaller which allows flor less flux leakage.

Employing the sixth term of the flux density:

Now is the turn for analyzing the next case. By employing the sixth term of the radial component of the magnetic flux density, the shear stress can be written as:

$$\begin{aligned}\tau_s &= H_{\theta 1}\cos\left(p_s\theta-\omega t-\delta\right)\\ &\times+\frac{1}{2}h_m M_0 \wp_1 \cos\left[(p_m+p_{\mathrm{mod}})\theta-p_{\mathrm{mod}}\omega_m t-p_{\mathrm{mod}}\zeta\right]\end{aligned} \tag{4.186}$$

To produce an average shear stress, the pole pairs and the rotation speeds must match. By the way, the product of the two cosines can be expressed in a sum as in below:

$$\begin{aligned}\tau_s &= \frac{1}{4}H_{\theta 1}h_m M_0 \wp_1 \cos\left[(p_s-p_m-p_{\mathrm{mod}})\theta-(\omega-p_{\mathrm{mod}}\omega_m)t-\delta+p_{\mathrm{mod}}\zeta\right]\\ &+\frac{1}{4}H_{\theta 1}h_m M_0 \wp_1 \cos\left[(p_s+p_m+p_{\mathrm{mod}})\theta-(\omega+p_{\mathrm{mod}}\omega_m)t-\delta-p_{\mathrm{mod}}\zeta\right]\end{aligned} \tag{4.187}$$

Similar to the previous case, any of the two parts above might lead to a constant value and have a non-zero spatial average if the pole and the speed conditions are met. Again, either the first part or the second part can meet the two mentioned conditions. They cannot both meet the two conditions at the same time. Both cases will be analyzed.

Meeting the pole and speed conditions for the first part of the sixth term:

- *pole condition:*

$$p_s-p_m-p_{\mathrm{mod}}=0 \;\Rightarrow\; p_{\mathrm{mod}}=-(p_m-p_s) \tag{4.188}$$

- *speed condition:*

$$\omega - p_{\text{mod}}\omega_m = 0 \;\Rightarrow\; \omega_m = \frac{\omega}{p_{\text{mod}}} \tag{4.189}$$

The first condition is the proposed number of modulators and the second is the mechanical speed of the rotor in the same direction as the excitation. In this case, the shear stress is:

$$\tau_s = \frac{1}{4} H_{\theta 1} h_m M_0 \wp_1 \cos\left(\delta - p_{\text{mod}}\zeta\right) \tag{4.190}$$

Meeting the pole and speed conditions for the second part of the sixth term:

- *pole condition:*

$$p_s + p_m + p_{\text{mod}} = 0 \;\Rightarrow\; p_{\text{mod}} = -(p_m + p_s) \tag{4.191}$$

- *speed condition:*

$$\omega + p_{\text{mod}}\omega_m = 0 \;\Rightarrow\; \omega_m = -\frac{\omega}{p_{\text{mod}}} \tag{4.192}$$

The first condition is the proposed number of modulators and the second is the mechanical speed of the rotor in the reverse direction of the excitation. In this case, the shear stress is:

$$\tau_s = \frac{1}{4} H_{\theta 1} h_m M_0 \wp_1 \cos\left(\delta + p_{\text{mod}}\zeta\right) \tag{4.193}$$

Which term should be chosen?

The two parts of the last term are the candidates.

Developed torque:

It seen that employing the fifth or the sixth term results in the same derivations with a minus sine difference. Generally, the shear stress for the rotor rotation in both directions is as in below:

$$\tau_s = \frac{1}{4} H_{\theta 1} h_m M_0 \wp_1 \cos\left(\delta \mp p_{\text{mod}}\zeta\right) \qquad ; \omega_m = \pm\frac{\omega}{p_{\text{mod}}} \tag{4.194}$$

where

$$H_{\theta 1} = \frac{3}{2}\frac{4}{\pi}\frac{NI_s}{2R_i}k_w \quad ; M_0 = \frac{4}{\pi}\frac{B_r}{\mu_0}\sin\frac{p_m\theta_m}{2} \tag{4.195}$$

Being careful about the negative sign, the developed electromagnetic torque can be calculated using the shear stress on the surface of stator as in below:

$$T^e{}_{stator} = -2\pi R_i^2 L < \tau_s > \tag{4.196}$$

By substituting $<\tau_s>$, M_0 and $H_{\theta 1}$, we obtain:

$$T^e{}_{stator} = -\frac{3}{2}\frac{4}{\pi}\frac{B_r}{\mu_0}R_i L k_w N I_s h_m \wp_1 \sin\frac{p_m\theta_m}{2}\cos\left(\delta \mp p_{\text{mod}}\zeta\right) \quad ; \omega_m = \pm\frac{\omega}{p_{\text{mod}}} \tag{4.197}$$

4.8.3 Torque on stator side using Lorentz force

Lorentz electromagnetics force acting on a particle of charge q with a velocity v in an electric field $\boldsymbol{E}$ and a magnetic field $\boldsymbol{B}$ is as in below [42]:

$$\vec{F} = q(\vec{E} + \vec{v} \times \vec{B}) \tag{4.198}$$

Having the volume charge density ρ, the volume force density is as in the following

$$\vec{f} = \rho(\vec{E} + \vec{v} \times \vec{B}) \tag{4.199}$$

The current density corresponding to a charge density ρ having speed of **v** is $\boldsymbol{J}=\rho\,\boldsymbol{v}$. Then, the Lorentz force density can be rewritten as in below:

$$\vec{f} = \rho\vec{E} + \vec{J} \times \vec{B} \tag{4.200}$$

In the presence of only magnetic fields, for example in electric machines, it reduces to:

$$\vec{f} = \vec{J} \times \vec{B} \tag{4.201}$$

Then, the developed torque in the volume *vol* can be obtained as in below:

$$T^e = \iiint_{vol} \vec{r} \times \vec{f}\, dv = \iiint_{vol} \vec{r} \times \vec{J} \times \vec{B}\, dv \tag{4.202}$$

In two-dimensional analysis of electric machines in cylindrical coordinates, where current density J_z is in the z-direction and magnetic flux density B_r is in r-direction, the developed torque is obtained as in below:

$$T^e = L\iint_S r\, J_z(r,\theta)\, B_r(r,\theta)\, r\, dr\, d\theta \tag{4.203}$$

In the cases where there exists a surface current density K_z on the circle path C having a radius R, the developed torque is calculated as in below:

$$T^e = L\int_C R\, K_z(\theta)\, B_r(R,\theta)\, R\, d\theta = LR^2\int_C K_z(\theta)\, B_r(R,\theta)\, d\theta \tag{4.204}$$

Having the fundamental component of the surface current density on the surface of the stator as shown in Fig. 4.37 and given below:

$$K_z(\theta,t) = K_{z1}\cos\left(p_s\theta - \omega t - \delta\right) \tag{4.205}$$

the developed torque can be obtained by Lorentz law as in the following:

$$T^e{}_{stator}(t) = LR_i^2\int_0^{2\pi} K_z(\theta,t)\, B_r(\theta,t)\, d\theta \tag{4.206}$$

where, by substituting K_z and B_r, the term inside the integral can be written as in below:

$$\begin{aligned} K_z(\theta,t)\, B_r(\theta,t) = {} & K_{z1}\cos\left(p_s\theta - \omega t - \delta\right)\times \\ & \Big\{F_{s1}\wp_0 \sin\left(p_s\theta - \omega t - \delta\right) \\ & + \frac{1}{2}F_{s1}\wp_1 \sin\left[(p_s - p_{\mathrm{mod}})\theta - (\omega - p_{\mathrm{mod}}\omega_m)t - \delta + p_{\mathrm{mod}}\zeta\right] \\ & + \frac{1}{2}F_{s1}\wp_1 \sin\left[(p_s + p_{\mathrm{mod}})\theta - (\omega + p_{\mathrm{mod}}\omega_m)t - \delta - p_{\mathrm{mod}}\zeta\right] \\ & + h_m M_0 \wp_0 \cos p_m\theta \\ & + \frac{1}{2}h_m M_0 \wp_1 \cos\left[(p_m - p_{\mathrm{mod}})\theta + p_{\mathrm{mod}}\omega_m t + p_{\mathrm{mod}}\zeta\right] \\ & + \frac{1}{2}h_m M_0 \wp_1 \cos\left[(p_m + p_{\mathrm{mod}})\theta - p_{\mathrm{mod}}\omega_m t - p_{\mathrm{mod}}\zeta\right]\Big\} \end{aligned} \tag{4.207}$$

Taking the same analysis as in the previous section, substituting the simplified term into the torque expression, and calculating the integral leads to the same formulations.

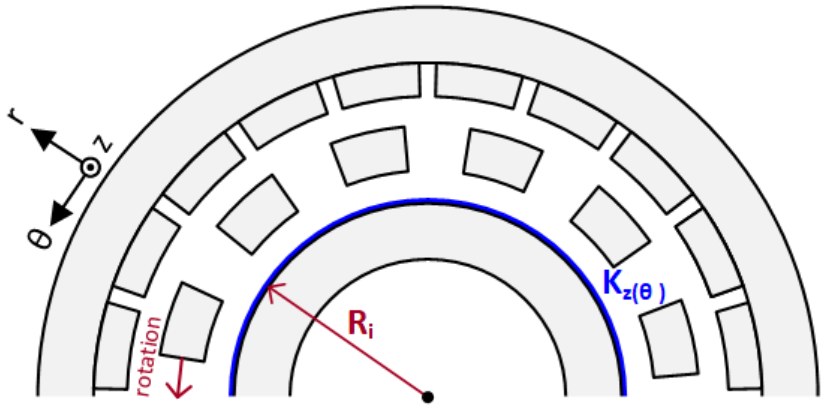

Figure 4.37: Surface current density of stator

4.8.4 Torque on PM side using Kelvin force and magnetic charge model of PMs

Kelvin magnetization force density can be used in finding the force on a magnetic charge in the presence of a magnetic field [42]-[43]. Force density acting on magnetic charge density ρ_m in a magnetic field of $\boldsymbol{H}$ can be obtained as in the following:

$$\vec{f} = \rho_m \vec{H} \tag{4.208}$$

Also, force density acting on magnetic surface charge density σ_m in a magnetic field of $\boldsymbol{H}$ can be obtained as in the following:

$$\vec{f} = \sigma_m \vec{H} \tag{4.209}$$

where, in the case of the studied magnetic gear, the magnetic field $\boldsymbol{H}$ has two components as in below:

$$\vec{H} = H_r \hat{a}_r + H_\theta \hat{a}_\theta \tag{4.210}$$

Because of symmetry, the resultant force in the radial direction produced by H_r is zero and only H_θ produces a shear stress on PMs represented by the fundamental of the surface charge density distribution as shown in Fig. 4.38 and given in the following:

$$\sigma_m(\theta) = -\mu_0 M_0 \cos p_m \theta \tag{4.211}$$

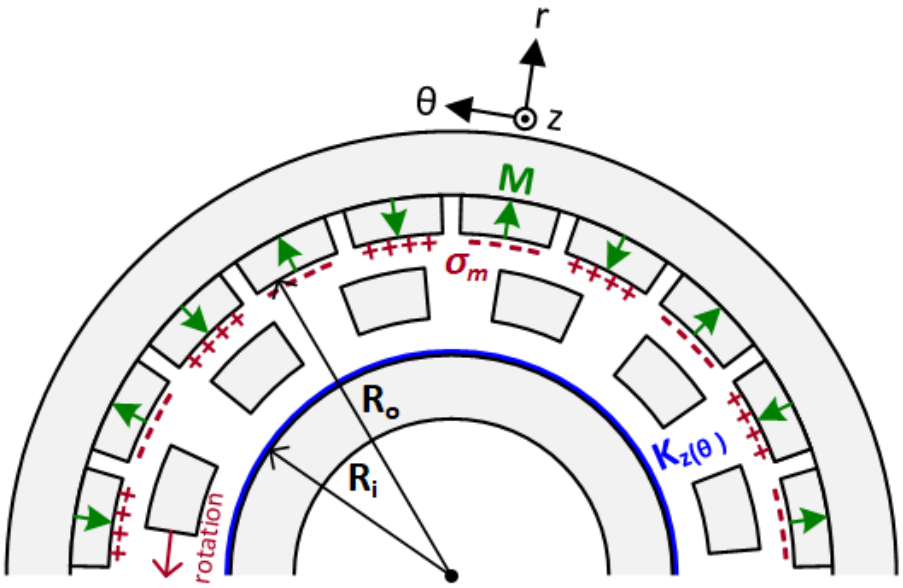

Figure 4.38: Equivalent surface magnetic charge density of PMs

Tangential component of the magnetic field intensity on the surface of PMs can also be calculated as in below:

$$H_\theta\big|_{r=R_o} = -\frac{h_m}{R_o}\frac{\partial H_r}{\partial \theta} \tag{4.212}$$

Substitution of $H_r = B_r/\mu_0$ from section 4.7.1 yields the following:

$$
\begin{aligned}
H_\theta\big|_{r=R_o} = & -\frac{h_m}{\mu_0 R_o}\times \\
& \Big\{F_{s1}\wp_0 p_s \cos\big(p_s\theta-\omega t-\delta\big) \\
& +\frac{1}{2}F_{s1}\wp_1(p_s-p_{\mathrm{mod}})\cos\big[(p_s-p_{\mathrm{mod}})\theta-(\omega-p_{\mathrm{mod}}\omega_m)t-\delta+p_{\mathrm{mod}}\zeta\big] \\
& +\frac{1}{2}F_{s1}\wp_1(p_s+p_{\mathrm{mod}})\cos\big[(p_s+p_{\mathrm{mod}})\theta-(\omega+p_{\mathrm{mod}}\omega_m)t-\delta-p_{\mathrm{mod}}\zeta\big] \\
& -h_m M_0\wp_0 p_m \sin p_m\theta \\
& -\frac{1}{2}h_m M_0\wp_1(p_m-p_{\mathrm{mod}})\sin\big[(p_m-p_{\mathrm{mod}})\theta+p_{\mathrm{mod}}\omega_m t+p_{\mathrm{mod}}\zeta\big] \\
& -\frac{1}{2}h_m M_0\wp_1(p_m+p_{\mathrm{mod}})\sin\big[(p_m+p_{\mathrm{mod}})\theta-p_{\mathrm{mod}}\omega_m t-p_{\mathrm{mod}}\zeta\big]\Big\}
\end{aligned}
\tag{4.213}
$$

The shear stress on the PMs can be calculated as:

$$
\begin{aligned}
\tau_m &= \sigma_m(\theta)H_\theta(\theta,t) \\
&= M_0\frac{h_m}{R_o}\cos p_m\theta \\
&\quad \times\Big\{F_{s1}\wp_0 p_s \cos\big(p_s\theta-\omega t-\delta\big) \\
&\quad +\frac{1}{2}F_{s1}\wp_1(p_s-p_{\mathrm{mod}})\cos\big[(p_s-p_{\mathrm{mod}})\theta-(\omega-p_{\mathrm{mod}}\omega_m)t-\delta+p_{\mathrm{mod}}\zeta\big] \\
&\quad +\frac{1}{2}F_{s1}\wp_1(p_s+p_{\mathrm{mod}})\cos\big[(p_s+p_{\mathrm{mod}})\theta-(\omega+p_{\mathrm{mod}}\omega_m)t-\delta-p_{\mathrm{mod}}\zeta\big] \\
&\quad -h_m M_0\wp_0 p_m \sin p_m\theta \\
&\quad -\frac{1}{2}h_m M_0\wp_1(p_m-p_{\mathrm{mod}})\sin\big[(p_m-p_{\mathrm{mod}})\theta+p_{\mathrm{mod}}\omega_m t+p_{\mathrm{mod}}\zeta\big] \\
&\quad -\frac{1}{2}h_m M_0\wp_1(p_m+p_{\mathrm{mod}})\sin\big[(p_m+p_{\mathrm{mod}})\theta-p_{\mathrm{mod}}\omega_m t-p_{\mathrm{mod}}\zeta\big]\Big\}
\end{aligned}
\tag{4.214}
$$

It can be observed that:

- the first, the forth, the fifth and the sixth terms of the tangential component of the field H_θ are orthogonal to the surface charge distribution, so the spatial average of their multiplication is zero, and their interaction doesn't produce any average shear stress.
- the second and the third terms are not orthogonal to the tangential component of the field intensity, so their interaction might be able to produce a shear stress and contribute in the torque production in certain conditions: *matching of pole pairs and rotation speeds*.
- either the second term or the third term can produce an average shear stress. They cannot average to a non-zero value at the same time because the number of poles in σ_m cannot match the number of poles of both terms (p_s-p_{mod} and p_s+p_{mod}). Both cases will be analyzed.

Employing the second term of the flux density:

By employing the second term of the tangential component of the magnetic flux density, the shear stress can be written as:

$$\begin{aligned}\tau_m &= M_0 \frac{h_m}{R_o}\cos p_m\theta \\ &\times\frac{1}{2}F_{s1}\wp_1(p_s-p_{\mathrm{mod}})\cos\left[(p_s-p_{\mathrm{mod}})\theta-(\omega-p_{\mathrm{mod}}\omega_m)t-\delta+p_{\mathrm{mod}}\zeta\right]\end{aligned} \tag{4.215}$$

To produce an average shear stress, the pole pairs and the rotation speeds must match. By the way, the product of the two cosines can be expressed in a sum as in below:

$$\begin{aligned}\tau_m &= \frac{1}{4}\frac{h_m}{R_o}M_0F_{s1}\wp_1(p_s-p_{\mathrm{mod}})\cos\left[(p_m-p_s+p_{\mathrm{mod}})\theta+(\omega-p_{\mathrm{mod}}\omega_m)t+\delta-p_{\mathrm{mod}}\zeta\right] \\ &+\frac{1}{4}\frac{h_m}{R_o}M_0F_{s1}\wp_1(p_s-p_{\mathrm{mod}})\cos\left[(p_m+p_s-p_{\mathrm{mod}})\theta-(\omega-p_{\mathrm{mod}}\omega_m)t-\delta+p_{\mathrm{mod}}\zeta\right]\end{aligned} \tag{4.216}$$

Any of the two parts above might lead to a constant value and have a non-zero spatial average if the two conditions below are met:

- ***pole condition:*** the coefficient of θ is zero
- ***speed condition:*** the coefficient of t is zero

Again, either the first part or the second part can meet the two mentioned conditions. They cannot both meet the two conditions at the same time. Both cases will be analyzed.

Meeting the pole and speed conditions for the first part of the second term:

- *pole condition:*

$$p_m - p_s + p_{\text{mod}} = 0 \Rightarrow p_{\text{mod}} = -(p_m - p_s) \tag{4.217}$$

- *speed condition:*

$$\omega - p_{\text{mod}}\omega_m = 0 \Rightarrow \omega_m = \frac{\omega}{p_{\text{mod}}} \tag{4.218}$$

The first condition is the proposed number of modulators and the second is the mechanical speed of the rotor in the same direction the excitation. In this case, the shear stress is:

$$\tau_m = \frac{1}{4}\frac{h_m}{R_o} M_0 F_{s1} \wp_1 p_m \cos(\delta - p_{\text{mod}}\zeta) \tag{4.219}$$

Meeting the pole and speed conditions for the second part of the second term:

- *pole condition:*

$$p_m + p_s - p_{\text{mod}} = 0 \Rightarrow p_{\text{mod}} = p_m + p_s \tag{4.220}$$

- *speed condition:*

$$\omega - p_{\text{mod}}\omega_m = 0 \Rightarrow \omega_m = \frac{\omega}{p_{\text{mod}}} \tag{4.221}$$

The first condition is the proposed number of modulators and the second is the mechanical speed of the rotor in the same direction as the excitation. In this case, the shear stress is:

$$\tau_m = -\frac{1}{4}\frac{h_m}{R_o} M_0 F_{s1} \wp_1 p_m \cos(\delta - p_{\text{mod}}\zeta) \tag{4.222}$$

This situation is a candidate.

Which term should be chosen?

The second term is taken, so it would be the candidate ($p_{mod}=p_s+p_m$).

Employing the third term of the flux density:

By employing the third term of the tangential component of the magnetic flux density, the shear stress can be written as:

$$\tau_m = M_0 \frac{h_m}{R_o} \cos p_m\theta \times \frac{1}{2} F_{s1} \wp_1 (p_s + p_{\text{mod}}) \cos\left[(p_s + p_{\text{mod}})\theta - (\omega + p_{\text{mod}}\omega_m)t - \delta - p_{\text{mod}}\zeta\right] \tag{4.223}$$

To produce an average shear stress, the pole pairs and the rotation speeds must match. By the way, the product of the two cosines can be expressed in a sum as in below:

$$\tau_m = \frac{1}{4}\frac{h_m}{R_o} M_0 F_{s1} \wp_1 (p_s + p_{\text{mod}}) \cos\left[(p_m - p_s - p_{\text{mod}})\theta + (\omega + p_{\text{mod}}\omega_m)t + \delta + p_{\text{mod}}\zeta\right] + \frac{1}{4}\frac{h_m}{R_o} M_0 F_{s1} \wp_1 (p_s + p_{\text{mod}}) \cos\left[(p_m + p_s + p_{\text{mod}})\theta - (\omega + p_{\text{mod}}\omega_m)t - \delta - p_{\text{mod}}\zeta\right] \tag{4.224}$$

Any of the two parts above might lead to a constant value and have a non-zero spatial average if the pole and the speed conditions are met. Again, either the first part or the second part can meet the two mentioned conditions. They cannot both meet the two conditions at the same time. Both cases will be analyzed.

Meeting the pole and speed conditions for the first part of the third term:

- *pole condition:*

$$p_m - p_s - p_{\text{mod}} = 0 \Rightarrow p_{\text{mod}} = p_m - p_s \tag{4.225}$$

- *speed condition:*

$$\omega + p_{\text{mod}}\omega_m = 0 \Rightarrow \omega_m = -\frac{\omega}{p_{\text{mod}}} \tag{4.226}$$

The first condition is the proposed number of modulators and the second is the mechanical speed of the rotor in the same direction the excitation. In this case, the shear stress is:

$$\tau_m = \frac{1}{4}\frac{h_m}{R_o} M_0 F_{s1} \wp_1 p_{\mathrm{m}} \cos(\delta + p_{\mathrm{mod}}\zeta) \tag{4.227}$$

This situation is a candidate.

Meeting the pole and speed conditions for the second part of the third term:

- *pole condition:*

$$p_m + p_s + p_{\mathrm{mod}} = 0 \;\Rightarrow\; p_{\mathrm{mod}} = -(p_m + p_s) \tag{4.228}$$

- *speed condition:*

$$\omega + p_{\mathrm{mod}}\omega_m = 0 \;\Rightarrow\; \omega_m = -\frac{\omega}{p_{\mathrm{mod}}} \tag{4.229}$$

The first condition is the proposed number of modulators and the second is the mechanical speed of the rotor in the same direction as the excitation. In this case, the shear stress is:

$$\tau_m = -\frac{1}{4}\frac{h_m}{R_o} M_0 F_{s1} \wp_1 p_{\mathrm{m}} \cos(\delta + p_{\mathrm{mod}}\zeta) \tag{4.230}$$

Which term should be chosen?

Second part of the second term and first part of the third term are the cases.

Developed torque:

Taking the second part of the second term (positive speed $\omega_m=\omega/p_{mod}$ and $p_{mod}=p_m+p_s$) and first part of the third term (negative speed $\omega_m=-\omega/p_{mod}$ and $p_{mod}=p_m-p_s$), the shear stress for the rotor rotation in both directions is as in below:

$$\tau_m = \mp\frac{1}{4}\frac{h_m}{R_o} M_0 F_{s1} \wp_1 p_{\mathrm{m}} \cos(\delta \mp p_{\mathrm{mod}}\zeta) \qquad ;\omega_m = \pm\frac{\omega}{p_{\mathrm{mod}}} \tag{4.231}$$

where

$$F_{s1} = -\frac{3}{2}\frac{4}{\pi}\frac{NI_s}{2p_s}k_w \qquad ; M_0 = \frac{4}{\pi}\frac{B_r}{\mu_0}\sin\frac{p_m\theta_m}{2} \tag{4.232}$$

Being careful about the negative sign, the developed electromagnetic torque can be calculated using the shear stress on the surface of PMs as in below:

$$T^e{}_{PM} = -2\pi R_o{}^2 L < \tau_m > \tag{4.233}$$

By substituting $<\tau_s>$, M_0 and $H_{\theta 1}$, we obtain:

$$T^e{}_{PM} = \mp\frac{3}{2}\frac{4}{\pi}\frac{p_{\mathrm{m}}}{p_s}\frac{B_r}{\mu_0}R_o L k_w N I_s h_m \wp_1 \sin\frac{p_m\theta_m}{2}\cos(\delta \mp p_{\mathrm{mod}}\zeta) \qquad ; \omega_m = \pm\frac{\omega}{p_{\mathrm{mod}}} \tag{4.234}$$

4.8.5 Torque on PM side using Lorentz force and Amperian current model of PMs

The permanent magnets can also be represented by Amperian currents based on which the developed torque can be obtained using Lorentz force. The equivalent current density of PMs is as in below:

$$J_m(r,\theta) = \frac{M_0 p_m}{r}\sin p_m\theta \tag{4.235}$$

The developed torque can be calculated using the following surface integral over the area *S* shown in Fig. 4.39 as in the following:

$$\begin{aligned} T^e{}_{PM} &= -L\int_0^{2\pi}\int_{R_o}^{R_o+h_m} r\, J_m(r,\theta)\, B_r(\theta,t)\, r\, dr\, d\theta \\ &= -L\int_0^{2\pi}\int_{R_o}^{R_o+h_m} r\left(\frac{M_0 p_m}{r}\sin p_m\theta\right) B_r(\theta,t)\, r\, dr\, d\theta \\ &= -LM_0 p_m \int_{R_o}^{R_o+h_m} r\, dr \int_0^{2\pi} \sin p_m\theta\, B_r(\theta,t)\, d\theta \\ &= -\frac{1}{2}LM_0 p_m (2R_o h_m + h_m{}^2)\int_0^{2\pi} \sin p_m\theta\, B_r(\theta)\, d\theta \end{aligned} \tag{4.236}$$

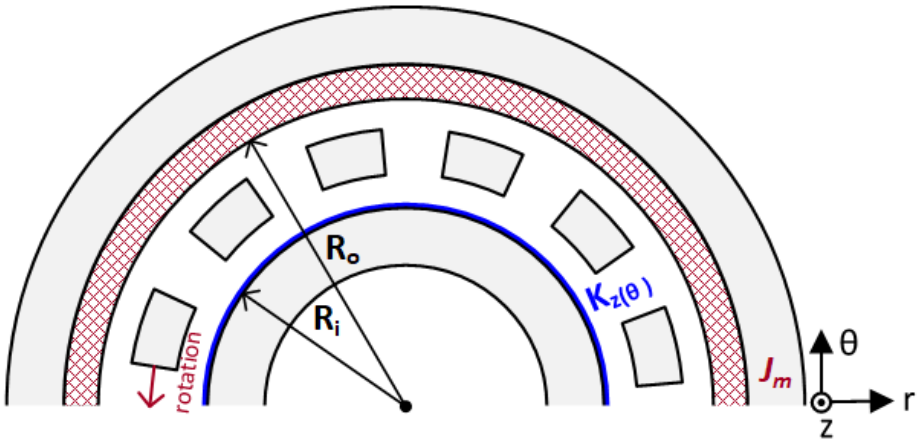

Figure 4.39: Equivalent Amperian current density distribution of PMs

The minus sign is because we are calculating the modulator torque using PM ring torque. The term inside the integral can be written as:

$$\begin{aligned}\sin p_m\theta\, B_r(\theta)\, d\theta = \sin p_m\theta \times \\ \Big\{ & F_{s1}\wp_0 \sin\left(p_s\theta - \omega t - \delta\right) \\ & + \frac{1}{2}F_{s1}\wp_1 \sin\left[(p_s - p_{\text{mod}})\theta - (\omega - p_{\text{mod}}\omega_m)t - \delta + p_{\text{mod}}\zeta\right] \\ & + \frac{1}{2}F_{s1}\wp_1 \sin\left[(p_s + p_{\text{mod}})\theta - (\omega + p_{\text{mod}}\omega_m)t - \delta - p_{\text{mod}}\zeta\right] \\ & + h_m M_0 \wp_0 \cos p_m\theta \\ & + \frac{1}{2}h_m M_0 \wp_1 \cos\left[(p_m - p_{\text{mod}})\theta + p_{\text{mod}}\omega_m t + p_{\text{mod}}\zeta\right] \\ & + \frac{1}{2}h_m M_0 \wp_1 \cos\left[(p_m + p_{\text{mod}})\theta - p_{\text{mod}}\omega_m t - p_{\text{mod}}\zeta\right]\Big\}\end{aligned} \tag{4.237}$$

Spatial average of the product of *sin* $p_m\theta$ with the first, the forth, the fifth and the sixth terms is zero because they are orthogonal, but the second and the third terms of B_r might be able to produce a torque. Product of *sin* $p_m\theta$ with the second term of B_r will be:

$$\begin{aligned}&\frac{1}{4}F_{s1}\wp_1 \cos\left[(p_m - p_s + p_{\text{mod}})\theta + (\omega - p_{\text{mod}}\omega_m)t + \delta - p_{\text{mod}}\zeta\right] \\ -&\frac{1}{4}F_{s1}\wp_1 \cos\left[(p_m + p_s - p_{\text{mod}})\theta - (\omega - p_{\text{mod}}\omega_m)t - \delta + p_{\text{mod}}\zeta\right]\end{aligned} \tag{4.238}$$

Meeting the pole condition $p_{mod}=p_s-p_m$ and the speed condition $\omega_m=\omega/p_{mod}$ for the first part, or meeting the pole condition $p_{mod}=p_s+p_m$ and the speed condition $\omega_m=\omega/p_{mod}$ for the second part, it reduces to:

$$\pm\frac{1}{4}F_{s1}\wp_1\cos(\delta-p_{\mathrm{mod}}\zeta) \tag{4.239}$$

Product of $\sin p_m\theta$ with the third term of B_r will be:

$$\begin{aligned}&\frac{1}{4}F_{s1}\wp_1\cos\left[(p_m-p_s-p_{\mathrm{mod}})\theta+(\omega+p_{\mathrm{mod}}\omega_m)t+\delta+p_{\mathrm{mod}}\zeta\right]\\&-\frac{1}{4}F_{s1}\wp_1\cos\left[(p_m+p_s+p_{\mathrm{mod}})\theta-(\omega+p_{\mathrm{mod}}\omega_m)t-\delta-p_{\mathrm{mod}}\zeta\right]\end{aligned} \tag{4.240}$$

Meeting the pole condition $p_{mod}=p_m-p_s$ and the speed condition $\omega_m=-\omega/p_{mod}$ for the first part, or meeting the pole condition $p_{mod}=-(p_s+p_m)$ and the speed condition $\omega_m=-\omega/p_{mod}$ for the second part, it reduces to:

$$\pm\frac{1}{4}F_{s1}\wp_1\cos(\delta+p_{\mathrm{mod}}\zeta) \tag{4.241}$$

Taking the second part of the product with the second term and first part of the product with the third term, and substitution of the two terms in the torque equation gives the following:

$$T^e{}_{PM}=\pm\frac{\pi}{4}LM_0p_mF_{s1}\wp_1(2R_oh_m+h_m{}^2)\cos(\delta\mp p_{\mathrm{mod}}\zeta);\quad \omega_m=\pm\frac{\omega}{p_{mod}} \tag{4.242}$$

Substitution of F_{s1} and M_0 results in the following equation:

$$T^e{}_{PM}=\mp\frac{3}{4}\frac{4}{\pi}\frac{p_m}{p_s}\frac{B_r}{\mu_0}\frac{1}{2}(2R_oh_m+h_m{}^2)L\ k_wN\ I_s\wp_1\sin\frac{p_m\theta_m}{2}\cos(\delta\mp p_{\mathrm{mod}}\zeta);\quad \omega_m=\pm\frac{\omega}{p_{mod}} \tag{4.243}$$

For relatively large machines, we have:

$$R_o \gg h_m \quad \Rightarrow \quad 2R_o h_m + h_m{}^2 \approx 2R_o h_m \tag{4.244}$$

Then, the developed torque can be calculated as in below:

$$T^e{}_{PM} = \mp \frac{3}{2}\frac{4}{\pi}\frac{p_m}{p_s}\frac{B_r}{\mu_0} R_o L k_w N I_s h_m \wp_1 \sin\frac{p_m \theta_m}{2} \cos(\delta \mp p_{\text{mod}}\zeta) \;\; ; \;\; \omega_m = \pm\frac{\omega}{p_{mod}} \tag{4.245}$$

It is seen that the value obtained from this method is the same as the previous method if $R_o >> h_m$.

4.8.6 Total torque

In the case of rotating

$$T^e = T^e{}_{stator} + T^e{}_{PM} \tag{4.246}$$

Substitution of the two term leads to the following expression:

$$\begin{aligned} T^e &= -\frac{3}{2}\frac{4}{\pi}\frac{B_r}{\mu_0} R_i L k_w N I_s h_m \wp_1 \sin\frac{p_m \theta_m}{2} \cos\left(\delta \mp p_{\text{mod}}\zeta\right) \\ &\quad \mp \frac{3}{2}\frac{4}{\pi}\frac{p_m}{p_s}\frac{B_r}{\mu_0} R_o L k_w N I_s h_m \wp_1 \sin\frac{p_m \theta_m}{2} \cos(\delta \mp p_{\text{mod}}\zeta) \\ &= -\frac{3}{2}\frac{4}{\pi}\left(R_i \pm R_o \frac{p_m}{p_s}\right)\frac{B_r}{\mu_0} L k_w N I_s h_m \wp_1 \sin\frac{p_m \theta_m}{2} \cos\left(\delta \mp p_{\text{mod}}\zeta\right) \;\; ; \;\; \omega_m = \pm\frac{\omega}{p_{mod}} \end{aligned} \tag{4.247}$$

The ± in the cosine argument is according to the mechanical speed $\omega_m = \pm\omega/p_{mod}$. The ± behind the ±pm/ps is based on the pole combination which is negative if $p_{mod}=p_m+p_s$ (so the shear stresses will add) and positive if $p_{mod}=p_m-p_s$ (so shear stresses will subtract). For relatively large machines, we have:

$$R_i \;\; and \;\; R_o \gg h_{\text{mod}} \quad \Rightarrow \quad R_i \approx R_o \approx R_{av} \tag{4.248}$$

Then- we have:

$$T^e = -\frac{3}{2}\frac{4}{\pi}\left(1 \pm \frac{p_m}{p_s}\right)\frac{B_r}{\mu_0} R_{av} L k_w N I_s h_m \wp_1 \sin\frac{p_m \theta_m}{2} \cos\left(\delta \mp p_{\text{mod}} \zeta\right) \quad ; \quad \omega_m = \pm\frac{\omega}{p_{mod}} \tag{4.249}$$

Defining the torque angle as in below:

$$\beta = \delta \mp p_{\text{mod}} \zeta \tag{4.250}$$

we have:

$$T^e = -\frac{3}{2}\frac{4}{\pi}\left(1 \pm \frac{p_m}{p_s}\right)\frac{B_r}{\mu_0} R_{av} L k_w N I_s h_m \wp_1 \sin\frac{p_m \theta_m}{2} \sin\beta \quad ; \quad \omega_m = \pm\frac{\omega}{p_{mod}} \tag{4.251}$$

Torque angle characteristics of the machine is shown in Fig. 4.40. Unit check for the torque expression is done in Appendix C.

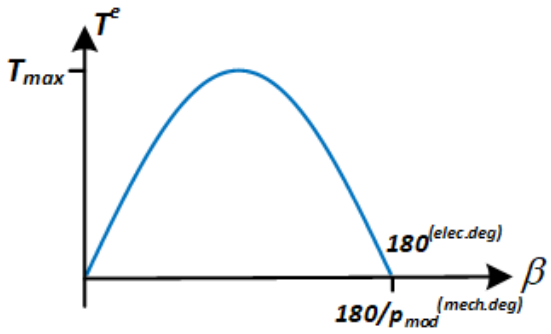

Figure 4.40: Torque angle characteristics for a geared machine with rotating modulators

4.8.7 Gearing effect

The ratio between the toque produced on the stator and the PM sides is as in below:

$$\frac{T^e_{PM}}{T^e_{stator}} = \pm\frac{p_m}{p_s} \tag{4.252}$$

The positive sign is for the pole combination $p_{mod}=p_m+p_s$ in which the shear stresses in the two sides of the modulator will add, while the negative sign is for the pole combination $p_{mod}=p_m-p_s$ in which the shear stresses in the two sides of the modulator will subtract.

The gearing ratio, defined as ratio of the torque on the rotor (modulators) to the torque on the stator, can be calculated as in below:

$$\frac{T_{\text{mod}}}{T_s} = \frac{p_{\text{mod}}}{p_s} = \frac{p_s \pm p_m}{p_s} \tag{4.253}$$

Defining the speed ratio as the ratio of the rotating field of the stator to the mechanical speed of the rotor (modulator ring), we have:

$$\frac{\Omega_{\text{mod}}}{\Omega_s} = \frac{\pm\omega / p_{\text{mod}}}{\omega / p_s} = \frac{p_s}{\pm p_{\text{mod}}} = \frac{p_s}{p_s \pm p_m} \tag{4.254}$$

If $p_m > p_s$, we will end in a geared machine having lower speed and a higher torque.

4.8.8 Power balance

The power into the machine (in motoring case) is the developed electromagnetic torque of the stator times the velocity of the stator rotating filed as in below:

$$P_s = T^e{}_{stator}\,\Omega_s = T_s \frac{\omega}{p_s} = \frac{\omega}{p_s} \times -\frac{3}{2}\frac{4}{\pi}\frac{B_r}{\mu_0} R_{av} L k_w N I_s h_m \wp_1 \sin\frac{p_m \theta_m}{2} \sin\beta \tag{4.255}$$

It is worth noting that negative electrical power refers to the stator as an input port — motoring mode, while a positive electrical power refers to an output port—generating mode.

The mechanical power is the total torque at the rotor (modulator ring) times the mechanical speed of the machine as in below

$$\begin{aligned} P_{mech} &= P_{\text{mod}} = T^e \Omega_{\text{m}} = T^e \frac{\omega}{p_{\text{mod}}} \\ &= \pm\frac{\omega}{p_{\text{mod}}} \times -\frac{3}{2}\frac{4}{\pi}\left(1 \pm \frac{p_m}{p_s}\right)\frac{B_r}{\mu_0} R_{av} L k_w N I_s h_m \wp_1 \sin\frac{p_m \theta_m}{2} \sin\beta \\ &= \frac{\omega}{p_s} \times -\frac{3}{2}\frac{4}{\pi}\frac{B_r}{\mu_0} R_{av} L k_w N I_s h_m \wp_1 \sin\frac{p_m \theta_m}{2} \sin\beta \end{aligned} \tag{4.256}$$

Knowing that $p_s \pm pm = \pm p_{mod}$, the power balance can be observed.

4.9 Torque production in a machine with rotating PMs

Two analytical frameworks are proposed here to model magnetically-geared machines in which the Pm ring are the rotor. Fig. 4.41 shows the block diagram of the first method in which the developed torque is obtained Kelvin force. The stator current produces a MMF. Also, the MMF produced by permanent magnets and an equivalent surface charge density is derived. The radial component of the magnetic flux density is also obtained using the total MMF and the air-gap reluctance derived from flux tube modeling. Carter coefficient is used in the air-gap length corrections as well. Having the equivalent surface charge and the tangential component of the magnetic field on the surface of PMs, the shear stress and subsequently the developed torque on the PM side is determined using Kelvin force.

Fig. 4.42 shows the block diagram of the second method in which the developed torques on PM side is obtained using Lorentz force. The stator current produces a MMF. Also, the MMF produced by permanent magnets and an equivalent Amperian current density is derived. The radial component of the magnetic flux density is also obtained using the total MMF and the air-gap reluctance derived from flux tube modeling. Carter coefficient is used in the air-gap length corrections as well. Having the Amperian current density in the PM region and also the radial component of the magnetic flux density, the developed torque can be easily obtained using Lorentz force.

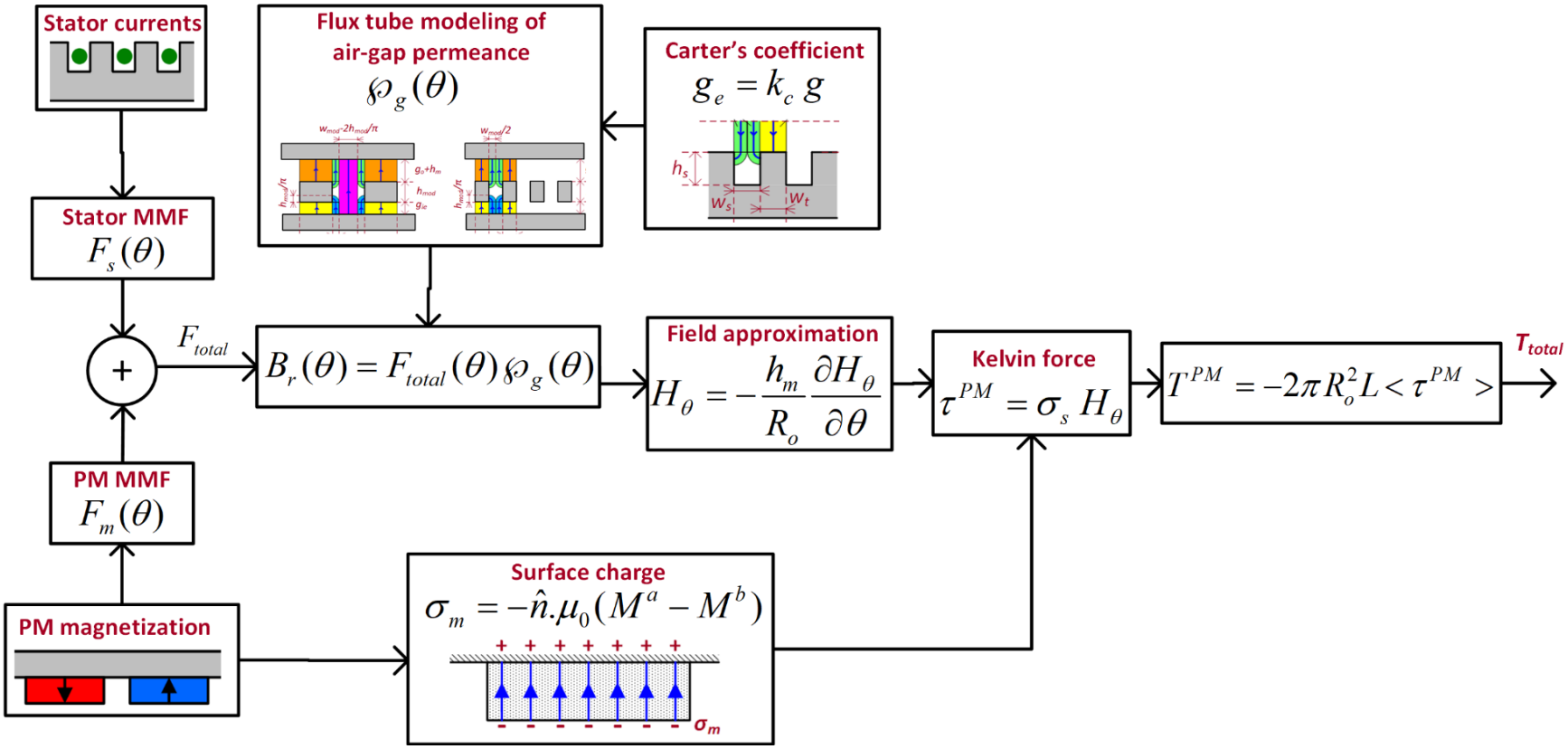

Figure 4. 41: Block diagram of the analytical framework based on Kelvin Force

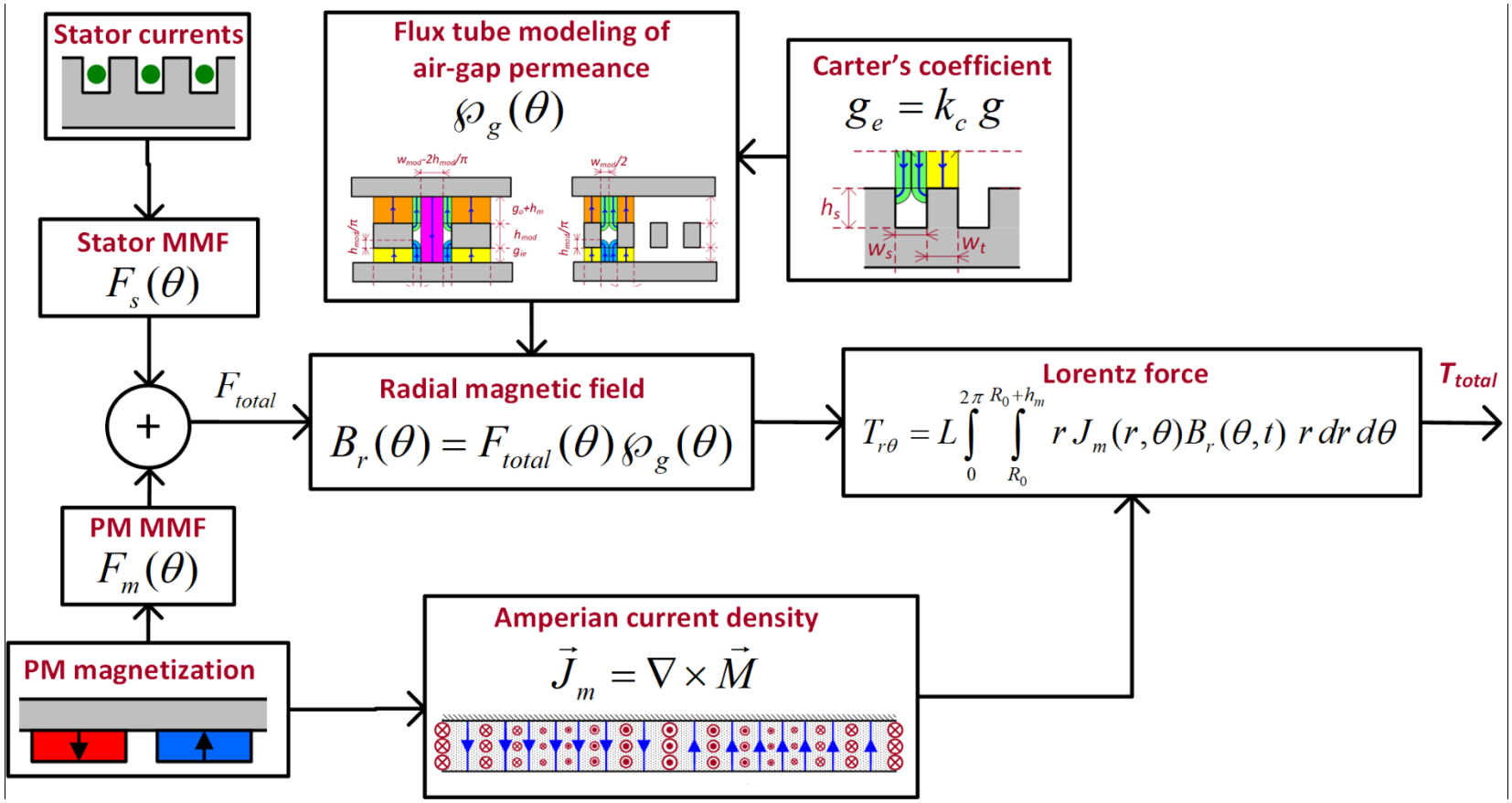

Figure 4. 42: Block diagram of the analytical framework based on Lorentz force

4.9.1 Torque on PM rotor using Kelvin force and magnetic charge model of PMs

The fundamental component of the surface charge density distribution is as in below:

$$\sigma_m(\theta,t) = -\mu_0 M_0 \cos p_m(\theta - \omega_m t - \zeta) \tag{4.257}$$

Tangential component of the magnetic field intensity on the surface of PMs can also be calculated as in below:

$$H_\theta\big|_{r=R_o} = -\frac{h_m}{R_o}\frac{\partial H_r}{\partial \theta} \tag{4.258}$$

Substitution of $H_r = B_r/\mu_0$ from section 4.7.2 yields the following:

$$\begin{aligned} B_r(\theta,t) = {} & F_{s1}\wp_0 \sin\left(p_s\theta - \omega t - \delta\right) \\ & + \frac{1}{2}F_{s1}\wp_1 \sin\left[(p_s - p_{\text{mod}})\theta - \omega t - \delta\right] \\ & + \frac{1}{2}F_{s1}\wp_1 \sin\left[(p_s + p_{\text{mod}})\theta - \omega t - \delta\right] \\ & + h_m M_0 \wp_0 \cos(p_m\theta - p_{\text{m}}\omega_m t - p_{\text{m}}\zeta) \\ & + \frac{1}{2}h_m M_0 \wp_1 \cos\left[(p_m - p_{\text{mod}})\theta - p_{\text{m}}\omega_m t - p_{\text{m}}\zeta\right] \\ & + \frac{1}{2}h_m M_0 \wp_1 \cos\left[(p_m + p_{\text{mod}})\theta - p_{\text{m}}\omega_m t - p_{\text{m}}\zeta\right] \end{aligned} \tag{4.259}$$

$$
\begin{aligned}
H_\theta\big|_{r=R_o} = & -\frac{h_m}{\mu_0 R_o}\times \\
& \Big\{F_{s1}\wp_0 p_s\cos\big(p_s\theta-\omega t-\delta\big) \\
& +\frac{1}{2}F_{s1}\wp_1(p_s-p_{\mathrm{mod}})\cos\big[(p_s-p_{\mathrm{mod}})\theta-\omega t-\delta\big] \\
& +\frac{1}{2}F_{s1}\wp_1(p_s+p_{\mathrm{mod}})\cos\big[(p_s+p_{\mathrm{mod}})\theta-\omega t-\delta\big] \\
& -h_m M_0\wp_0 p_m\sin(p_m\theta-p_{\mathrm{m}}\omega_m t-p_{\mathrm{m}}\zeta) \\
& -\frac{1}{2}h_m M_0\wp_1(p_m-p_{\mathrm{mod}})\sin\big[(p_m-p_{\mathrm{mod}})\theta-p_{\mathrm{m}}\omega_m t-p_{\mathrm{m}}\zeta\big] \\
& -\frac{1}{2}h_m M_0\wp_1(p_m+p_{\mathrm{mod}})\sin\big[(p_m+p_{\mathrm{mod}})\theta-p_{\mathrm{m}}\omega_m t-p_{\mathrm{m}}\zeta\big]\Big\}
\end{aligned}
\tag{4.260}
$$

The shear stress on the PMs can be calculated as:

$$
\begin{aligned}
\tau_m &= \sigma_m(\theta,t)H_\theta(\theta,t) \\
&= M_0\frac{h_m}{R_o}\cos p_m(\theta-\omega_m t-\zeta) \\
&\quad\times\Big\{F_{s1}\wp_0 p_s\cos\big(p_s\theta-\omega t-\delta\big) \\
&\quad+\frac{1}{2}F_{s1}\wp_1(p_s-p_{\mathrm{mod}})\cos\big[(p_s-p_{\mathrm{mod}})\theta-\omega t-\delta\big] \\
&\quad+\frac{1}{2}F_{s1}\wp_1(p_s+p_{\mathrm{mod}})\cos\big[(p_s+p_{\mathrm{mod}})\theta-\omega t-\delta\big] \\
&\quad-h_m M_0\wp_0 p_m\sin(p_m\theta-p_{\mathrm{m}}\omega_m t-p_{\mathrm{m}}\zeta) \\
&\quad-\frac{1}{2}h_m M_0\wp_1(p_m-p_{\mathrm{mod}})\sin\big[(p_m-p_{\mathrm{mod}})\theta-p_{\mathrm{m}}\omega_m t-p_{\mathrm{m}}\zeta\big] \\
&\quad-\frac{1}{2}h_m M_0\wp_1(p_m+p_{\mathrm{mod}})\sin\big[(p_m+p_{\mathrm{mod}})\theta-p_{\mathrm{m}}\omega_m t-p_{\mathrm{m}}\zeta\big]\Big\}
\end{aligned}
\tag{4.261}
$$

The first, the forth, the fifth and the sixth terms of the tangential component of the field H_θ are orthogonal to the surface charge distribution, so the spatial average of their multiplication is zero, but the second and the third terms might be able to produce a shear

stress and contribute in the torque production if they meet *pole and speeds conditions*. Product of $\cos p_m(\theta-\omega_m t-\zeta)$ with the second term of H_θ will be:

$$\frac{1}{4}M_0\frac{h_m}{R_o}F_{s1}\wp_1(p_s-p_{\mathrm{mod}})\cos\left[(p_m-p_s+p_{\mathrm{mod}})\theta+(\omega-p_m\omega_m)t+\delta-p_m\zeta\right]$$
$$+\frac{1}{4}M_0\frac{h_m}{R_o}F_{s1}\wp_1(p_s-p_{\mathrm{mod}})\cos\left[(p_m+p_s-p_{\mathrm{mod}})\theta-(\omega+p_m\omega_m)t-\delta-p_m\zeta\right] \tag{4.262}$$

Meeting the pole condition $p_{mod}=p_s-p_m$ and the speed condition $\omega_m=\omega/p_{mod}$ for the first part, or meeting the pole condition $p_{mod}=p_s+p_m$ and the speed condition $\omega_m=-\omega/p_{mod}$ for the second part, it reduces to:

$$\pm\frac{1}{4}M_0\frac{h_m}{R_o}F_{s1}\wp_1 p_{\mathrm{mod}}\cos(\delta\mp p_{\mathrm{mod}}\zeta);\qquad \omega_m=\pm\frac{\omega}{p_{mod}} \tag{4.263}$$

Product of $\cos p_m(\theta-\omega_m t-\zeta)$ with the third term of H_θ will be:

$$\frac{1}{4}M_0\frac{h_m}{R_o}F_{s1}\wp_1(p_s+p_{\mathrm{mod}})\cos\left[(p_m-p_s-p_{\mathrm{mod}})\theta+(\omega-p_m\omega_m)t+\delta-p_m\zeta\right]$$
$$+\frac{1}{4}M_0\frac{h_m}{R_o}F_{s1}\wp_1(p_s+p_{\mathrm{mod}})\cos\left[(p_m+p_s+p_{\mathrm{mod}})\theta-(\omega+p_m\omega_m)t-\delta-p_m\zeta\right] \tag{4.264}$$

Meeting the pole condition $p_{mod}=p_m-p_s$ and the speed condition $\omega_m=\omega/p_{mod}$ for the first part, or meeting the pole condition $p_{mod}=-(p_s+p_m)$ and the speed condition $\omega_m=-\omega/p_{mod}$ for the second part, it reduces to:

$$\pm\frac{1}{4}M_0\frac{h_m}{R_o}F_{s1}\wp_1 p_{\mathrm{m}}\cos(\delta\mp p_m\zeta);\qquad \omega_m=\pm\frac{\omega}{p_{mod}} \tag{4.265}$$

Finally, the shear stress will be as in below:

$$\tau_m=\pm\frac{1}{4}M_0\frac{h_m}{R_o}F_{s1}\wp_1 p_{\mathrm{m}}\cos(\delta\mp p_m\zeta);\quad \omega_m=\pm\frac{\omega}{p_{mod}} \tag{4.266}$$

There are two cases out of the two parts of the second term of the tangential field, that results in the following shear stress expression:

$$\tau_m = \pm\frac{1}{4} M_0 \frac{h_m}{R_o} F_{s1} \wp_1 p_{\mathrm{m}} \cos(\delta \mp p_m \zeta); \quad \omega_m = \pm\frac{\omega}{p_{mod}} \tag{4.267}$$

Developed torque:

The following values will be substituted in the shear stress expression:

$$F_{s1} = -\frac{3}{2}\frac{4}{\pi}\frac{NI_s}{2p_s} k_w \quad ; M_0 = \frac{4}{\pi}\frac{B_r}{\mu_0}\sin\frac{p_m\theta_m}{2} \tag{4.268}$$

The developed electromagnetic torque can be calculated using the shear stress on the surface of PMs as in below:

$$T^e{}_{PM} = 2\pi R_o{}^2 L < \tau_m > \tag{4.269}$$

By substituting $<\tau_s>$, M_0 and F_{s1}, we obtain:

$$T^e{}_{PM} = \mp\frac{3}{2}\frac{4}{\pi}\frac{p_{\mathrm{m}}}{p_s}\frac{B_r}{\mu_0} R_o L k_w N I_s h_m \wp_1 \sin\frac{p_m\theta_m}{2}\cos(\delta \mp p_m\zeta); \quad \omega_m = \pm\frac{\omega}{p_{mod}} \tag{4.270}$$

4.9.2 Torque on PM rotor using Lorentz force and Amperian current model of PMs

The permanent magnets can also be represented by Amperian currents as in below:

$$J_m(r,\theta,t) = \frac{M_0 p_m}{r}\sin p_m(\theta - \omega_m t - \zeta) \tag{4.271}$$

The developed torque can be calculated using the following surface integral over the area S as in the following:

$$
\begin{aligned}
T^{e}{}_{PM} &= L\int_{0}^{2\pi}\int_{R_o}^{R_o+h_m} r\,J_m(r,\theta,t)\,B_r(\theta,t)\,r\,dr\,d\theta \\
&= L\int_{0}^{2\pi}\int_{R_o}^{R_o+h_m} r\left(\frac{M_0 p_m}{r}\sin\,p_m(\theta-\omega_m t-\zeta)\right)B_r(\theta,t)\,r\,dr\,d\theta \\
&= LM_0 p_m\int_{R_o}^{R_o+h_m} r\,dr\int_{0}^{2\pi}\sin\,p_m(\theta-\omega_m t-\zeta)\,B_r(\theta,t)\,d\theta \\
&= \frac{1}{2}LM_0 p_m(2R_o h_m+h_m{}^2)\int_{0}^{2\pi}\sin\,p_m(\theta-\omega_m t-\zeta)\,B_r(\theta,t)\,d\theta
\end{aligned}
\tag{4.272}
$$

The term inside the integral can be written as:

$$
\begin{aligned}
\sin\,p_m(\theta-\omega_m t-\zeta)\,B_r(\theta,t)\,d\theta = \sin\,p_m(\theta-\omega_m t-\zeta)\times \\
&\Big\{F_{s1}\wp_0\sin\big(p_s\theta-\omega t-\delta\big) \\
&+\frac{1}{2}F_{s1}\wp_1\sin\big[(p_s-p_{\mathrm{mod}})\theta-\omega t-\delta\big] \\
&+\frac{1}{2}F_{s1}\wp_1\sin\big[(p_s+p_{\mathrm{mod}})\theta-\omega t-\delta\big] \\
&+h_m M_0\wp_0\cos(p_m\theta-p_{\mathrm{m}}\omega_m t-p_{\mathrm{m}}\zeta) \\
&+\frac{1}{2}h_m M_0\wp_1\cos\big[(p_m-p_{\mathrm{mod}})\theta-p_{\mathrm{m}}\omega_m t-p_{\mathrm{m}}\zeta\big] \\
&+\frac{1}{2}h_m M_0\wp_1\cos\big[(p_m+p_{\mathrm{mod}})\theta-p_{\mathrm{m}}\omega_m t-p_{\mathrm{m}}\zeta\big]\Big\}
\end{aligned}
\tag{4.273}
$$

Spatial average of the product of $\sin\,p_m(\theta-\omega_m t-\zeta)$ with the first, the forth, the fifth and the sixth terms is zero because they are orthogonal, but the second and the third terms of B_r might be able to produce a torque. Product with the second term of B_r will be:

$$
\begin{aligned}
&\frac{1}{4}F_{s1}\wp_1\cos\big[(p_m-p_s+p_{\mathrm{mod}})\theta+(\omega-p_{\mathrm{m}}\omega_m)t+\delta-p_{\mathrm{m}}\zeta\big] \\
&-\frac{1}{4}F_{s1}\wp_1\cos\big[(p_m+p_s-p_{\mathrm{mod}})\theta-(\omega+p_{\mathrm{m}}\omega_m)t-\delta-p_{\mathrm{m}}\zeta\big]
\end{aligned}
\tag{4.274}
$$

Meeting the pole condition $p_{mod}=p_s-p_m$ and the speed condition $\omega_m=\omega/p_m$ for the first part, or meeting the pole condition $p_{mod}=p_s+p_m$ and the speed condition $\omega_m=-\omega/p_{mod}$ for the second part, it reduces to:

$$\pm\frac{1}{4}F_{s1}\wp_1\cos(\delta\mp p_{\mathrm{mod}}\zeta) \tag{4.275}$$

Product with the third term of B_r will be:

$$\begin{aligned}&\frac{1}{4}F_{s1}\wp_1\cos\left[(p_m-p_s-p_{\mathrm{mod}})\theta+(\omega-p_{\mathrm{m}}\omega_m)t+\delta-p_{\mathrm{m}}\zeta\right]\\&-\frac{1}{4}F_{s1}\wp_1\cos\left[(p_m+p_s+p_{\mathrm{mod}})\theta-(\omega+p_{\mathrm{m}}\omega_m)t-\delta-p_{\mathrm{m}}\zeta\right]\end{aligned} \tag{4.276}$$

Meeting the pole condition $p_{mod}=p_m-p_s$ and the speed condition $\omega_m=\omega/p_m$ for the first part, or meeting the pole condition $p_{mod}=-(p_s+p_m)$ and the speed condition $\omega_m=-\omega/p_m$ for the second part, it reduces to:

$$\pm\frac{1}{4}F_{s1}\wp_1\cos(\delta\mp p_{\mathrm{mod}}\zeta) \tag{4.277}$$

Substitution of the two terms in the torque equation gives the following:

$$T^e{}_{PM}=\pm\frac{\pi}{4}LM_0p_mF_{s1}\wp_1(2R_oh_m+h_m{}^2)\cos(\delta\mp p_{\mathrm{mod}}\zeta);\quad \omega_m=\pm\frac{\omega}{p_{mod}} \tag{4.278}$$

Taking the second part of the product with the second term and first part of the product with the third term, and substitution of F_{s1} and M_0 results in the following equation:

$$T^e{}_{PM}=\mp\frac{3}{4}\frac{4}{\pi}\frac{p_m}{p_s}\frac{B_r}{\mu_0}\frac{1}{2}(2R_oh_m+h_m{}^2)L\ k_wN\ I_s\wp_1\sin\frac{p_m\theta_m}{2}\cos(\delta\mp p_{\mathrm{mod}}\zeta);\quad \omega_m=\pm\frac{\omega}{p_{mod}} \tag{4.279}$$

For relatively large machines, we have:

$$R_o\gg h_m\ \Rightarrow\ 2R_oh_m+h_m{}^2\approx 2R_oh_m \tag{4.280}$$

Then, the developed torque can be calculated as in below:

$$T^e_{PM} = \mp\frac{3}{2}\frac{4}{\pi}\frac{p_m}{p_s}\frac{B_r}{\mu_0}R_o L k_w N I_s h_m \wp_1 \sin\frac{p_m\theta_m}{2}\cos(\delta \mp p_{\text{mod}}\zeta) \;\; ; \;\; \omega_m = \pm\frac{\omega}{p_{mod}} \tag{4.281}$$

It is seen that the value obtained from this method is the same as the previous method if $R_o >> h_m$.

Defining the torque angle as in below:

$$\beta = \delta \mp p_{\text{mod}}\zeta \tag{4.282}$$

we have:

$$T^e_{PM} = \mp\frac{3}{2}\frac{4}{\pi}\frac{p_m}{p_s}\frac{B_r}{\mu_0}R_o L k_w N I_s h_m \wp_1 \sin\frac{p_m\theta_m}{2}\sin\beta \;\; ; \;\; \omega_m = \pm\frac{\omega}{p_{mod}} \tag{4.283}$$

Torque angle characteristics of the machine is shown in Fig. 4.43.

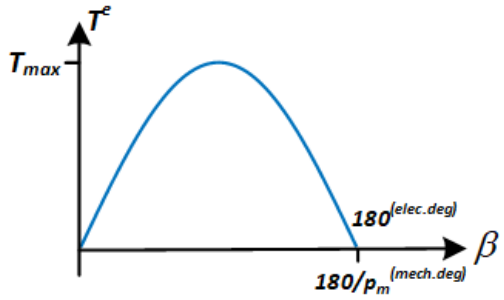

Figure 4.43: Torque angle characteristics for a geared machine with rotating PM ring

4.9.3 Torque on stator

The torque on the stator can obtained using Maxwell stress tensor or Lorenz force. The shear stress on the stator can be obtained using Maxwell stress tensor as in below:

$$
\begin{aligned}
\tau_s = T_{\theta r} &= H_\theta B_r \\
&= H_{\theta 1}\cos\left(p_s\theta-\omega t-\delta\right)\times \\
&\quad \left\{F_{s1}\wp_0\sin\left(p_s\theta-\omega t-\delta\right)\right. \\
&\quad +\frac{1}{2}F_{s1}\wp_1\sin\left[(p_s-p_{\mathrm{mod}})\theta-\omega t-\delta\right] \\
&\quad +\frac{1}{2}F_{s1}\wp_1\sin\left[(p_s+p_{\mathrm{mod}})\theta-\omega t-\delta\right] \\
&\quad +h_m M_0\wp_0\cos(p_m\theta-p_{\mathrm{m}}\omega_m t-p_{\mathrm{m}}\zeta) \\
&\quad +\frac{1}{2}h_m M_0\wp_1\cos\left[(p_m-p_{\mathrm{mod}})\theta-p_{\mathrm{m}}\omega_m t-p_{\mathrm{m}}\zeta\right] \\
&\quad \left.+\frac{1}{2}h_m M_0\wp_1\cos\left[(p_m+p_{\mathrm{mod}})\theta-p_{\mathrm{m}}\omega_m t-p_{\mathrm{m}}\zeta\right]\right\}
\end{aligned}
\tag{4.284}
$$

The first, the second, the third and the fourth terms of the radial field are orthogonal to the tangential filed, so the spatial average of their product is zero, but the fifth and the sixth terms might be able to produce a shear stress and contribute in the torque production if they meet *pole and speeds conditions*. Product of with the fifth term of B_r will be:

$$
\begin{aligned}
&\frac{1}{4}h_m M_0\wp_1 H_{\theta 1}\cos\left[(p_s-p_m+p_{\mathrm{mod}})\theta-(\omega-p_{\mathrm{m}}\omega_m)t-\delta+p_{\mathrm{m}}\zeta\right] \\
&+\frac{1}{4}h_m M_0\wp_1 H_{\theta 1}\cos\left[(p_s+p_m-p_{\mathrm{mod}})\theta-(\omega+p_{\mathrm{m}}\omega_m)t-\delta-p_{\mathrm{m}}\zeta\right]
\end{aligned}
\tag{4.285}
$$

Meeting the pole condition $p_{mod}=p_m-p_s$ and the speed condition $\omega_m=\omega/p_{mod}$ for the first part, or meeting the pole condition $p_{mod}=p_s+p_m$ and the speed condition $\omega_m=-\omega/p_{mod}$ for the second part, it reduces to:

$$
\frac{1}{4}h_m M_0\wp_1 H_{\theta 1}\cos(\delta\mp p_{\mathrm{mod}}\zeta);\qquad \omega_m=\pm\frac{\omega}{p_{mod}}
\tag{4.286}
$$

Product of with the sixth term of B_r will be:

$$
\begin{aligned}
&\frac{1}{4}h_m M_0\wp_1 H_{\theta 1}\cos\left[(p_s-p_m-p_{\mathrm{mod}})\theta-(\omega-p_{\mathrm{m}}\omega_m)t-\delta+p_{\mathrm{m}}\zeta\right] \\
&+\frac{1}{4}h_m M_0\wp_1 H_{\theta 1}\cos\left[(p_s+p_m+p_{\mathrm{mod}})\theta-(\omega+p_{\mathrm{m}}\omega_m)t-\delta-p_{\mathrm{m}}\zeta\right]
\end{aligned}
\tag{4.287}
$$

Meeting the pole condition $p_{mod}=p_s-p_m$ and the speed condition $\omega_m=\omega/p_{mod}$ for the first part, or meeting the pole condition $p_{mod}=-(p_s+p_m)$ and the speed condition $\omega_m=-\omega/p_{mod}$ for the second part, it reduces to:

$$\frac{1}{4}h_m M_0 \wp_1 H_{\theta 1}\cos(\delta \mp p_{\mathrm{mod}}\zeta); \qquad \omega_m = \pm\frac{\omega}{p_{mod}} \tag{4.288}$$

Taking the first and the second parts of the fifth term, shear stress expression is as in the following:

$$\tau_s = \frac{1}{4}h_m M_0 \wp_1 H_{\theta 1}\cos(\delta \mp p_m\zeta); \quad \omega_m = \pm\frac{\omega}{p_{mod}} \tag{4.289}$$

Having a minus sign for the stator node assumed to be an input, there developed torque will be:

$$T^e{}_{stator} = -\frac{3}{2}\frac{4}{\pi}\frac{B_r}{\mu_0}R_i L k_w N I_s h_m \wp_1 \sin\frac{p_m\theta_m}{2}\cos(\delta \mp p_m\zeta); \quad \omega_m = \pm\frac{\omega}{p_{mod}} \tag{4.290}$$

In terms of the torque angle β, we have:

$$T^e{}_{stator} = -\frac{3}{2}\frac{4}{\pi}\frac{B_r}{\mu_0}R_i L k_w N I_s h_m \wp_1 \sin\frac{p_m\theta_m}{2}\sin\beta; \quad \omega_m = \pm\frac{\omega}{p_{mod}} \tag{4.291}$$

4.9.4 Gearing effect

The gearing ratio, defined as ratio of the torque on the rotor (PM ring) to the torque on the stator, can be calculated as in below:

$$\frac{T_{pm}}{T_{stator}} = \pm\frac{p_m}{p_s} \tag{4.292}$$

Defining the speed ratio as the ratio of the rotating field of the stator to the mechanical speed of the rotor (PM ring), we have:

$$\frac{\Omega_{\mathrm{m}}}{\Omega_{\mathrm{s}}} = \frac{\pm\omega/\,p_{\mathrm{m}}}{\omega/\,p_s} = \pm\frac{p_s}{p_{\mathrm{m}}} \tag{4.293}$$

If $p_m > p_s$, we will end in a geared machine having lower speed and a higher torque.

4.9.5 Power balance

The power into the machine (in motoring case) is the developed electromagnetic torque of the stator times the velocity of the stator rotating filed as in below:

$$P_s = T^e{}_{stator}\,\Omega_s = T_s\frac{\omega}{p_s} = \frac{\omega}{p_s}\times -\frac{3}{2}\frac{4}{\pi}\frac{B_r}{\mu_0}R_i L\,k_w N I_s h_m \delta \wp_1 \sin\frac{p_m\theta_m}{2}\sin\beta \tag{4.294}$$

It is worth noting that negative electrical power refers to the stator as an input port — motoring mode, while a positive electrical power refers to an output port—generating mode.

The mechanical power is the total torque at the rotor (modulator ring) times the mechanical speed of the machine as in below

$$\begin{aligned} P_{mech} &= P_{\mathrm{m}} = T^e\,\Omega_{\mathrm{m}} = T^e\frac{\omega}{p_{\mathrm{m}}} \\ &= \pm\frac{\omega}{p_{\mathrm{m}}}\times\mp\frac{3}{2}\frac{4}{\pi}\frac{p_{\mathrm{m}}}{p_s}\frac{B_r}{\mu_0}R_o L k_w N I_s h_m \delta \wp_1 \sin\frac{p_m\theta_m}{2}\sin\beta \\ &= -\frac{\omega}{p_s}\times\frac{3}{2}\frac{4}{\pi}\frac{B_r}{\mu_0}R_o L k_w N I_s h_m \delta \wp_1 \sin\frac{p_m\theta_m}{2}\sin\beta \end{aligned} \tag{4.295}$$

The power balance can be observed.

Chapter 5

Model Validation and 2D FEA of a Radial-Flux Magnetically-Geared Machine

5.1 Introduction

In this chapter, an inside-out radial-flux magnetically-geared machine is analyzed using two dimensional finite element analysis (FEA). The analytical framework in the chapter 4 is also investigated and validated for the two cases of rotating modulators and rotating PMs. The gearing effect and harmonics analysis is performed using FFT. The meshed model is presented. The main characteristics of the machine such as torque-angle curve, torque profile, back EMF, magnetic flux density distribution and flux lines are extracted and studied as well.

5.2 Machine geometry and specifications

Fig. 5.1 shows the machine geometry having an inside-out (inner stator) configuration. Its specifications are given in Table 5.1. The three phase stator has a frequency of *50 Hz*, four poles ($p_s=2$), single layer winding, and 36 slots, i.e. three slots per pole per phase. There are 22 PMs ($p_m=11$) on the outer back iron, so there will be 2+11=13 modulator pieces. The number of turns per coil (number of turns in a slot) is 30, so the total number of turns in each phase winding will be 180. Two cases will be investigated: rotating modulator ring, and rotating PM ring. Slot dimensions are also given in Fig. 5.2 and Table 5.2.

Table. 5.1: Geometric parameters of the machine.

Parameter	Symbol	value
inner air-gap	g_i	*1 mm*
outer air-gap	g_o	*1 mm*
modulator height	h_{mod}	*6 mm*
permanent magnet height	h_m	*5 mm*
PM pole ratio	α_m	*0.9*
PM arc	$\theta_m = \alpha_m(2\pi/p_m)$	*14.72 deg*
PM residual flux	B_r	*1.15 tesla*
stator pole pairs	P_s	*2*
PM pole pairs	P_m	*11*
number of modulators	P_{mod}	*13*
outer radius of stator	R_i	*50 mm*
axial length	L	*50 mm*
shaft diameter	D_{sh}	*10 mm*
outer yoke thickness	L_{yo}	*6 mm*
number of stator slot	n_s	*36*
total number of turns per phase winding	N	*180*
electrical frequency of stator	f	*50 Hz*
mechanical speed of modulator rotor		*230.78 rpm*
mechanical speed of PM rotor		*272.73 rpm*

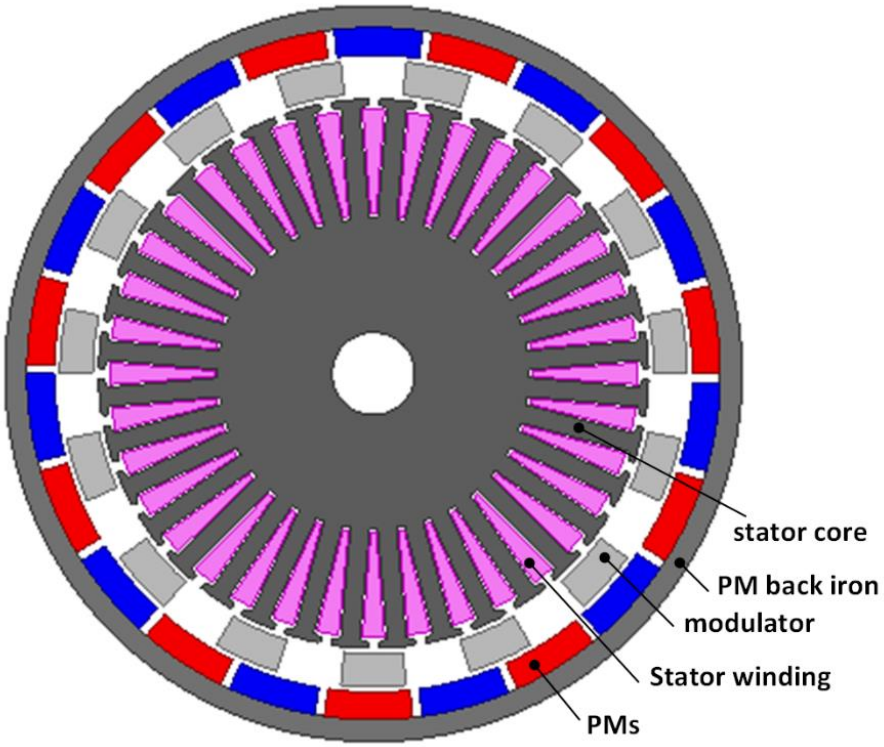

Figure 5.1: A typical inside-out radial-flux magnetically-geared machine.

Table. 5.2: Slot dimensions.

Slot dimensions	value
h_{s0}	*1 mm*
h_{s1}	*0.7 mm*
h_{s2}	*20 mm*
b_{s0}	*2 mm*
b_{s1}	*5 mm*
b_{s2}	*1.5 mm*

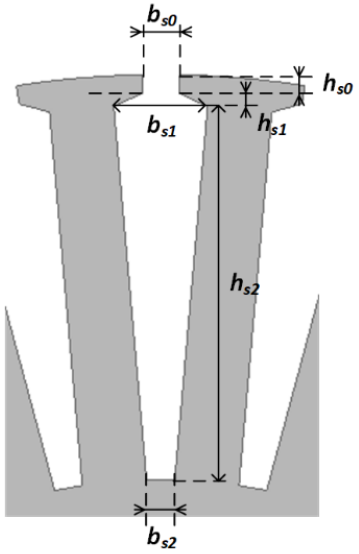

Figure 5.2: Slot dimensions.

5.3 Machine with rotating modulators

In this section, the machine with rotating modulators will be analyzed. Field distribution, gearing effect, back EMF and torque characteristics will also be extracted and studied. At the stator frequency of 50 Hz, the mechanical speed of the PM rotor in *rpm* is:

$$\frac{2\pi f}{p_{\text{mod}}} \times \frac{30}{\pi} = \frac{2\pi 50}{13} \times \frac{30}{\pi} = 230.77 \ rpm \tag{5.1}$$

5.3.1 Field analysis

Fig. 5.3 shows the meshed model of the machine using two-dimensional finite element analysis in the software *Ansoft Maxwell*. It can be seen that smaller elements are used in

areas having more field variation, e.g. the air-gap, inter-modulator regions and PMs, while in the iron parts relatively larger elements are employed to reduce the simulation time. There are around 50000 elements in this meshed model that is used in the preliminary investigations. Fig. 5.4 illustrates a very fine meshed model for final analysis and result extraction. It includes around 90000 elements.

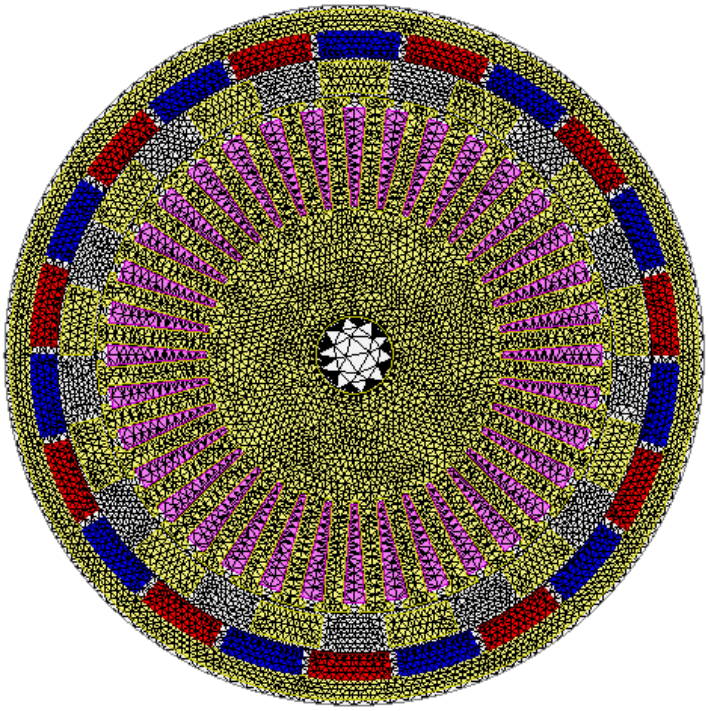

Figure 5.3: A middle-level meshed model for the analyses.

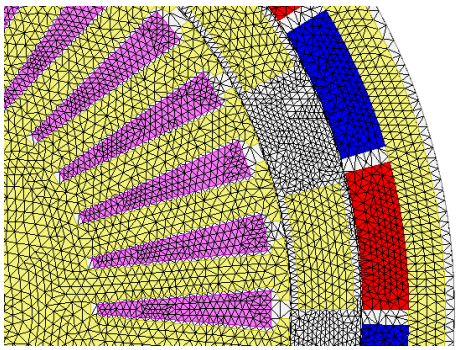

Figure 5.4: A very fine meshed model.

Fig. 5.5 shows the flux lines within the machines for current loading of 21 Ampere-turns in each slot. It can be seen that the stator has four poles ($p_s=2$). Flux lines on the PM side behave the way that we expected. The interesting point is the effect of modulators on

the fluxed produced by the stator current and residual flux of PMs. Detailed study and harmonics analysis of this influence is performed in the next sections. Fig. 5.6 shows the magnetic flux density distribution within the machines that could somehow be predicted from the flux lines.

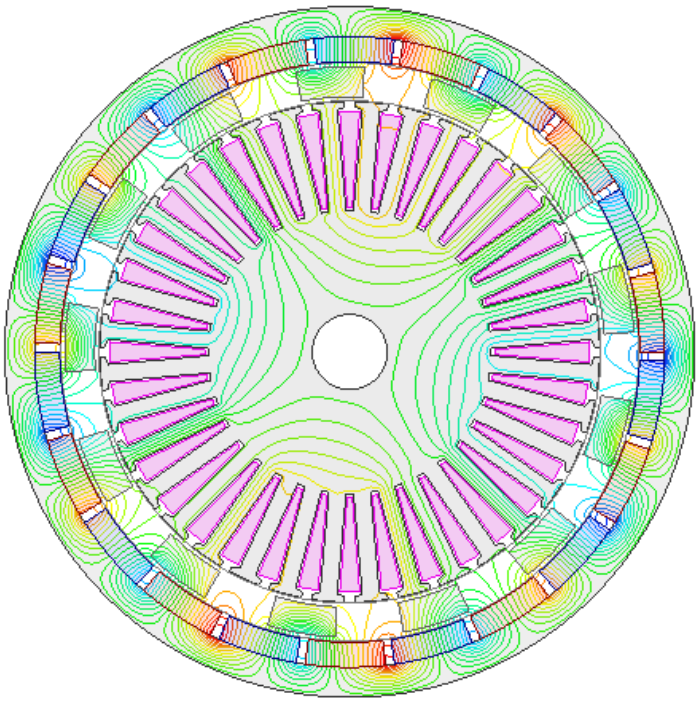

Figure 5.5: Flux lines within the machine.

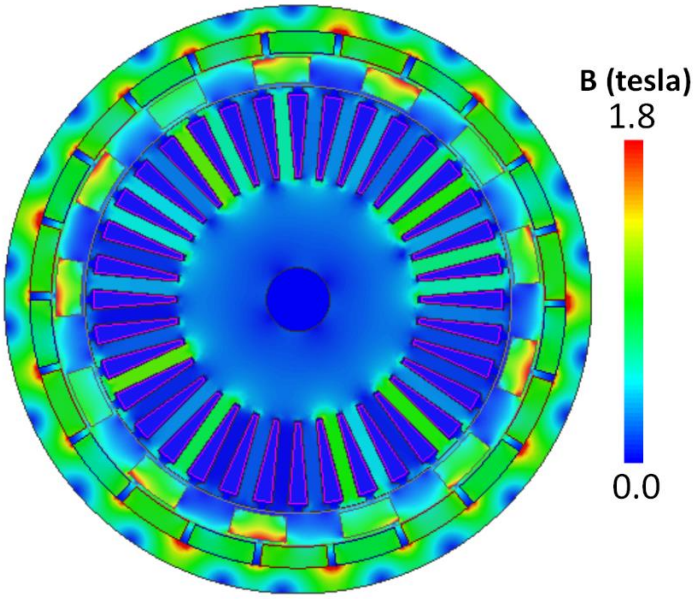

Figure 5.6: Magnetic flux density distribution within the machine.

5.3.2 Field analysis of the gearing effect

Fig. 5.7 illustrates the radial component of the magnetic flux density distribution on the two air-gaps of Fig. 5.6. The main harmonic (number of pole pairs of the MMF on that side) as well as the effect of modulator ring can be observed.

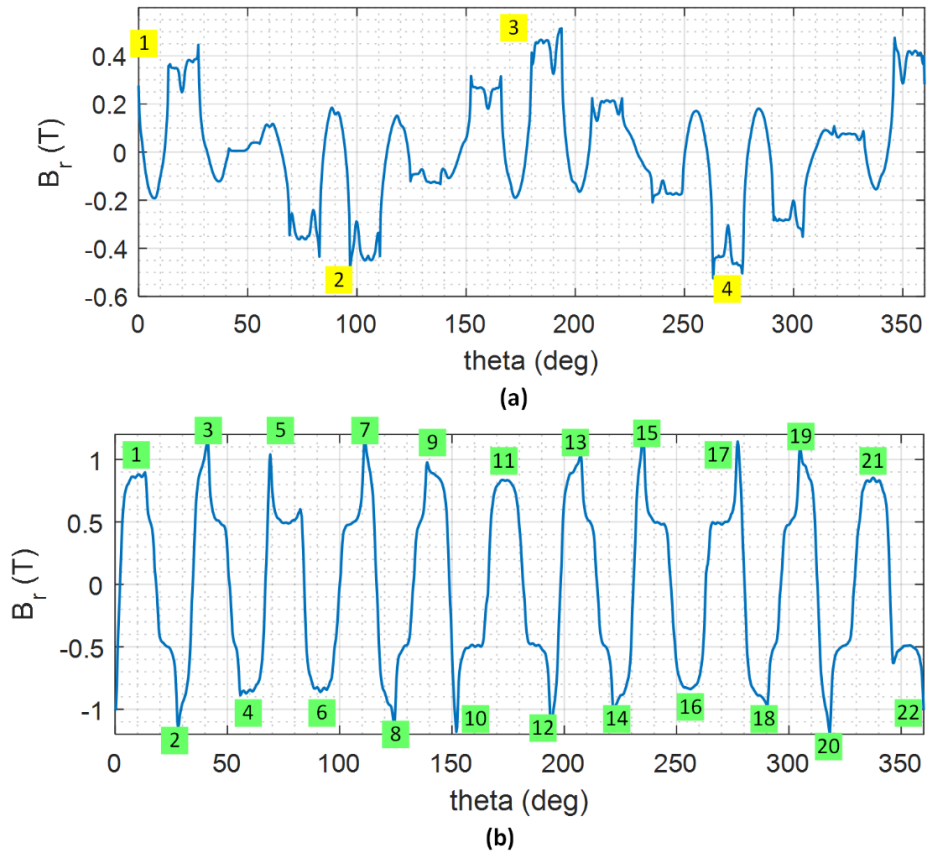

Figure 5.7: Radial component of magnetic flux density distribution in (a) stator-side air-gap having four poles (p_s=*2*) and (b) PM-side air-gap having 22 poles (p_m=*11*).

Fig. 5.8 illustrates the harmonics (pole pair) analysis of the radial component of the magnetic flux density distribution of the two air-gaps using FFT. In each air-gap, there are two sources of harmonics: the MMF on that side and the modulated form of the field on the other side. As we discussed in chapter 4, one part of the gearing idea is to match the number of pole pairs of the stator with one of the harmonics produced by modulation of the field generated by the PMs. Considering the first pair ($p_{mod}\pm p_m$), the two harmonics of 2 and 24 can be seen on the stator side as shown in Fig. 5.8(a). The number of pole pair of

the stator field matches with the first one (2)., because the first one has a higher magnitude, so it will be the best candidate for pole matching. Another reason for taking this option is that a higher number of modulator pieces means that the width of the modulators is smaller which allows flor less flux leakage. The third reason is that the torques produced on the two sides of the modulator ring will add, as we discussed in chapter 4. The second part of the gearing idea is to match the number of pole pairs of the PMs with one of the harmonics produced by modulation of the field generated by the stator. Considering the first pair ($p_{mod} \pm p_s$), the two harmonics of 11 and 15 can be seen on the PM side as shown in Fig. 5.8(b). The number of pole pair of the PM field matches with the first one (11).

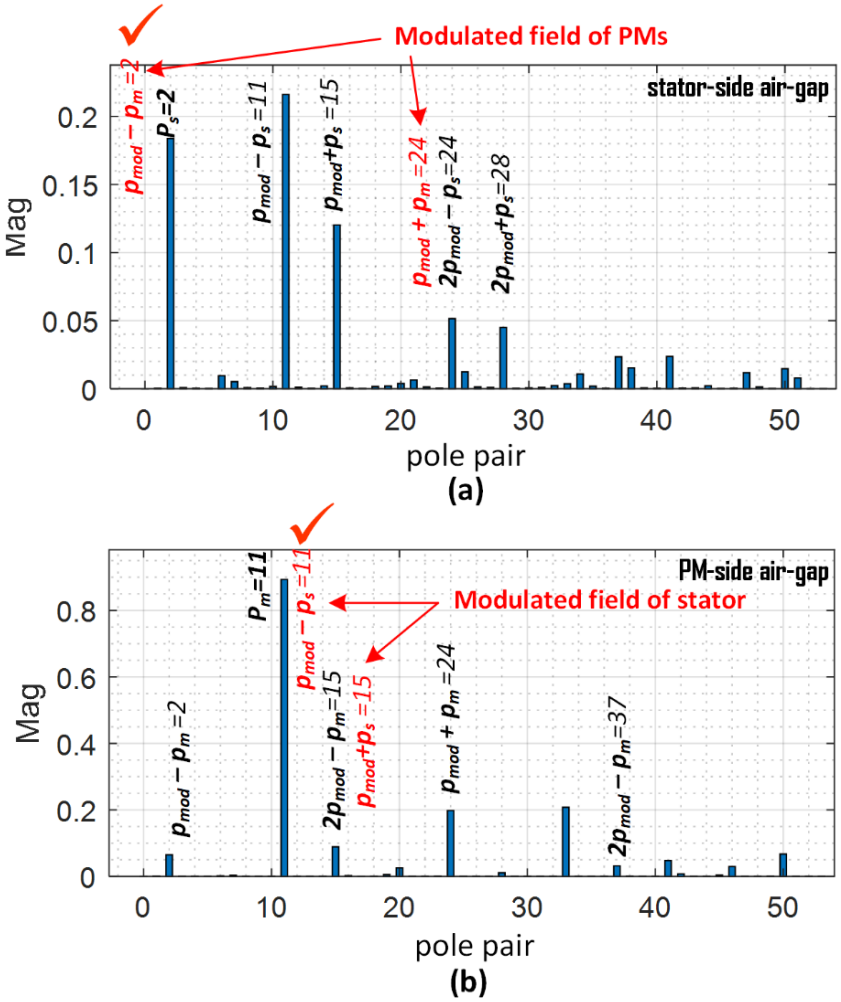

Figure 5.8: Space harmonic spectrum (pole pair of the field components) in (a) the stator-side air-gap and (b) PM-side air-gap.

5.3.3 Torque and back-EMF

Torque angle characteristics of the machine for current loading of 63 Ampere-turns is as in Fig. 5.9 which is almost a sinusoidal curve. To obtain this characteristics, the stator windings are excited with DC values which can be *amplitude* of the three phase currents at an arbitrary time, e.g. set of (I_s,-I_s/2,-I_s/2), then the rotor is rotated with a constant speed to get the torque-angle curve, e.g. if the speed is 1 deg/sec, a curve as a function of mechanical angular displacement of the rotor will be obtained.

A half period of the curve is 180 electrical degrees as well as $180/p_{mod}$ mechanical degrees of the rotor angular displacement, as we expected from $\beta=\delta\pm p_{mod}\zeta$ in section 4.8. The result of the analytical model is compared with that obtained from FEM. A close agreement between the flux-tube based models and FEM can be observed. It is seen that the model whose torque is obtained using Amperian current representation of PMs and Lorenz force is more accurate than the one whose torque is extracted by Maxwell stress tensor or fictitious charge model. Torque profile for the torque angle of 39.5 electrical degrees is also given in Fig. 5.10.

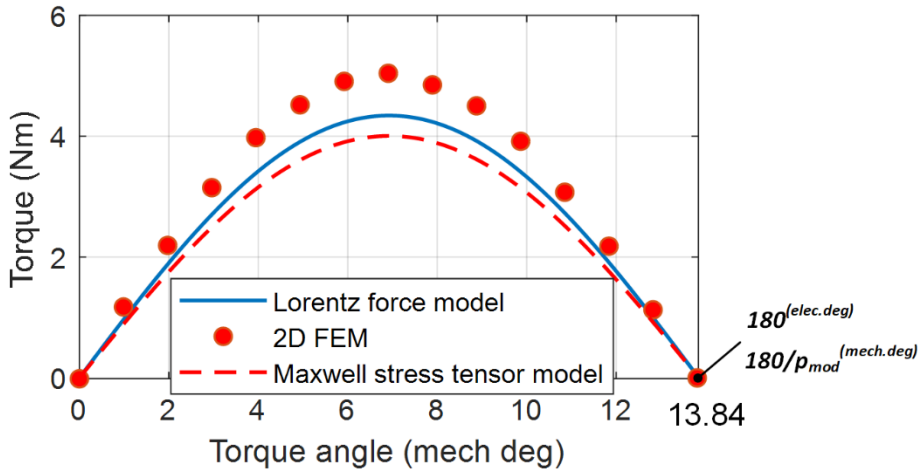

Figure 5.9: Torque angle characteristics

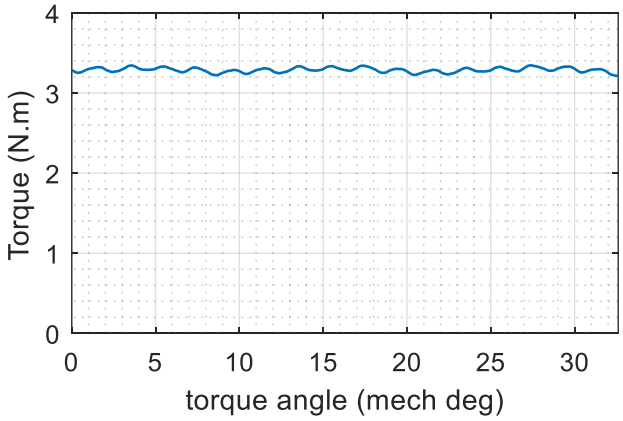

Figure 5.10: Torque profile at synchronous speed of 230.78 rpm and torque angle of 39.5 electrical degrees (3.04 mechanical degrees)

Fig. 5.11 presents the back-EMF waveforms with electrical frequency of *50 Hz* while the rotor (modulator ring) is rotating at speed of *230.78 rpm*. The waveforms are almost sinusoidal as its FFT is shown in Fig. 12.

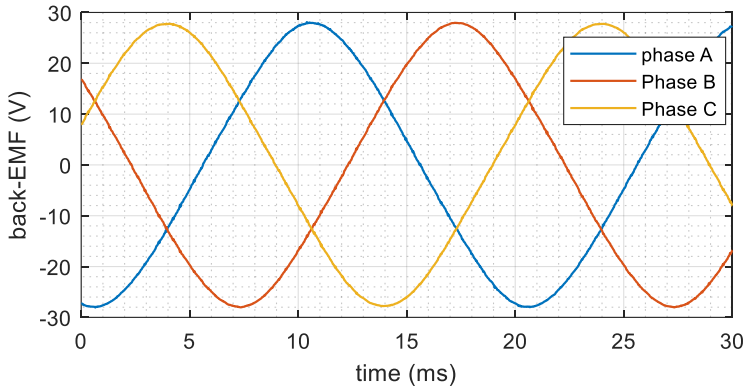

Figure 5.11: Back-EMF waveforms with frequency 50 Hz at rotor mechanical speed of $2\pi f/p_{mod}$ =230.78 rpm.

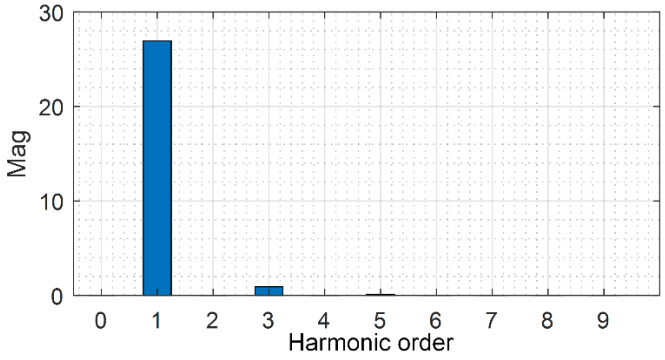

Figure 5.12: Harmonic analysis of the back-EMF waveform

5.4 Machine with rotating PMs

In this section, the machine with rotating PMs will be analyzed. Field distribution, gearing effect, back EMF and torque characteristics will also be extracted and studied. At the stator frequency of 50 Hz, the mechanical speed of the PM rotor in *rpm* is:

$$\frac{2\pi f}{p_m}\times\frac{30}{\pi}=\frac{2\pi 50}{11}\times\frac{30}{\pi}=272.72\ rpm \tag{5.2}$$

5.4.1 Field analysis

Fig. 5.13 shows the flux lines within the machines for current loading of 63 Ampere-turns in each slot. It can be seen that the stator has four poles (p_s=*2*). Flux lines on the PM side behave the way that we expected. Fig. 5.14 shows the magnetic flux density distribution within the machines that could somehow be predicted from the flux lines.

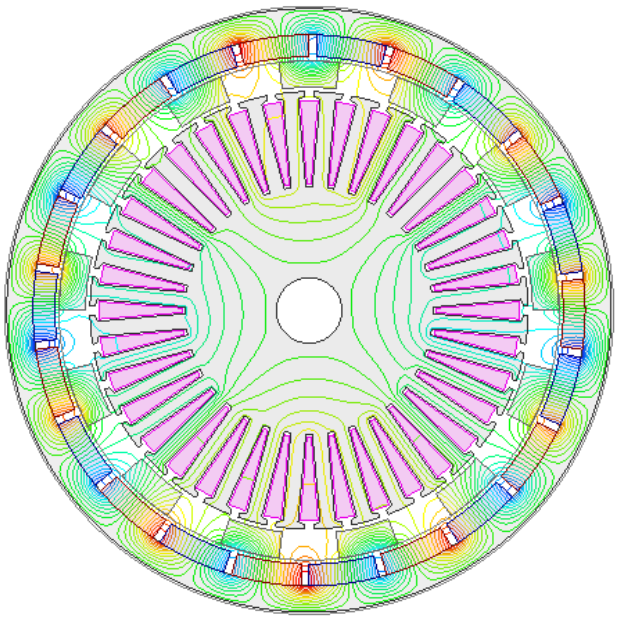

Figure 5.13: Flux lines in the machine.

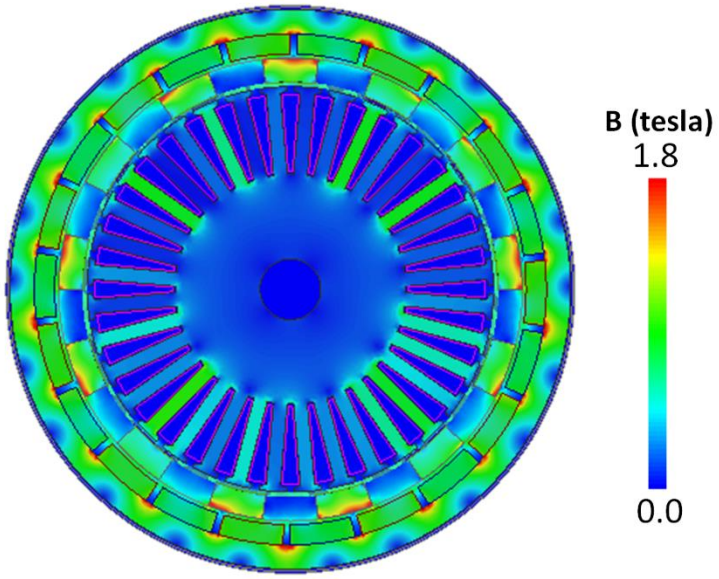

Figure 5.14: Magnetic flux density distribution within the machine.

5.4.2 Torque and back-EMF

Torque angle characteristics of the machine for current loading of 63 Ampere-turns is as in Fig. 5.15 which is almost a sinusoidal curve. The half period is 180 electrical degrees or $180/p_m$ mechanical degrees of the rotor angular displacement, as we expected from $\beta=\delta\pm p_m\zeta$ in section 4.9. Similar to the previous case, a close agreement between the flux-tube based model and FEM is obtained; actually, the Lorentz force based model is more accurate than the one based on Maxwell stress tensor Fig. 5.16 presents the back-EMF waveforms with frequency of *50 Hz* while the rotor (PM ring) is rotating at speed of *272.73 rpm*. The waveforms are almost sinusoidal as its FFT is shown in Fig. 17.

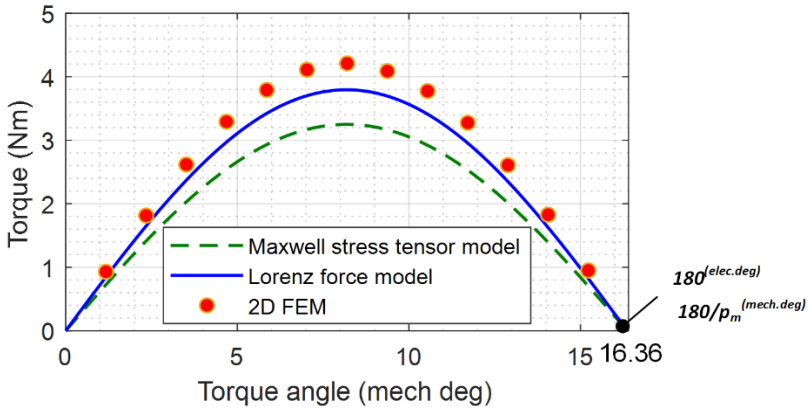

Figure 5.15: Torque angle characteristics

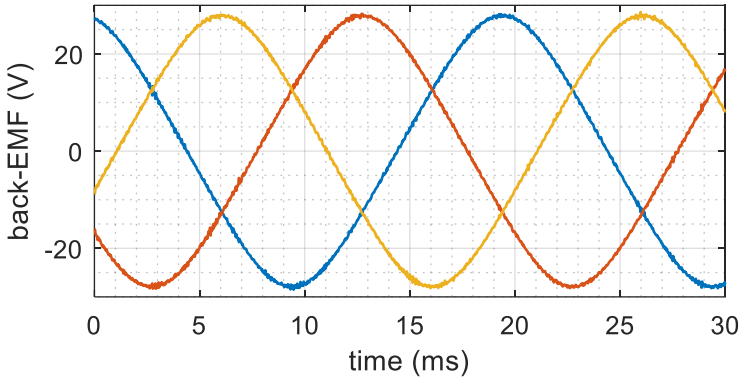

Figure 5.16: Back-EMF waveforms with frequency *50 Hz* at rotor mechanical speed of $2\pi f/p_m$ *=272.73 rpm*.

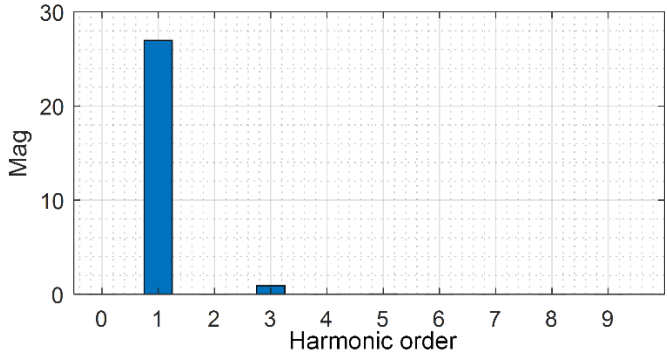

Figure 5.17: Harmonic analysis of the back-EMF waveform

5.5 Torque and back-EMF analysis of the gearing effect

As expected from the analytical framework in the chapter 4, it is seen that, at the same stator frequencies, the maximum torque in the case of rotating PM ring is smaller than the case of rotating modulator ring, while its mechanical speed at synchronous condition is higher; the reason is that the gearing ratio in the case of rotating modulators ($1+p_m/p_s$) is larger than the gearing ratio for the case of the rotating PM ring (p_m/p_s) which is also reflected in the closed form of the torque expressions in the two cases, as we obtained. It can also be observed that although the speeds the rotor in the two cases of rotating PM ring and rotating modulator ring are different, the frequency of the back-EMF is always the same—gearing effect.

Chapter 6

3D FEA of an Axial-Flux Magnetically Geared Machine

6.1 Introduction

In this chapter, a single-sided axial-flux magnetically-geared machine is analyzed using finite element analysis. Three-dimensional FEM is employed in the work. Machine characteristics are also extracted and analyzed. The whole idea of machine operation that we obtained using the analytical framework is confirmed by the simulations performed in this chapter.

6.2 Machine geometry and specifications

Fig. 6.1 shows the machine configuration which called axial-flux or disc-type machine. Concentrated windings are used here. Each coil, which is wound over one stator pole, has 110 turns. Each phase has four coils in series, so it has 440 turns. The specifications of the machine are given in Table 6.1.

The three phase stator has a frequency of *50 Hz*, eight poles ($p_s=4$). There are 22 PMs ($p_m=11$) on the outer back iron, so there will be 4+11=15 modulator pieces. Two cases will be investigated: rotating modulator ring, and rotating PM ring. Slot dimensions are also given in Fig. 5.2 and Table 5.2. Fig. 6.2 depicts the exploded view of the machine in which the configuration is more visible.

Table. 6.1: Geometric parameters of the machine.

Parameter	Symbol	value
Stator-side air-gap	g_1	*1 mm*
Rotor-side air-gap	g_2	*1 mm*
modulator height	h_{mod}	*3 mm*
permanent magnet height	h_m	*5 mm*
PM pole ratio	α_m	*0.9*
PM arc	$\theta_m = \alpha_m(2\pi/p_m)$	*14.72 deg*
PM residual flux	B_r	*1.18 tesla*
stator pole pairs	P_s	*4*
PM pole pairs	P_m	*11*
number of modulators	P_{mod}	*15*
outer radius of stator	R_o	*50 mm*
inner radius of machine	R_i	*30 mm*
outer yoke thickness	L_{yo}	*5 mm*
inner yoke thickness	L_{yi}	*5 mm*
Height of stator pole	H_s	*10 mm*
Arc ratio of stator pole	α_s	*0.4*
number of stator slot	n_s	*36*
number of turns per coil	N_{coil}	*110*
electrical frequency of stator	f	*50 Hz*
mechanical speed of modulator rotor		*200 rpm*
mechanical speed of PM rotor		*272.73 rpm*

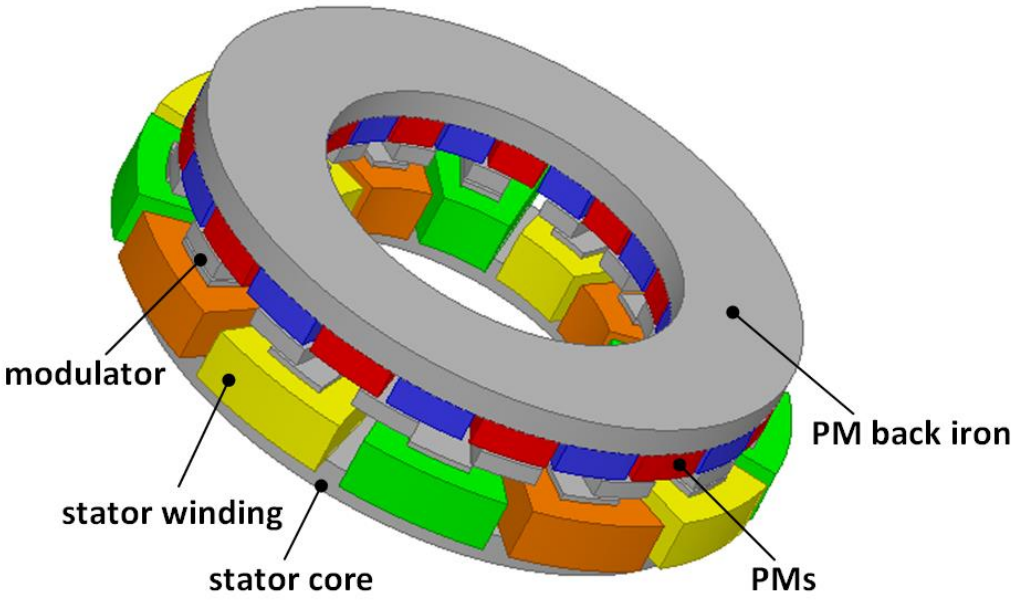

Figure 6.1: A typical axial-flux magnetically-geared machine

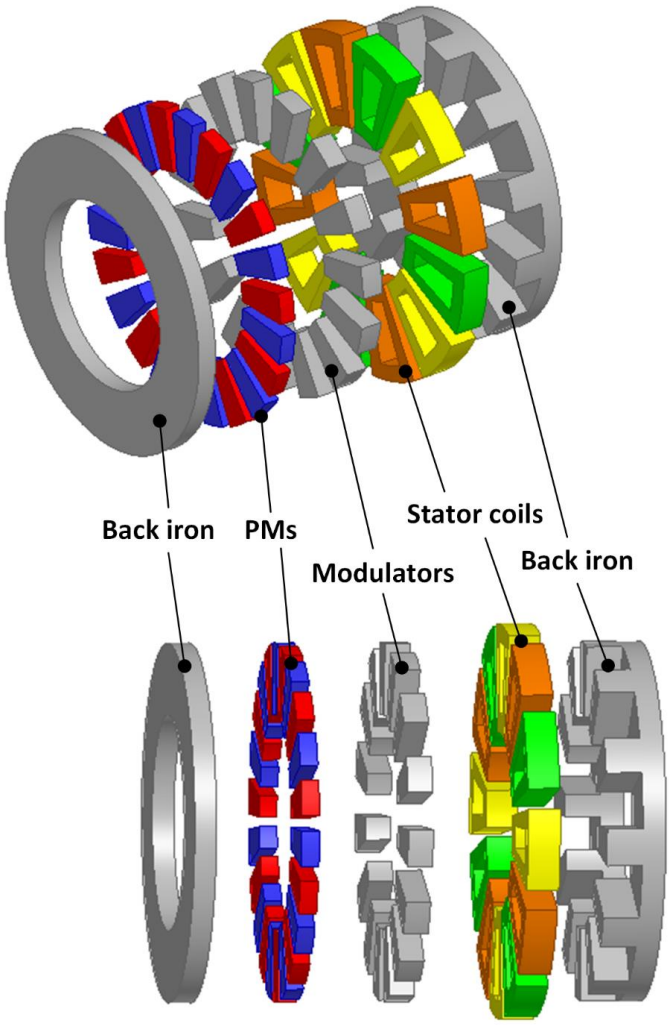

Figure 6.2: Exploded view of an axial-flux magnetically-geared machine

6.3 Field analysis

Meshed model of the machine, which is employed in the finite element analysis, is shown in Fig. 6.3. this not very fine but provides enough accuracy to investigate the ideas in the shortest time. In this case, stator of the machine is highly loaded to illustrate the fields more clearly. Fig. 6.4 shows magnetic flux density vectors within the machine and how they behave. Fig. 6.5 and Fig. 6.6 show magnetic flux density distribution in the stator-side air-gap for a line and a disc surface in the middle of the air-gap, respectively. The main harmonic of the stator ($p_s=4$) as well as the modulated ones can be observed. Fig. 6.7 illustrates the magnetic flux density distribution on a disc within the stator-side

air-gap having the rotation speed of *750 rpm* while the modulators in front of it with mechanical speed of *272.7 rpm* are depicted as well. The gearing idea can be observed.

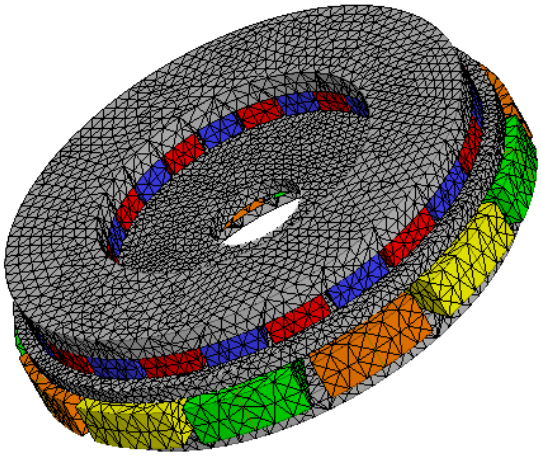

Figure 6.3: Meshing of the model

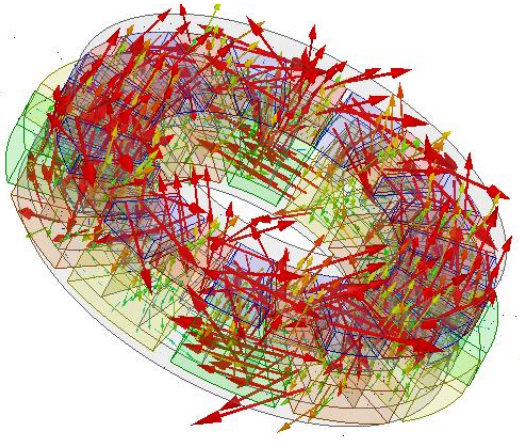

Figure 6.4: Magnetic flux density vectors within the machine

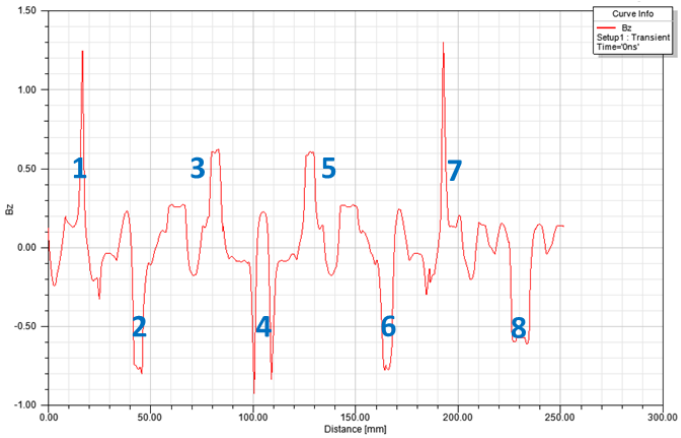

Figure 6.5: Magnetic flux density distribution on a line in the middle of the stator-side air-gap

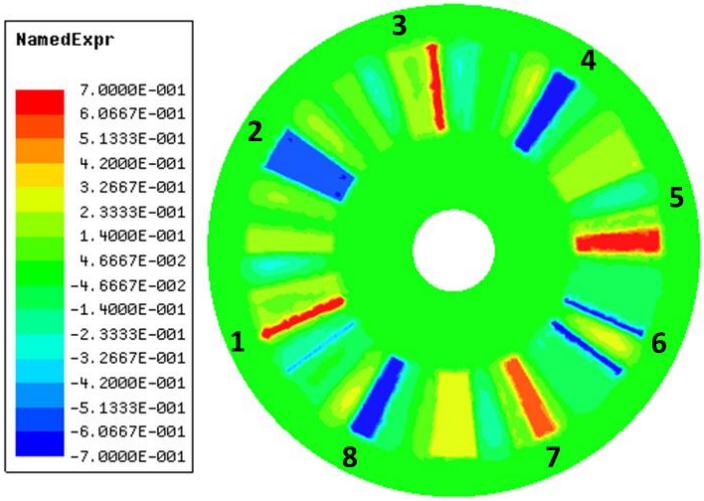

Figure 6.6: Magnetic flux density distribution on a disc surface in the middle of the stator-side air-gap

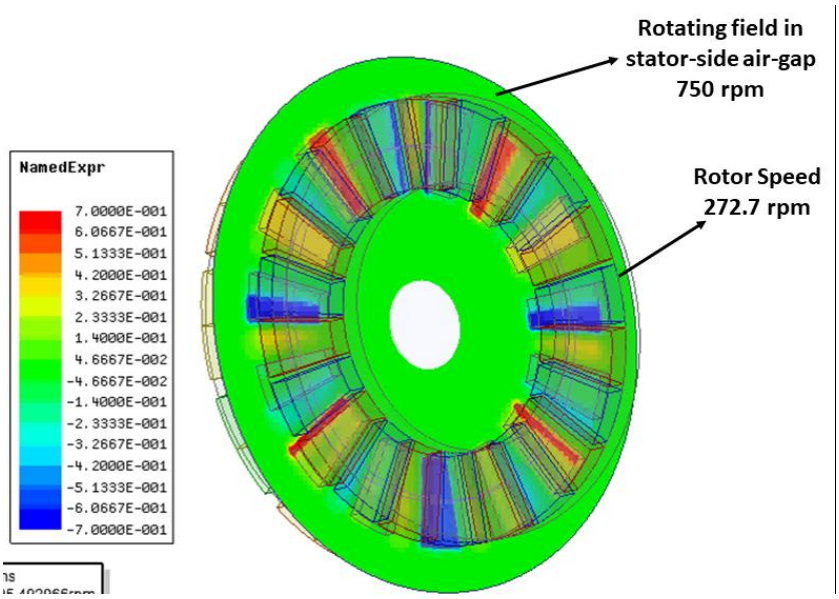

Figure 6.7: Magnetic flux density distribution on a disc surface in the middle of the stator-side air-gap illustrating the modulation effect and how the harmonics match the PMs on the other side

Fig. 6.8 and Fig. 6.9 show magnetic flux density distribution in the PM-side air-gap for a line and a disc surface in the middle of the air-gap, respectively. The main harmonic of the PM ring ($p_m=11$) as well as the modulated ones can be observed. Fig. 6.10 illustrates the magnetic flux density distribution on a disc within the PM-side air-gap while the effect of the modulator pieces behind it can be observed.

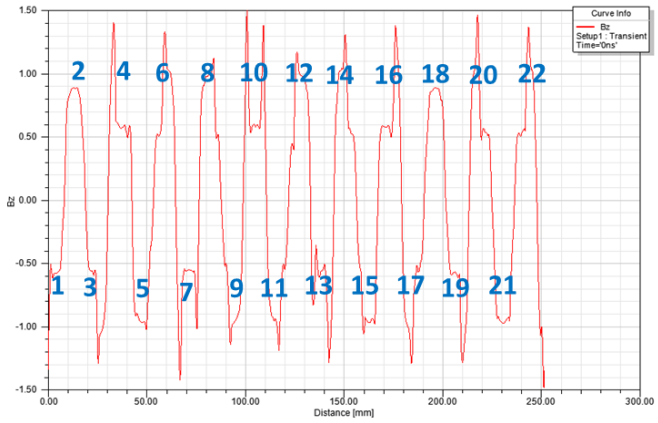

Figure 6.8: Magnetic flux density distribution on a line in the middle of the PM-side air-gap

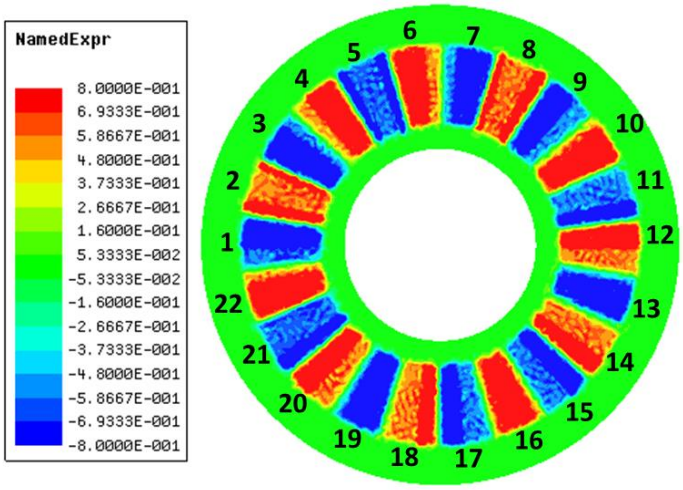

Figure 6.9: Magnetic flux density distribution on a disc surface in the middle of the PM-side air-gap

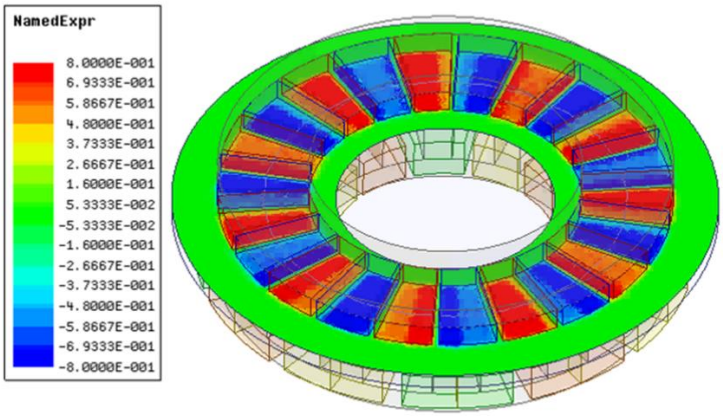

Figure 6.10: Magnetic flux density distribution on a disc surface in the middle of the PM-side air-gap illustrating the modulation effect and how the harmonics match the stator field on the other side

6.3.1 Torque and back-EMF

In this analysis, current in the windings is about *2* A_{rms}. Fig. 6. 11 and Fig. 6.12 show torque-angle characteristics of the machine when modulators and PMs are the rotor, respectively. The span of the half cycle is 180 electrical degrees for both, while it is 180/15=12 mechanical degrees for the former and 180/11=16.3 mechanical degrees for the latter. Better curves could be obtained by using a higher number of mesh elements—tradeoff between accuracy and time. Fig. 6.13 and Fig. 6.14 show the back-EMFs for the two cases when the rotors are rotating at the same angular speeds of 200rpm; it can be seen that the frequencies are not the same as result—gearing effect with different ratios.

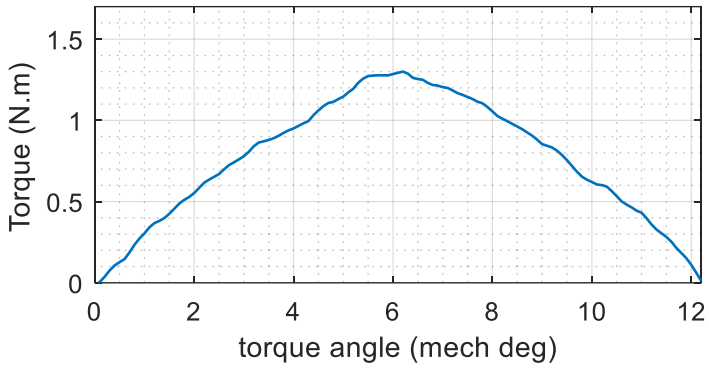

Figure 6.11: Torque angle characteristics when the modulator ring is the rotor

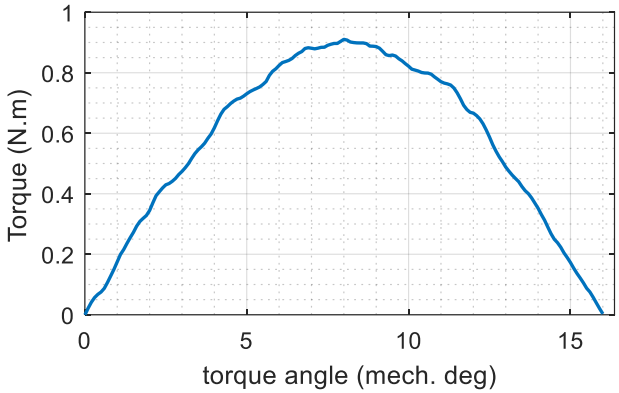

Figure 6.12: Torque angle characteristics when the PM ring is the rotor

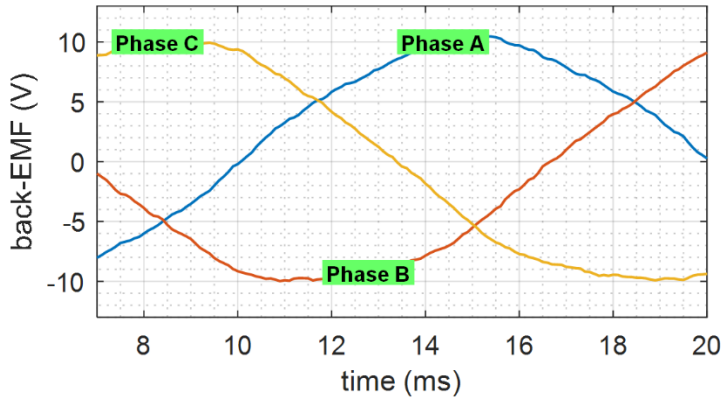

Figure 6.13: Back EMF when the modulator ring is the rotor

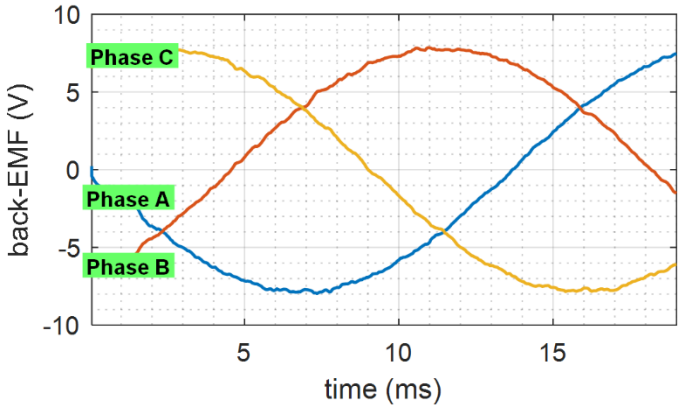

Figure 6.14: Back EMF when the PM ring is the rotor

Chapter 7

Conclusion and Future Works

7.1 conclusions

Analytical and numerical study of magnetically-geared machines is done in the research performed in this thesis. The former is performed by employing flux-tube methods and the latter is done using two-dimensional and three-dimensional finite element method (FEM) using the software Ansoft Maxwell. The two main structure of electrical machines, radial-flux and axial-flux configurations, are investigated. The flux-tube method, also called magnetic equivalent circuit (MEC), is very useful as a flexible yet accurate analytical framework for the study of the physics, analysis and design of the device. Development of this novel analytical model for magnetically-geared machines is done for the two cases of rotating modulator ring and rotating PM ring. Also, the model has been validated by FEM, showing a very close agreement between the analytical and numerical results. This framework can be utilized in preliminary designs and optimizations. The stator and the PMs are modeled by employing different techniques such as magnetization density, Amperian currents and coulombian fictitious charges, all of which provides a general framework so that a suitable technique can be used based on the geometry of the machine for further study of such devices. Closed-form expressions for the magnetic fields and the developed torques are extracted using different approaches including Maxwell stress tensor, Lorentz force and Kelvin force density. Advantage of the developed framework over existing ones is the flexibility and the capability to be applied to complex geometries. These options give the designers a flexibility to choose the most suitable technique according to the configuration and application of the device. Nature and behavior of magnetically-geared machines are studied and its main characteristics such as torque, field and back-EMF with different scenarios and conditions are extracted as well.

7.2 Future works

Magnetically-geared machines, by introducing many advantages and superiorities, has been of great interest in both industry and academia. The lines below are among the future works as well as ideas and suggestions for those who want lead a research in this interesting field:

- An attempt to reduce the discrepancy between the results obtained from the analytical model and FEM, although the accuracy is great and acceptable. The difference might be due to the flux leakage in the stator or the air-gap, or the saturation in the iron parts.

- Design optimization of the machine by using the closed-form expressions we extracted, and by employing genetic algorithm.

- Building a prototype of the machine based on the optimized design whose results can be compared with those obtained from analytical model and FEM.

- Parametric study and sensitivity analysis of the main characteristics of the device using the developed analytical framework

- Accounting for practical considerations such as temperature and cooling conditions.

- Analytical modeling of the machine by solving Laplace and Poisons' equations as an alternative to flux-tube based methods. Such models have their own advantages and disadvantages.

- Applying the modeling techniques to different structures, for example machines with interior PM or having double-stator or double-rotor configuration.

- In addition to 2D FEA of the radial-flux structure, it can be analyzed using 3D FEM to account for end turns of the stator winding.

- Deriving closed-form expressions for the machine back-EMF

- Deriving closed-form expressions for stator inductances

- Deriving a *dq*-model for the machine
- Control and drive study for the machine

Appendix A

Matlab code and plots for the Fourier series representation of the reluctance models

The code below is written to analyze the Fourier series for the models A and B of air-gap the reluctance.

```
%% Fourie series for reluctance model
%% Model A
clc;clear;

gie=1e-3;     % inner air-gap
go=1.5e-3;    % outer air-gap
hm=5e-3;      % PM height
hmod=4e-3;    % modulator height
wmod=6e-3;    % modulator sidth
u0=4*pi*1e-7;

pmod=11;           % number of modulators
Rav=pmod*wmod/pi; % average radius
dt=hm/(Rav*pi);    % area of Pmid

Pmax=u0/(gie+go+hm);
Pmid=(u0/hmod)*log(1+hmod/(gie+go+hm));
Pmin=u0/(gie+hmod+go+hm);



theta=0:(2*pi/pmod)/1000:2*pi/pmod;
P=Pmax * (theta<pi/(2*pmod)) + Pmid * ( (theta>=pi/(2*pmod)) &
(theta<pi/(2*pmod)+dt) )...
    + Pmin*((theta>=pi/(2*pmod)+dt) & (theta<1.5*pi/pmod-dt)) + Pmid*(
(theta>=1.5*pi/pmod-dt) & (theta<1.5*pi/pmod) )...
    +Pmax*(theta>=1.5*pi/pmod);

k=1;
for N=[1 10 50]

    a0=(pmod/pi)*( 0.5*(Pmax+Pmin)*(pi/pmod)+ (Pmid-Pmin)*dt);

    PP=zeros(1,length(theta))+a0;
    for n=1:2:N
        an=(2/(n*pi))*(Pmax-Pmid)*sin(n*pi/2) + (2/(n*pi))*(Pmid-
Pmin)*sin(n*pi/2+n*pmod*dt);
        PP=PP+an*cos(n*pmod*theta);
    end

    subplot(3,1,k)
    plot(theta,P,theta,PP)
    xlabel('\theta (deg)')
```

```
    ylabel('P (H/m^2)')
    axis tight
    title(['n=',num2str(N)])
    legend('P(\theta)', 'Fourier series')

    k=k+1;
end

%% Model B
clc;clear;

gie=1e-3;     % inner air-gap
go=1.5e-3;    % outer air-gap
hm=5e-3;      % PM height
hmod=4e-3;    % modulator height
wmod=6e-3;    % modulator sidth
u0=4*pi*1e-7;

pmod=11;           % number of modulators
Rav=pmod*wmod/pi; % average radius

Pmax=u0/(gie+go+hm);
Pmin=u0/(gie+hmod+go+hm);

theta=0:(2*pi/pmod)/1000:2*pi/pmod;
P=Pmax * (theta<pi/(2*pmod)) + Pmin*((theta>=pi/(2*pmod)) &
(theta<1.5*pi/pmod))...
    +Pmax*(theta>=1.5*pi/pmod);



    k=1;
for N=[1 10 50]

    a0=0.5*(Pmax+Pmin);

    PP=zeros(1,length(theta))+a0;
    for n=1:2:N
        an=(2/(n*pi))*(Pmax-Pmin)*sin(n*pi/2);
        PP=PP+an*cos(n*pmod*theta);
    end

    subplot(3,1,k)
    plot(theta,P,theta,PP)
    xlabel('\theta (deg)')
    ylabel('P (H/m^2)')
    axis tight
    title(['n=',num2str(N)])
    legend('P(\theta)', 'Fourier series')

    k=k+1;
end
```

Fig. A.1 shows the Fourier series representation of the permeance spatial distribution in model A for *n=1* (fundamental component), *n=10* and *n=50*. Also, Fig. A. 2 shows the

Fourier series representation of the permeance spatial distribution in model B for *n=1* (fundamental component), *n=10* and *n=50*.

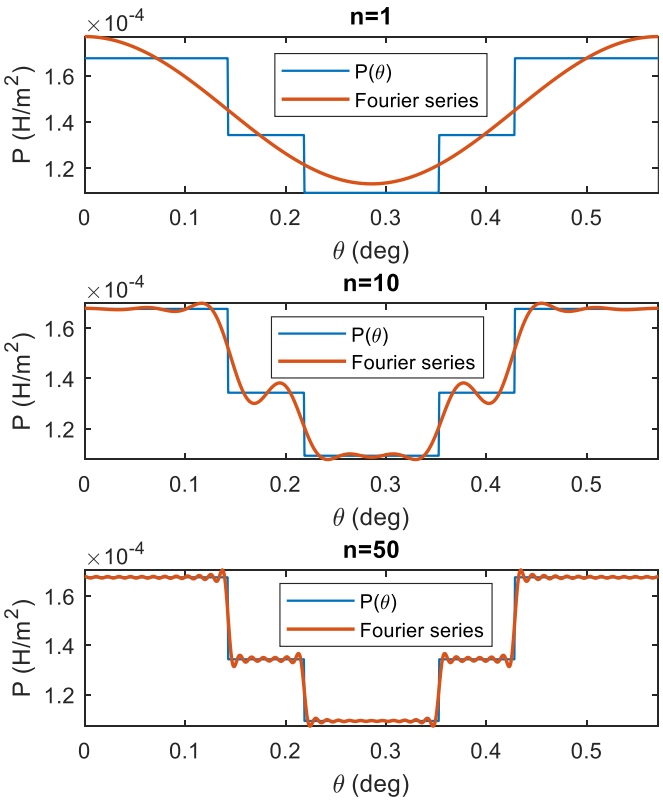

Figure A.1: Fourier series representation for the reluctance spatial distribution in model A

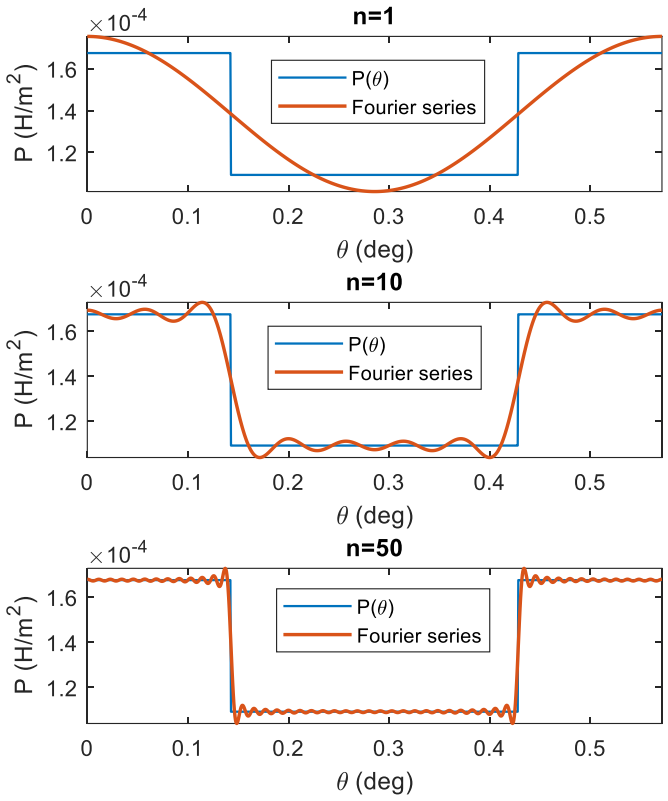

Figure A.2: Fourier series representation for the reluctance spatial distribution in model B

Appendix B

Matlab code and plots for the Fourier series representation of the magnetization distribution of permanent magnets

The code below is written to analyze the Fourier series for the magnetization distribution of the permanent magnets.

```
%% Fourie series for reluctance model
%% Model A
clc;clear;

Br=1.2;
u0=4*pi*1e-7;

pm=11;           % pole pair of PMs
theta_p=2*pi/(2*pm);
theta_m=0.8*theta_p;
dt=pi/(2*pm)-theta_m/2;

theta=0:(2*pi/pm)/1000:2*pi/pm;

MM=(Br/u0) * (theta<(pi/(2*pm)-dt)) + 0 * ( (theta>=(pi/(2*pm)-dt)) &
(theta<pi/(2*pm)+dt) )...
    + (-Br/u0)*((theta>=pi/(2*pm)+dt) & (theta<(1.5*pi/pm-dt))) + 0*(
(theta>=1.5*pi/pm-dt) & (theta<(1.5*pi/pm+dt)) )...
    +(Br/u0)*(theta>=1.5*pi/pm+dt);
k=1;
for N=[1 10 50]

    M=zeros(1,length(theta));
    for n=1:2:N
        an=(4/(n*pi))*(Br/u0)*sin(n*pm*theta_m/2);
        M=M+an*cos(n*pm*theta);
    end

    subplot(3,1,k)
    plot(theta*(180/pi),MM,theta*(180/pi),M)
    xlabel('\theta (deg)')
    ylabel('M')
    xlim([0,(180/pi)*2*pi/pm])
    title(['n=',num2str(N)])
    legend('M(\theta)', 'Fourier series')

    k=k+1;
end
```

Fig. B.1 shows the Fourier series representation of the spatial distribution of the magnetization of permanent magnets for *n=1* (fundamental component), *n=10* and *n=50*.

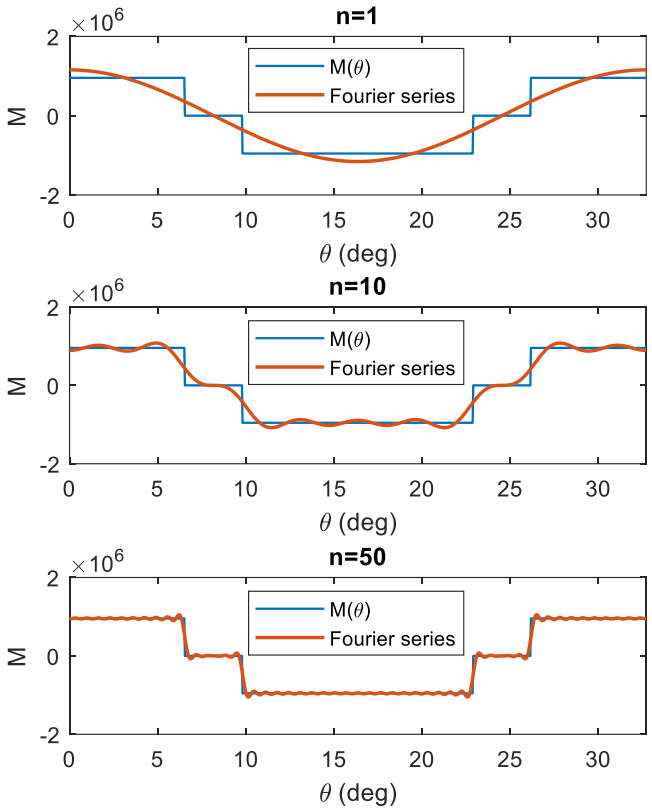

Figure B.1: Fourier series representation for the reluctance spatial distribution the spatial distribution of the PM magnetization

Appendix C

Unit Check for the torque expression

The developed torque for a magnetic gear having modulators as the rotor be expressed as in below:

$$T^e = -\frac{3}{2}\frac{4}{\pi}\left(1 \pm \frac{p_m}{p_s}\right)\frac{B_r}{\mu_0} R_{av}{}^2 L\, k_w N\, I_s \frac{h_m}{R_{av}} \wp_1 \sin\frac{p_m \theta_m}{2} \cos\left(\delta \mp p_{\text{mod}}\zeta\right) \tag{4.20}$$

where the unit of the sets of parameters are given below:

$-\frac{3}{2}\frac{4}{\pi}\left(1 \pm \frac{p_m}{p_s}\right)\sin\frac{p_m \theta_m}{2}\cos\left(\delta \mp p_{\text{mod}}\zeta\right)$: []

$\frac{B_r}{\mu_0}$: $[A/m]$

$R_{av}{}^2 L$: $[m^3]$

$k_w N\, I_s$: $[A]$

$\frac{h_m}{R_{av}}$: []

$\wp_1$: $[Tesla / A]$

According to Maxwell stress tensor $H_\theta B_r$, we know that *[A/m.Tesla]* is surface force density $[N.m_2]$, so mathematical manipulation leads to:

$$\left([A/m]\times[A]\times[Tesla/A]\right)=[A/m\times Tesla]\times[m^3]=[N/m^2]\times[m^3]=[N.m]$$

where *Nm* is the torque unit.

Appendix D

FFT Analysis Using Simulink

The data is first extracted from Ansoft Maxwell. Then it is imported to a Matlab m-file. Finally, it is saved to the workspace and imported to the Simulink (Simscape Power System) for FFF Analysis. The variables *Tstop* and *Ts* are inserted into Simulink file. The code below is a part of the m-file used. Fig. D.1 shows the Simulink sections.

```
BB=[0,-0.549449374139776
0.251320430970176,-0.497075457036888
0.502640861940351,-0.447867604226871
0.753961292910527,-0.399384620736442
1.0052817238807,-0.35124354989325
1.25660215485088,-0.352083496979221
1.50792258582105,-0.364324532383236
1.75924301679123,-0.385400514883324
2.0105634477614,-0.41391983092116
2.26188387873158,-0.452780550056095
2.51320430970176,-0.509681479165294
2.76452474067193,-0.549449542426018
3.01584517164211,-0.56568854832708
.
.
.
.
.
.
.
250.817790108235,-0.562761837329154
251.069110539205,-0.562160598660656
251.320430970176,-0.550949398238422];

% x=BB(:,1);
% y=BB(:,2);
% plot(x,y)
Bfield.time = BB(:,1);
Bfield.signals.values = BB(:,2);
Ts=BB(2,1)-BB(1,1);

t_stop=BB(end,1);

T=(BB(end,1)-BB(1,1));
freq=1/T;
```

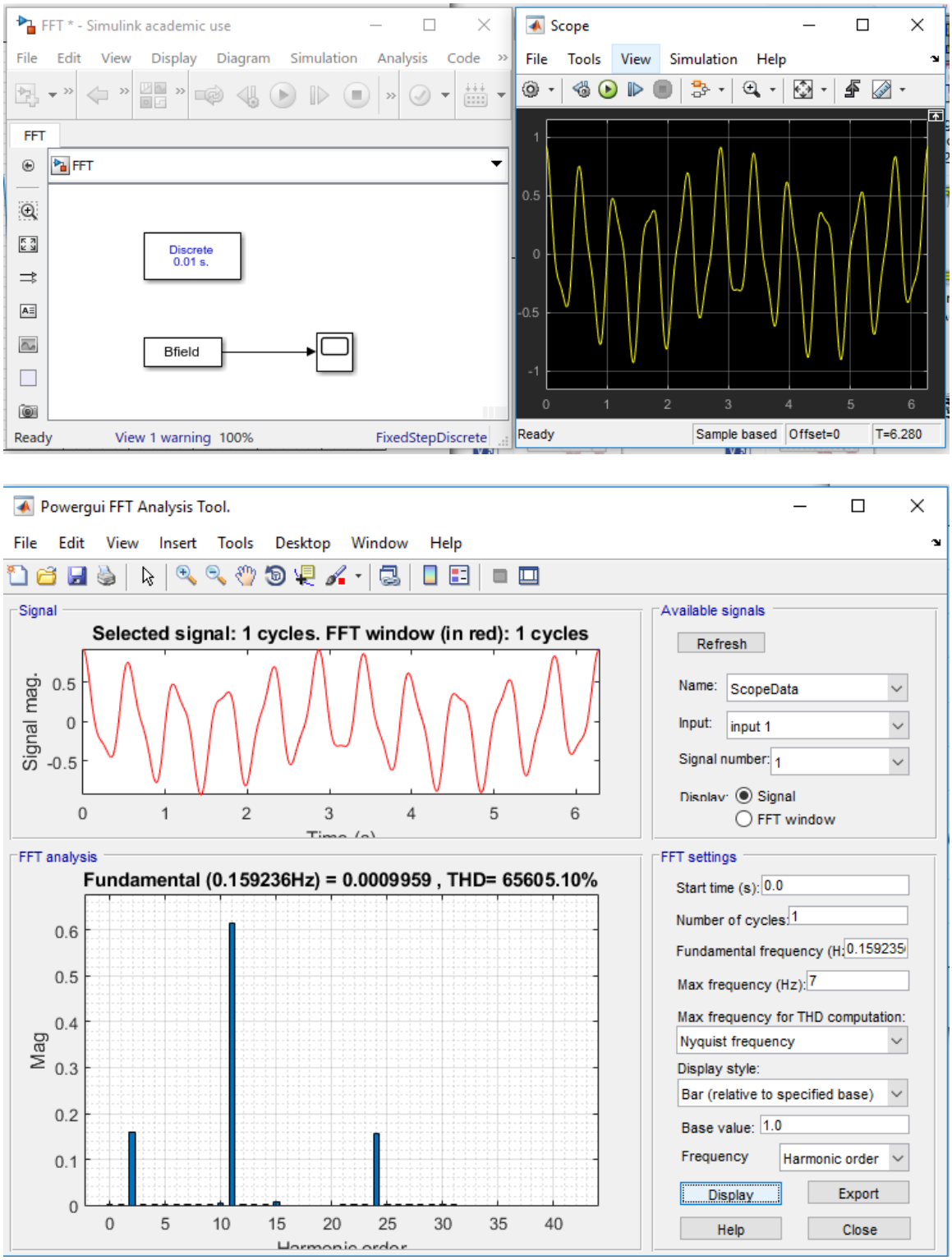

Figure D.1: FFT analysis using Simulink (Simscape Power Systems)

Appendix E

Matlab code for Analytical modeling of a radial-flux magnetically-geared machine with rotating modulators using the flux-tube based permeance model and Maxwell stress tensor

The code can be found below:

```
% Analytical modeling of magnetically-geared machines
% rotating modulators, flux-tube model
% Sajjad Mohammadi @ MIT, 2AM, May 23, 2019
clc;clear;

Irms=2.1; % RMS current of stator (A)
Is=sqrt(2)*Irms; % peak current of stator (A)
N=180; % total number of turns in a phase winding
f=50; % electrical frequency (Hz)

ps=2; % stator pole pair
pm=11; % PM pole pair
pmod=ps+pm; % modulator pole pair

alpha=0.9; % PM ratio
T_pm=alpha*2*pi/(2*pm); % PM arc

gi=1e-3;    % inner air-gap (m)
go=1e-3;   % outer air-gap (m)

hm=5e-3;     % PM height (m)
hmod=6e-3;   % modulator height (m)
%hmod=0.020498409140724+0.01

R1=50e-3; % stator outer radius (m)
R2=R1+gi+hmod+go; % inner radius of PMs (m)
Rav=(R1+R2)/2; % average radius of modulators (m)

slot=36; % number of stator slots
mm=3; % slot per pole per phase (distributed winding)
gamma=ps*2*pi/slot; % slot pitch (electrical degrees)
kd=sin(mm*gamma/2)/(mm*sin(gamma/2)); % distribution factor
kp=1; % pitch factor
kw=kp*kd; % winding factor

w=R1*2*pi/slot; % slot pitch (m)
ws=2e-3; % slot opening (m)
kc=( 1-(ws/w)+(4*gi/(pi*w))*log(1+pi*ws/(4*gi)) )^(-1); %Carter's
coefficient
```

```
gie=kc*gi; %effective air-gap (m)
g_diff=gie-gi; % g-difference
R1=R1-g_diff; % reducing the stator outer radius by g-diffrence (m)
Rav_t=(R1+R2)/2; % average radius of torque calculations (m)

L=50e-3; % axial length (m)

Br=1.15; % residual flux of PMs (T)
u0=4*pi*1e-7;
M0=Br/u0; % PM Magnetization
Hc=837e3;
ur=Br/(u0*Hc);

T_mod=2*pi/(2*pmod); % modulator arc (rad)
wmod=Rav*T_mod; % modulator width (m)

% switching between the two flux tube models
if hmod<(pi*wmod/2)

    % Model A
    Pmin=u0/(ur*(gie+hmod+go)+hm);
    Pmid=(u0/hmod)*log(1+ur*hmod/(ur*(gie+go)+hm));
    Pmax=u0/(ur*(gie+go)+hm);

    dt=hmod/(pi*Rav);
    P0=(1/2)*(Pmax+Pmin)+(pmod*dt/pi)*(Pmid-Pmin);
    P1=(2/pi)*(Pmax-Pmid)+(2/pi)*(Pmid-Pmin)*sin(pi/2+pmod*dt);
    disp('model A')
else

    % Model B
    Pmin=(2*u0/(pi*wmod))*log(1+pi*wmod/(2*(gie+go+hm)));
    Pmax=u0/(gie+go+hm);

    P0=(1/2)*(Pmax+Pmin);
    P1=(1/2)*(4/pi)*(Pmax-Pmin);
    disp('model B')
end

beta=0:0.01:pi; % torque angle (rad)

Tmax=(3/2)*(4/pi)*(R1+R2*pm/ps)*(Br/u0)*L*kw*N*Is*hm*P1*sin(pm*T_pm/2);
% maximum torque
%
Tmax=(3/2)*(4/pi)*(1+pm/ps)*(Br/u0)*Rav_t*L*kw*N*Is*hm*P1*sin(pm*T_pm/2
); % maximum torque
Torque=-Tmax*sin(beta); % torque angle curve

disp(Tmax)
plot(beta*((1/pmod)*180/pi),-Torque)
xlabel('Torque angle (mech deg)')
ylabel('Torque (Nm)')
grid; grid minor
```

```
% spatial distribution of the radial field
delta=0; % current angle
zeta=0; % modulator intial angle
omega=2*pi*f;
omega_m=omega/pmod; % mechanical speed (rad/sec)
time=0; %time

Fs1=(-3/2)*(4/pi)*(N*Is/(2*ps))*kw;

theta=0:0.01:2*pi; % spatial angular position

% spatial distribution of Br
Br=Fs1*P0*sin(ps*theta-omega*time-delta)...
  +(1/2)*Fs1*P1*sin((ps-pmod)*theta-omega*time-delta)...
  +(1/2)*Fs1*P1*sin( (ps+pmod)*theta-omega*time-delta)...
  +hm*M0*P0*cos(pm*theta-pm*omega_m*time-pm*zeta)...
  +(1/2)*hm*M0*P1*cos((pm-pmod)*theta-pm*omega_m*time-pm*zeta)...
  +(1/2)*hm*M0*P1*cos((pm+pmod)*theta-pm*omega_m*time-pm*zeta);
figure
plot((180/pi)*theta,Br)
xlabel('theta (mech deg)')
ylabel('B_r (T)')
grid; grid minor

% for TTF analysis using simulink
Bfield.time = theta';
Bfield.signals.values = Br';
Ts=theta(2)-theta(1);

t_stop=theta(end);

T=(theta(end)-theta(1));
freq=1/T;
```

Appendix F

Matlab code for Analytical modeling of a radial-flux magnetically-geared machine with rotating modulators using the flux-tube based permeance model and Lorentz law on Amperian current of PMs

The code can be found below:

```
% Analytical modeling of magnetically-geared machines
% rotating modulators, flux-tube model
% Sajjad Mohammadi @ MIT, 2AM, May 23, 2019
clc;clear;

Irms=2.1; % RMS current of stator (A)
Is=sqrt(2)*Irms; % peak current of stator (A)
N=180; % total number of turns in a phase winding
f=50; % electrical frequency (Hz)

ps=2; % stator pole pair
pm=11; % PM pole pair
pmod=ps+pm; % modulator pole pair

alpha=0.9; % PM ratio
T_pm=alpha*2*pi/(2*pm); % PM arc

gi=1e-3;    % inner air-gap (m)
go=1e-3;   % outer air-gap (m)

hm=5e-3;     % PM height (m)
hmod=6e-3;   % modulator height (m)
%hmod=0.020498409140724+0.01

R1=50e-3; % stator outer radius (m)
R2=R1+gi+hmod+go; % inner radius of PMs (m)
Rav=(R1+R2)/2; % average radius of modulators (m)

slot=36; % number of stator slots
mm=3; % slot per pole per phase (distributed winding)
gamma=ps*2*pi/slot; % slot pitch (electrical degrees)
kd=sin(mm*gamma/2)/(mm*sin(gamma/2)); % distribution factor
kp=1; % pitch factor
kw=kp*kd; % winding factor

w=R1*2*pi/slot; % slot pitch (m)
```

```
ws=2e-3; % slot opening (m)
kc=( 1-(ws/w)+(4*gi/(pi*w))*log(1+pi*ws/(4*gi)) )^(-1); %Carter's
coefficient

gie=kc*gi; %effective air-gap (m)
g_diff=gie-gi; % g-difference
R1=R1-g_diff; % reducing the stator outer radius by g-diffrence (m)
Rav_t=(R1+R2)/2; % average radius of torque calculations (m)

L=50e-3; % axial length (m)

Br=1.15; % residual flux of PMs (T)
u0=4*pi*1e-7;
M0=Br/u0; % PM Magnetization
Hc=837e3;
um=Br/(u0*Hc);

T_mod=2*pi/(2*pmod); % modulator arc (rad)
wmod=Rav*T_mod; % modulator width (m)

% switching between the two flux tube models
if hmod<(pi*wmod/2)

    % Model A
    Pmin=u0/(gie+hmod+go+hm);
    Pmid=(u0/hmod)*log(1+hmod/(gie+go+hm));
    Pmax=u0/(gie+go+hm);

    dt=hmod/(pi*Rav);
    P0=(1/2)*(Pmax+Pmin)+(pmod*dt/pi)*(Pmid-Pmin);
    P1=(2/pi)*(Pmax-Pmid)+(2/pi)*(Pmid-Pmin)*sin(pi/2+pmod*dt);
    disp('model A')
else

    % Model B
    Pmin=(2*u0/(pi*wmod))*log(1+pi*wmod/(2*(gie+go+hm)));
    Pmax=u0/(gie+go+hm);

    P0=(1/2)*(Pmax+Pmin);
    P1=(1/2)*(4/pi)*(Pmax-Pmin);
    disp('model B')
end

beta=0:0.01:pi; % torque angle (rad)

Ts=(3/2)*(4/pi)*(R1)*(Br/u0)*L*kw*N*Is*hm*P1*sin(pm*T_pm/2);
Tm=(3/2)*(4/pi)*(R2*hm+hm^2)*pm/ps*(Br/u0)*L*kw*N*Is*P1*sin(pm*T_pm/2);
%lorentz law
Tmax=Ts+Tm;
%
Tmax=(3/2)*(4/pi)*(1+pm/ps)*(Br/u0)*Rav_t*L*kw*N*Is*hm*P1*sin(pm*T_pm/2
); % maximum torque
Torque=-Tmax*sin(beta); % torque angle curve
disp(Tmax)
```

```
plot(beta*((1/pmod)*180/pi),-Torque)
xlabel('Torque angle (mech deg)')
ylabel('Torque (Nm)')
grid; grid minor

% spatial distribution of the radial field
delta=0; % current angle
zeta=0; % modulator intial angle
omega=2*pi*f;
omega_m=omega/pmod; % mechanical speed (rad/sec)
time=0; %time

Fs1=(-3/2)*(4/pi)*(N*Is/(2*ps))*kw;

theta=0:0.01:2*pi; % spatial angular position

% spatial distribution of Br
Br=Fs1*P0*sin(ps*theta-omega*time-delta)...
  +(1/2)*Fs1*P1*sin((ps-pmod)*theta-omega*time-delta)...
  +(1/2)*Fs1*P1*sin( (ps+pmod)*theta-omega*time-delta)...
  +hm*M0*P0*cos(pm*theta-pm*omega_m*time-pm*zeta)...
  +(1/2)*hm*M0*P1*cos((pm-pmod)*theta-pm*omega_m*time-pm*zeta)...
  +(1/2)*hm*M0*P1*cos((pm+pmod)*theta-pm*omega_m*time-pm*zeta);
figure
plot((180/pi)*theta,Br)
xlabel('theta (mech deg)')
ylabel('B_r (T)')
grid; grid minor

% for TTF analysis using simulink
Bfield.time = theta';
Bfield.signals.values = Br';
Ts=theta(2)-theta(1);

t_stop=theta(end);

T=(theta(end)-theta(1));
freq=1/T;
```

Appendix G

Matlab code for Analytical modeling of a radial-flux magnetically-geared machine with rotating modulators using the simplified permeance model and Maxwell stress tensor

The code can be found below:

```
% Analytical modeling of magnetically-geared machines
% rotating modulators, simplified model
% Sajjad Mohammadi @ MIT, 2AM, May 23, 2019
clc;clear;

Irms=2.1; % RMS current of stator (A)
Is=sqrt(2)*Irms; % peak current of stator (A)
N=180; % total number of turns in a phase winding
f=50; % electrical frequency (Hz)

ps=2; % stator pole pair
pm=11; % PM pole pair
pmod=ps+pm; % modulator pole pair

alpha=0.9; % PM ratio
T_pm=alpha*2*pi/(2*pm); % PM arc

gi=1e-3;    % inner air-gap (m)
go=1e-3;   % outer air-gap (m)

hm=5e-3;     % PM height (m)
hmod=6e-3;   % modulator height (m)

R1=50e-3; % stator outer radius (m)
R2=R1+gi+hmod+go; % inner radius of PMs (m)
Rav=(R1+R2)/2; % average radius of modulators (m)

slot=36; % number of stator slots
mm=3; % slot per pole per phase (distributed winding)
gamma=ps*2*pi/slot; % slot pitch (electrical degrees)
kd=sin(mm*gamma/2)/(mm*sin(gamma/2)); % distribution factor
kp=1; % pitch factor
kw=kp*kd; % winding factor

w=R1*2*pi/slot; % slot pitch (m)
ws=2e-3; % slot opening (m)
kc=( 1-(ws/w)+(4*gi/(pi*w))*log(1+pi*ws/(4*gi)) )^(-1); %Carter's
coefficient
```

```
gie=kc*gi; %effective air-gap (m)
g_diff=gie-gi; % g-difference
R1=R1-g_diff; % reducing the stator outer radius by g-diffrence (m)
Rav_t=(R1+R2)/2; % average radius of torque calculations (m)

L=50e-3; % axial length (m)

Br=1.15; % residual flux of PMs (T)
u0=4*pi*1e-7;
M0=Br/u0; % PM Magnetization

% Simplest Model
Pmax=u0/(gi+go+hm);
Pmin=u0/(gi+hmod+go+hm);
P0=(1/2)*(Pmax+Pmin);
P1=(1/2)*(4/pi)*(Pmax-Pmin);

beta=0:0.01:pi; % torque angle (rad)

Tmax=(3/2)*(4/pi)*(1+pm/ps)*(Br/u0)*R2*L*kw*N*Is*hm*P1*sin(pm*T_pm/2);
% maximum torque
Torque=-Tmax*sin(beta); % torque angle curve

disp(Tmax)
plot(beta*((1/pmod)*180/pi),-Torque)
xlabel('Torque angle (mech deg)')
ylabel('Torque (Nm)')
grid; grid minor

% spatial distribution of the radial field
delta=0; % current angle
zeta=0; % modulator initial angle
omega=2*pi*f;
omega_m=omega/pmod; % mechanical speed (rad/sec)
time=0; %time

Fs1=(-3/2)*(4/pi)*(N*Is/(2*ps))*kw;

theta=0:0.01:2*pi; % spatial angular position
% spatial distribution of Br
Br=Fs1*P0*sin(ps*theta-omega*time-delta)...
  +(1/2)*Fs1*P1*sin((ps-pmod)*theta-(omega-pmod*omega_m)*time-
delta+pmod*zeta)...
  +(1/2)*Fs1*P1*sin( (ps+pmod)*theta-(omega+pmod*omega_m)*time-delta-
pmod*zeta )...
  +hm*M0*P0*cos(pm*theta)...
  +(1/2)*hm*M0*P1*cos((pm-pmod)*theta+pmod*omega_m*time+pmod*zeta)...
  +(1/2)*hm*M0*P1*cos((pm+pmod)*theta-pmod*omega_m*time-pmod*zeta);
figure
plot((180/pi)*theta,Br)
xlabel('theta (mech deg)')
ylabel('B_r (T)')
grid; grid minor
```

Appendix H

Matlab code for Analytical modeling of a radial-flux magnetically-geared machine with rotating PMs using the flux-tube based permeance model and Maxwell stress tensor

The code can be found below:

```
% Analytical modeling of magnetically-geared machines
% rotating PMs, flux-tube model
% Sajjad Mohammadi @ MIT, 2AM, May 23, 2019
clc;clear;

Irms=2.1; % RMS current of stator (A)
Is=sqrt(2)*Irms; % peak current of stator (A)
N=180; % total number of turns in a phase winding
f=50; % electrical frequency (Hz)

ps=2; % stator pole pair
pm=11; % PM pole pair
pmod=ps+pm; % modulator pole pair

alpha=0.9; % PM ratio
T_pm=alpha*2*pi/(2*pm); % PM arc

gi=1e-3;    % inner air-gap (m)
go=1e-3;   % outer air-gap (m)

hm=5e-3;     % PM height (m)
hmod=6e-3;   % modulator height (m)

R1=50e-3; % stator outer radius (m)
R2=R1+gi+hmod+go; % inner radius of PMs (m)
Rav=(R1+R2)/2; % average radius of modulators (m)

slot=36; % number of stator slots
mm=3; % slot per pole per phase (distributed winding)
gamma=ps*2*pi/slot; % slot pitch (electrical degrees)
kd=sin(mm*gamma/2)/(mm*sin(gamma/2)); % distribution factor
kp=1; % pitch factor
kw=kp*kd; % winding factor

w=R1*2*pi/slot; % slot pitch (m)
ws=2e-3; % slot opening (m)
kc=( 1-(ws/w)+(4*gi/(pi*w))*log(1+pi*ws/(4*gi)) )^(-1); %Carter's
coefficient

gie=kc*gi; %effective air-gap (m)
```

```
g_diff=gie-gi; % g-difference
R1=R1-g_diff; % reducing the stator outer radius by g-diffrence (m)
Rav_t=(R1+R2)/2; % average radius of torque calculations (m)

L=50e-3; % axial length (m)

Br=1.15; % residual flux of PMs (T)
u0=4*pi*1e-7;
M0=Br/u0; % PM Magnetization

T_mod=2*pi/(2*pmod); % modulator arc (rad)
wmod=Rav*T_mod; % modulator width (m)

% switching between the two flux tube models
if hmod<(pi*wmod/2)

    % Model A
    Pmin=u0/(gie+hmod+go+hm);
    Pmid=(u0/hmod)*log(1+hmod/(gie+go+hm));
    Pmax=u0/(gie+go+hm);

    dt=hmod/(pi*Rav);
    P0=(1/2)*(Pmax+Pmin)+(pmod*dt/pi)*(Pmid-Pmin);
    P1=(2/pi)*(Pmax-Pmid)+(2/pi)*(Pmid-Pmin)*sin(pi/2+pmod*dt);
    disp('model A')
else

    % Model B
    Pmin=(2*u0/(pi*wmod))*log(1+pi*wmod/(2*(gie+go+hm)));
    Pmax=u0/(gie+go+hm);

    P0=(1/2)*(Pmax+Pmin);
    P1=(1/2)*(4/pi)*(Pmax-Pmin);
    disp('model B')
end

beta=0:0.01:pi; % torque angle (rad)

Tmax=(3/2)*(4/pi)*(pm/ps)*(Br/u0)*R2*L*kw*N*Is*hm*P1*sin(pm*T_pm/2); %
maximum torque
Torque=-Tmax*sin(beta); % torque angle curve

disp(Tmax)
plot(beta*((1/pm)*180/pi),-Torque)
xlabel('Torque angle (mech deg)')
ylabel('Torque (Nm)')
grid; grid minor


% spatial distribution of the radial field
delta=0; % current angle
zeta=0; % modulator intial angle
omega=2*pi*f;
```

```
% [be careful about pm or pmod]
omega_m=omega/pm; % mechanical speed (rad/sec)
time=0; %time

Fs1=(-3/2)*(4/pi)*(N*Is/(2*ps))*kw;

theta=0:0.01:2*pi; % spatial angular position
% spatial distribution of Br
Br=Fs1*P0*sin(ps*theta-omega*time-delta)...
  +(1/2)*Fs1*P1*sin((ps-pmod)*theta-omega*time-delta)...
  +(1/2)*Fs1*P1*sin( (ps+pmod)*theta-omega*time-delta)...
  +hm*M0*P0*cos(pm*theta-pm*omega_m*time-pm*zeta)...
  +(1/2)*hm*M0*P1*cos((pm-pmod)*theta-pm*omega_m*time-pm*zeta)...
  +(1/2)*hm*M0*P1*cos((pm+pmod)*theta-pm*omega_m*time-pm*zeta);
figure
plot((180/pi)*theta,Br)
xlabel('theta (mech deg)')
ylabel('B_r (T)')
grid; grid minor

% for TTF analysis using simulink
Bfield.time = theta';
Bfield.signals.values = Br';
Ts=theta(2)-theta(1);

t_stop=theta(end);

T=(theta(end)-theta(1));
freq=1/T;
```

Appendix I

Matlab code for Analytical modeling of a radial-flux magnetically-geared machine with rotating PMs using the flux-tube based permeance model and Lorentz law on Amperian current of PMs

```
% Analytical modeling of magnetically-geared machines
% rotating PMs, flux-tube model
% Sajjad Mohammadi @ MIT, 2AM, May 23, 2019
clc;clear;

Irms=2.1; % RMS current of stator (A)
Is=sqrt(2)*Irms; % peak current of stator (A)
N=180; % total number of turns in a phase winding
f=50; % electrical frequency (Hz)

ps=2; % stator pole pair
pm=11; % PM pole pair
pmod=ps+pm; % modulator pole pair

alpha=0.9; % PM ratio
T_pm=alpha*2*pi/(2*pm); % PM arc

gi=1e-3;    % inner air-gap (m)
go=1e-3;   % outer air-gap (m)

hm=5e-3;     % PM height (m)
hmod=6e-3;   % modulator height (m)

R1=50e-3; % stator outer radius (m)
R2=R1+gi+hmod+go; % inner radius of PMs (m)
Rav=(R1+R2)/2; % average radius of modulators (m)

slot=36; % number of stator slots
mm=3; % slot per pole per phase (distributed winding)
gamma=ps*2*pi/slot; % slot pitch (electrical degrees)
kd=sin(mm*gamma/2)/(mm*sin(gamma/2)); % distribution factor
kp=1; % pitch factor
kw=kp*kd; % winding factor

w=R1*2*pi/slot; % slot pitch (m)
ws=2e-3; % slot opening (m)
kc=( 1-(ws/w)+(4*gi/(pi*w))*log(1+pi*ws/(4*gi)) )^(-1); %Carter's
coefficient

gie=kc*gi; %effective air-gap (m)
g_diff=gie-gi; % g-difference
```

```
R1=R1-g_diff; % reducing the stator outer radius by g-diffrence (m)
Rav_t=(R1+R2)/2; % average radius of torque calculations (m)

L=50e-3; % axial length (m)

Br=1.15; % residual flux of PMs (T)
u0=4*pi*1e-7;
M0=Br/u0; % PM Magnetization

T_mod=2*pi/(2*pmod); % modulator arc (rad)
wmod=Rav*T_mod; % modulator width (m)

% switching between the two flux tube models
if hmod<(pi*wmod/2)

    % Model A
    Pmin=u0/(gie+hmod+go+hm);
    Pmid=(u0/hmod)*log(1+hmod/(gie+go+hm));
    Pmax=u0/(gie+go+hm);

    dt=hmod/(pi*Rav);
    P0=(1/2)*(Pmax+Pmin)+(pmod*dt/pi)*(Pmid-Pmin);
    P1=(2/pi)*(Pmax-Pmid)+(2/pi)*(Pmid-Pmin)*sin(pi/2+pmod*dt);
    disp('model A')
else

    % Model B
    Pmin=(2*u0/(pi*wmod))*log(1+pi*wmod/(2*(gie+go+hm)));
    Pmax=u0/(gie+go+hm);

    P0=(1/2)*(Pmax+Pmin);
    P1=(1/2)*(4/pi)*(Pmax-Pmin);
    disp('model B')
end

beta=0:0.01:pi; % torque angle (rad)

Tmax=(3/2)*(4/pi)*(R2*hm+hm^2)*pm/ps*(Br/u0)*L*kw*N*Is*P1*sin(pm*T_pm/2
); %lorentz law
Torque=-Tmax*sin(beta); % torque angle curve

disp(Tmax)
plot(beta*((1/pm)*180/pi),-Torque)
xlabel('Torque angle (mech deg)')
ylabel('Torque (Nm)')
grid; grid minor



% spatial distribution of the radial field
delta=0; % current angle
zeta=0; % modulator intial angle
omega=2*pi*f;

% [be careful about pm or pmod]
```

```
omega_m=omega/pm; % mechanical speed (rad/sec)
time=0; %time

Fs1=(-3/2)*(4/pi)*(N*Is/(2*ps))*kw;

theta=0:0.01:2*pi; % spatial angular position
% spatial distribution of Br
Br=Fs1*P0*sin(ps*theta-omega*time-delta)...
  +(1/2)*Fs1*P1*sin((ps-pmod)*theta-omega*time-delta)...
  +(1/2)*Fs1*P1*sin( (ps+pmod)*theta-omega*time-delta)...
  +hm*M0*P0*cos(pm*theta-pm*omega_m*time-pm*zeta)...
  +(1/2)*hm*M0*P1*cos((pm-pmod)*theta-pm*omega_m*time-pm*zeta)...
  +(1/2)*hm*M0*P1*cos((pm+pmod)*theta-pm*omega_m*time-pm*zeta);
figure
plot((180/pi)*theta,Br)
xlabel('theta (mech deg)')
ylabel('B_r (T)')
grid; grid minor

% for TTF analysis using simulink
Bfield.time = theta';
Bfield.signals.values = Br';
Ts=theta(2)-theta(1);

t_stop=theta(end);

T=(theta(end)-theta(1));
freq=1/T;
```

Appendix J

Matlab code for Analytical modeling of a radial-flux magnetically-geared machine with rotating PMs using the simplified permeance model and Maxwell stress tensor

The code can be found below:

```
% Analytical modeling of magnetically-geared machines
% rotating PMs, simplified model
% Sajjad Mohammadi @ MIT, 2AM, May 23, 2019
clc;clear;

Irms=2.1; % RMS current of stator (A)
Is=sqrt(2)*Irms; % peak current of stator (A)
N=180; % total number of turns in a phase winding
f=50; % electrical frequency (Hz)

ps=2; % stator pole pair
pm=11; % PM pole pair
pmod=ps+pm; % modulator pole pair

alpha=0.9; % PM ratio
T_pm=alpha*2*pi/(2*pm); % PM arc

gi=1e-3;    % inner air-gap (m)
go=1e-3;   % outer air-gap (m)

hm=5e-3;     % PM height (m)
hmod=6e-3;   % modulator height (m)

R1=50e-3; % stator outer radius (m)
R2=R1+gi+hmod+go; % inner radius of PMs (m)
Rav=(R1+R2)/2; % average radius of modulators (m)

slot=36; % number of stator slots
mm=3; % slot per pole per phase (distributed winding)
gamma=ps*2*pi/slot; % slot pitch (electrical degrees)
kd=sin(mm*gamma/2)/(mm*sin(gamma/2)); % distribution factor
kp=1; % pitch factor
kw=kp*kd; % winding factor

w=R1*2*pi/slot; % slot pitch (m)
ws=2e-3; % slot opening (m)
kc=( 1-(ws/w)+(4*gi/(pi*w))*log(1+pi*ws/(4*gi)) )^(-1); %Carter's
coefficient
```

```
gie=kc*gi; %effective air-gap (m)
g_diff=gie-gi; % g-difference
R1=R1-g_diff; % reducing the stator outer radius by g-diffrence (m)
Rav_t=(R1+R2)/2; % average radius of torque calculations (m)

L=50e-3; % axial length (m)

Br=1.15; % residual flux of PMs (T)
u0=4*pi*1e-7;
M0=Br/u0; % PM Magnetization

% Simplest Model
Pmax=u0/(gi+go+hm);
Pmin=u0/(gi+hmod+go+hm);
P0=(1/2)*(Pmax+Pmin);
P1=(1/2)*(4/pi)*(Pmax-Pmin);

beta=0:0.01:pi; % torque angle (rad)

Tmax=(3/2)*(4/pi)*(pm/ps)*(Br/u0)*Rav_t*L*kw*N*Is*hm*P1*sin(pm*T_pm/2);
% maximum torque
Torque=-Tmax*sin(beta); % torque angle curve

disp(Tmax)
plot(beta*((1/pm)*180/pi),-Torque)
xlabel('Torque angle (mech deg)')
ylabel('Torque (Nm)')
grid; grid minor

% spatial distribution of the radial field
delta=0; % current angle
zeta=0; % modulator intial angle
omega=2*pi*f;

% [be carful about pm or pmod]
omega_m=omega/pm; % mechanical speed (rad/sec)
time=0; %time

Fs1=(-3/2)*(4/pi)*(N*Is/(2*ps))*kw;

theta=0:0.01:2*pi; % spatial angular position
% spatial distribution of Br
Br=Fs1*P0*sin(ps*theta-omega*time-delta)...
  +(1/2)*Fs1*P1*sin((ps-pmod)*theta-omega*time-delta)...
  +(1/2)*Fs1*P1*sin( (ps+pmod)*theta-omega*time-delta)...
  +hm*M0*P0*cos(pm*theta-pm*omega_m*time-pm*zeta)...
  +(1/2)*hm*M0*P1*cos((pm-pmod)*theta-pm*omega_m*time-pm*zeta)...
  +(1/2)*hm*M0*P1*cos((pm+pmod)*theta-pm*omega_m*time-pm*zeta);
figure
plot((180/pi)*theta,Br)
xlabel('theta (mech deg)')
ylabel('B_r (T)')
grid; grid minor
```

Appendix K

Matlab code for parametric analysis

For sweeping over h_{mod}, in rotating modulator case the code can be found below. It can simply be generalized to other parameters. The analysis is in the condition of a constant R_o.

```
% parametric analysis if [Ro is constant]

% magnetically-geared machines
% rotating modulators, flux-tube model
% Sajjad Mohammadi @ MIT, 2AM, May 24, 2019
clc;clear;

%   x1 x2  x3 x4   x5   x6    x7   x8   x9    x10    x11   x12    x13
%x=[ps pm  f  N    gi   go   hmod  hm  alpha  Br    Irms   Ro      L]
x =[2  11 50 180  1e-3 1e-3  6e-3 5e-3  0.9   1.1   2.1   58e-3  50e-
3];
% all parameters below are equeal to  corresponding element in  vector
x...
% if we want to sweep a parameter it will not be equal to the vector...
% element but will be equal to the sweep variable

xx=(3:0.1:30)*1e-3; % hmod
ii=1;
for val=xx

Irms=x(11); % RMS current of stator (A)
Is=sqrt(2).*Irms; % peak current of stator (A)
N=x(4); % total number of turns in a phase winding
f=x(3); % electrical frequency (Hz)

ps=x(1); % stator pole pair
pm=x(2); % PM pole pair
pmod=ps+pm; % modulator pole pair

alpha=x(9); % PM ratio
T_pm=alpha.*2.*pi/(2.*pm); % PM arc

gi=x(5);    % inner air-gap (m)
go=x(6);   % outer air-gap (m)

hm=x(8);     % PM height (m)

hmod=val;
% hmod=x(7);    % modulator height (m)

R2=x(12); % stator outer radius (m)
R1=R2-(gi+hmod+go); % inner radius of PMs (m)
Rav=(R1+R2)/2; % average radius of modulators (m)
```

```
slot=36; % number of stator slots
mm=3; % slot per pole per phase (distributed winding)
gamma=ps.*2.*pi/slot; % slot pitch (electrical degrees)
kd=sin(mm.*gamma/2)/(mm.*sin(gamma/2)); % distribution factor
kp=1; % pitch factor
kw=kp.*kd; % winding factor

w=R1.*2.*pi/slot; % slot pitch (m)
ws=2e-3; % slot opening (m)
kc=( 1-(ws/w)+(4.*gi/(pi.*w)).*log(1+pi.*ws/(4.*gi)) )^(-1); %Carter's
coefficient

gie=kc.*gi; %effective air-gap (m)
g_diff=gie-gi; % g-difference
R1=R1-g_diff; % reducing the stator outer radius by g-diffrence (m)
Rav_t=(R1+R2)/2; % average radius of torque calculations (m)

L=x(13); % axial length (m)

Br=x(10); % residual flux of PMs (T)
u0=4.*pi.*1e-7;
M0=Br/u0; % PM Magnetization

T_mod=2.*pi/(2.*pmod); % modulator arc (rad)
wmod=Rav.*T_mod; % modulator width (m)

% switching between the two flux tube models
if hmod<(pi.*wmod/2)

    % Model A
    Pmin=u0/(gie+hmod+go+hm);
    Pmid=(u0/hmod).*log(1+hmod/(gie+go+hm));
    Pmax=u0/(gie+go+hm);

    dt=hmod/(pi.*Rav);
    P0=(1/2).*(Pmax+Pmin)+(pmod.*dt/pi).*(Pmid-Pmin);
    P1=(2/pi).*(Pmax-Pmid)+(2/pi).*(Pmid-Pmin).*sin(pi/2+pmod.*dt);
    disp('model A')
else

    % Model B
    Pmin=(2.*u0/(pi.*wmod)).*log(1+pi.*wmod/(2.*(gie+go+hm)));
    Pmax=u0/(gie+go+hm);

    P0=(1/2).*(Pmax+Pmin);
    P1=(1/2).*(4/pi).*(Pmax-Pmin);
    disp('model B')
end

beta=0:0.01:pi; % torque angle (rad)

Ts=(3/2)*(4/pi)*(R1)*(Br/u0)*L*kw*N*Is*hm*P1*sin(pm*T_pm/2);
```

```
Tm=(3/2)*(4/pi)*(R2*hm+hm^2)*pm/ps*(Br/u0)*L*kw*N*Is*P1*sin(pm*T_pm/2);
%lorentz law

Tmax(ii)=Ts+Tm;
ii=ii+1;
end

plot(xx,Tmax)
xlabel('h_m_o_d')
ylabel('Torque (Nm)')
axis tight
grid
```

The result is shown in Fig. K.1

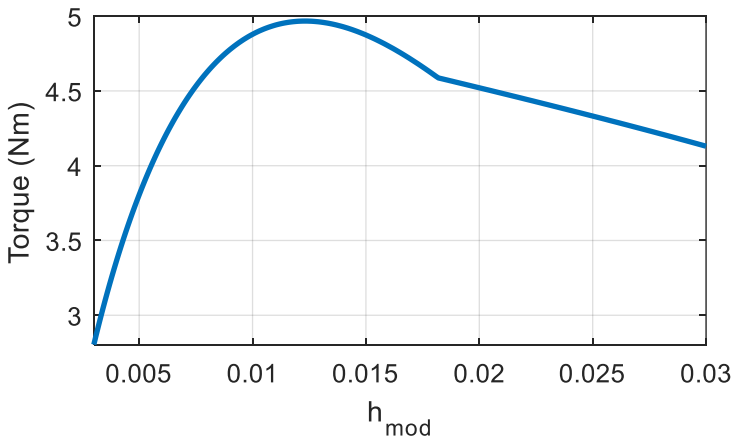

Figure K.1: Parametric analysis over h_{mod}

Bibliography

Chapter 1

[1] S. Kim, E. Park, S. Jung, and Y. Kim, "Transfer torque performance comparison in coaxial magnetic gears with different flux modulator shapes," *IEEE Trans. Magn.*, vol. 53, no. 6, Jun, 2017.

[2] M. Johnson, M. Gardner, H. A. Toliyat, "Design and Analysis of an Axial Flux Magnetically Geared Generator," *IEEE Trans. Ind. Appl.*, vol. 53, no. 1, Jan/Feb, 2017.

[3] M. Johnson, M. Gardner, H. A. Toliyat, "Design and Analysis of an Axial Flux Magnetically Geared Generator," *2015 IEEE Energy Conversion Congress and Exposition (ECCE)*, 2015.

[4] L. L. Wang, J. X. Shen, P. C. K. Luk, W. Z. Fei, C. F. Wang, and Hao, "Development of a Magnetic-Geared Permanent-Magnet Brushless Motor," *IEEE Trans. Magn.*, vol. 45, no. 10, Oct, 2009.

[5] N. W. Frank and H. A. Toliyat, "Gearing ratios of a magnetic gear for wind turbines," *in Proc. IEEE Int. Elect. Mach. Drives Conf.*, May 3–6, 2009, pp. 1224–1230.

[6] M. Johnson, M. Gardner, H. A. Toliyat, S. Englebretson, W. Ouyang, and C. Tschida, "Design, Construction, and Analysis of a Large-Scale Inner Stator Radial Flux Magnetically Geared Generator for Wave Energy Conversion," *IEEE Trans. Ind. Appl.*, vol. 54, no. 4, Jul./Aug. 2018.

[7] M. Johnson, M. Gardner, H. A. Toliyat, S. Englebretson, W. Ouyang, and C. Tschida, "Design, Construction, and Analysis of a Large-Scale Inner Stator Radial Flux Magnetically Geared Generator for Wave Energy Conversion," *IEEE Energy Conversion Congress and Exposition (ECCE)*, 2017.

[8] S. Pakdelian and H. A. Toliyat, "Trans-rotary magnetic gear for wave energy applicaion," *in Proc. Power Energy Soc. Gen. Meeting*, 2012, pp. 1–4.

[9] A. Rotondale, M. Villani, and L. Castellini, "Analysis of high-performance magnetic gears for electric vehicle," *in Proc. IEEE Int. Elect. Veh. Conf.*, Dec. 17–19, 2014, pp. 1–6.

[10] M. Gardner, M. Johnson, H. A. Toliyat, "Analysis of High Gear Ratio Capabilities for Single-Stage, Series Multistage, and Compound Differential Coaxial Magnetic Gears," *IEEE Trans. Energy Convers.*, vol. 34, no. 2, Jun. 2019.

[11] M. Gardner, M. Johnson, E, Benjamin E. Jack, H. A. Toliyat, "Comparison of Surface Mounted Permanent Magnet Coaxial Radial Flux Magnetic Gears Independently

Optimized for Volume, Cost, and Mass," *IEEE Trans. Energy Convers.*, vol. 54, no. 3, May/Jun. 2018.

[12] M. Johnson, M. Gardner, H. A. Toliyat, "Design Comparison of NdFeB and Ferrite Radial Flux Surface Permanent Magnet Coaxial Magnetic Gears," *IEEE Trans. Energy Convers.*, vol. 54, no. 2, Mar./Apr. 2018.

[13] M. Gardner, M. Johnson, H. A. Toliyat, "Comparison of Surface Permanent Magnet Axial and Radial Flux Coaxial Magnetic Gears," *IEEE Trans. Energy Convers.*, vol. 33, no. 4, Dec. 2018.

[14] V. M. Acharya, J. Z. Bird, and M. Calvin, "A flux focusing axial magnetic gear," *IEEE Trans. Magn.*, vol. 49, no. 7, pp. 4092–4095, Jul. 2013.

[15] M. Johnson, M. C. Gardner, and H. Toliyat, "Analysis of axial field magnetic gears with Halbach arrays," *in Proc. IEEE Int. Elect. Mach. Drives Conf., 2015*, pp. 108–114.

[16] M. Johnson, M. Gardner, H. A. Toliyat, "A Parameterized Linear Magnetic Equivalent Circuit for Analysis and Design of Radial Flux Magnetic Gears—Part I: Implementation," *IEEE Trans. Energy Convers.*, vol. 33, no. 2, Jun. 2018.

[17] M. Johnson, M. Gardner, H. A. Toliyat, "A Parameterized Linear Magnetic Equivalent Circuit for Analysis and Design of Radial Flux Magnetic Gears–Part II: Evaluation," *IEEE Trans. Energy Convers.*, vol. 33, no. 2, Jun. 2018.

[18] T. Lubin, S. Mezani, and A. Rezzoug, "Development of a 2-D analytical model for the electromagnetic computation of axial-field magnetic gears*," IEEE Trans. Magn.*, vol. 49, no. 11, pp. 5507–5521, Nov. 2013.

[19] K. Atallah and D. Howe, "A novel high-performance magnetic gear," *IEEE Trans. Magn.*, vol. 37, no. 4, pp. 2844–2846, Jul. 2001.

[20] K. Atallah, S. D. Calverley, and D. Howe, "Design, analysis and realization of a high-performance magnetic gear," *IEE Proc. Elect. Power Appl.*, vol. 151, no. 2, pp. 135–143, Mar. 2004.

Chapter 2

[21] N. Bianchi, 'Electrical Machine Analysis using finite elements', *CRC press*, 2005.

[22] S. Mohammadi, M. Mirsalim, S. Vaez-Zadeh, and H. A. Talebi, 'Design Analysis of a New Axial-Flux Interior Permanent-Magnet Coupler', *5th Power Electronics, Drive Systems and Tech. Conf. 2014*, Tehran.

[23] S. Mohammadi, M. Mirsalim, S. Vaez-Zadeh, and H. Lesani, 'Sensitivity Analysis and Prototyping of a Surface-Mounted Permanent-Magnet Axial-Flux Coupler', *The 5th Power Electronics, Drive Systems and Tech. Conf. 2014*, Tehran.

[24] S. Mohammadi, M. Mirsalim, H. Rastegar, H. Lesani, and B. Vahidi, 'A Neural Network Based Saturation Model for Dynamic Modeling of Synchronous Machines', *5th Power Electronics, Drive Systems and Tech. Conf. 2014*, Tehran.

[25] S. Mohammadi, M. Mirsalim, M. Niazazari, and H. A. Talebi, 'A New Interior Permanent-Magnet Radial-Flux Eddy-Current Coupler', in *Proc. The 5th Power Electronics, Drive Systems and Tech. Conf. 2014*, Tehran, Iran.

[26] A. Vakilian-Zand, S. Mohammadi, J. S. Moghani, and M. Mirsalim, 'Sensitivity Analysis and Performance Optimization of an Industrial Squirrel-Cage Induction Motor Used for a 150 HP Floating Pump', *5th Power Electronics, Drive Systems and Tech. Conf. 2014*, Tehran.

[27] Gh. Davarpanah, S. Mohammadi, J. Kirtley, 'A Novel 8/10 Two-Phase Switched Reluctance Motor with Enhanced Performance: Analysis and Experimental Study', *IEEE Transactions on Industry applications*, DOI: 10.1109/TIA.2019.2908952, 2019.

[28] Gh. Davarpanah, S. Mohammadi, J. Kirtley, 'A Novel 8/10 Two-Phase Switched Reluctance Motor with Enhanced Performance', in *53rd IEEE Industry Applications Society Annual Meeting 2018*, Portland, USA.

[29] C. Lee, R. Krishnan, and N. S. Lobo, 'Novel Two-Phase Switched Reluctance Machine Using Common-Pole E-Core Structure: Concept, Analysis, and Experimental Verification', *IEEE Trans. Ind. Appl.*, vol. 45, no. 2, pp. 703–711, Mar./Apr. 2009.

[30] H. Eskandari, and M. Mirsalim, 'An Improved 9/12 Two-Phase E-Core Switched Reluctance Machine', *IEEE Trans. Energy Convers.*, vol. 28, no. 4, pp. 951–958, Dec. 2013.

Chapter 3

[31] S. Mohammadi, and M. Mirsalim, 'Analytical Design Framework for Torque and Back-EMF Optimization, and Inductance Calculation in Double-Rotor Radial-Flux Air-Cored Permanent-Magnet Synchronous Machines', *IEEE Transactions on Magnetics*, vol. 50, no. 1, Jan 2014.

[32] S. Mohammadi, M. Mirsalim, S. Vaez-Zadeh, and H.A. Talebi, 'Analytical Modeling and Analysis of Axial-Flux Interior Permanent-Magnet Couplers', *IEEE Transactions on Industrial Electronics*, vol. 61, no. 11, pp. 5940-5947, Nov 2014.

[33] S. Mohammadi, M. Mirsalim, and S. Vaez-Zadeh, 'Nonlinear Modeling of Eddy-Current Couplers', *IEEE Transactions on Energy Conversion*, vol. 29, no. 1, pp. 224-231, March 2014.

[34] S. Mohammadi, and M. Mirsalim, 'Double-Sided Permanent-Magnet Radial-Flux Eddy-Current Couplers: Three-Dimensional Analytical Modeling, Static and Transient Study, and Sensitivity Analysis', *IET Electric Power Applications*, vol. 7, no. 9, pp. 665–679, 2013.

[35] S. Mohammadi, B. Vahidi, M. Mirsalim, and H. Lesani, 'Simple Nonlinear MEC-Based Model for Sensitivity Analysis and Genetic Optimization of Permanent-Magnet Synchronous Machines', *COMPEL: The International Journal for Computation and Mathematics in Electrical and Electronic Engineering*, vol. 24, no. 1, 2015.

[36] S. Mohammadi, and M. Mirsalim, 'Design Optimization of Double-Sided Permanent-Magnet Radial-Flux Eddy-Current Couplers', *Elsevier: Electric Power Systems Research*, vol. 108, pp. 282-292, 2014.

[37] Gh. Davarpanah, S. Mohammadi. and J. Kirtley, "Flux-tube based modeling of switched reluctance Motors," to be submitted to *IEEE Transactions on Magnetics*.

[38] M. Hsieh and Y. Hsu, "A generalized magnetic circuit modeling approach for design of surface-permanent magnet machines," *IEEE Trans. Ind. Electron.*, vol. 59, no. 2, pp. 779–792, Aug. 2012.

[39] N. K. Sheth, and K. R. Rajagopal, 'Calculation of the Flux-Linkage Characteristics of a Switched Reluctance Motor by Flux Tube Method', *IEEE Trans. Magn.*, vol. 41, no. 10, pp. 4069–4071, Oct. 2005.

[40] G. Cao, L. Li, S. Huang, L. Li, Q. Qian, and J. Duan, 'Nonlinear Modeling of Electromagnetic Forces for the Planar-Switched Reluctance Motor', *IEEE Trans. Magn.*, vol. 51, no. 13, pp. 1–5, Nov. 2015.

Chapter 4

[41] M. Zahn, 'Electromagnetic field theory: a problem solving approach', *Jon Wiley and Sons, Inc.*, 1979.

[42] R. M. Fano, L. J. Chu, R. B. Adler, 'Electromagnetic fields, energy and forces', *Jon Wiley and Sons, Inc.*, 1960.

[43] H. A. Haus, J. R. Melcher, ‘Electromagnetic fields and energy, *Prentice-Hall. Inc.*, 1989.
[44] D. C. Hanselman, Brushless Permanent Magnet Motor Design, 2nd ed. USA: Magna Physics Publishing, 2006.